Origin of carbonate-bearing rocks in Jezero crater: Implications for ancient habitability in subsurface environments

J.D. Tarnas[1], K.M. Stack[1], M. Parente[2], J.F. Mustard[3], A.H.D. Koeppel[4], K.R. Moore[1], B.H.N. Horgan[5], F.P. Seelos[6], E.A. Cloutis[7], P.B. Kelemen[8], D. Flannery[9], A.J. Brown[10], K.R. Frizzell[11], P. Pinet[12]

[1]NASA Jet Propulsion Laboratory, California Institute of Technology, [2]University of Massachusetts at Amherst Department of Electrical and Computer Engineering, [3]Brown University Department of Earth, Environmental and Planetary Sciences, [4]Northern Arizona University, Department of Astronomy and Planetary Science, [5]Purdue University Department of Earth, Atmospheric, and Planetary Sciences, [6]Johns Hopkins University Applied Physics Lab, [7]University of Winnipeg Department of Geography, [8]Columbia University Lamont-Doherty Earth Observatory, [9]Queensland University of Technology School of Earth and Atmospheric Sciences, [10]Plancius Research, Severna Park, MD, [11]Rutgers University Department of Earth and Planetary Sciences, [12]Institut de Recherche en Astrophysique et Planétologie.

Abstract

Jezero crater, an ancient lake basin that is the landing site of the Mars 2020 Perseverance rover, contains a carbonate-bearing rock unit termed the margin fractured unit. Some of the carbonates in these rocks may have formed in a fluviolacustrine environment and therefore could preserve biosignatures of paleolake-inhabiting lifeforms. Here we evaluate whether these

margin fractured unit carbonates formed as authigenic precipitates in a fluviolacustrine environment or via alteration of primary minerals by groundwater. We integrate thermal inertia measurements from the Thermal Emission Imaging System (THEMIS), spectral analyses from the Compact Reconnaissance Imaging Spectrometer for Mars (CRISM), examination of stratigraphic relationships in Jezero crater using High Resolution Science Experiment (HiRISE) and Context Camera (CTX) images and digital elevation models. We also compare the Jezero crater results to observations from the Curiosity rover in Gale crater. We find that margin fractured bedrock with the deepest visible-to-near-infrared carbonate absorptions also has exceptionally high thermal inertia and thickness relative to other carbonate-bearing units in Jezero crater, consistent with enhanced cementation and crystallization by groundwater. Our results indicate that it is equally likely that carbonates in Jezero crater formed via alteration of primary minerals by alkaline groundwater rather than as authigenic precipitates in a fluviolacustrine environment. Jezero crater may have hosted ancient subsurface habitable environments related to these groundwaters, where life-sustaining redox energy was generated by water-rock interactions. The Mars 2020 Perseverance rover could encounter biosignatures preserved from this carbonate-forming environment, whether it was fluviolacustrine or in the subsurface.

Plain Language Summary

Spacecraft orbiting Mars can measure the composition of rocks that make up its surface. Understanding rock composition allows us to interpret past environmental conditions on Mars, including their likelihood to be habitable. Using data acquired from orbit, researchers have

found carbonate minerals in Jezero crater and the surrounding region–called the Nili Fossae region. Jezero crater is the landing site of NASA's Mars 2020 Perseverance rover and once contained a lake. The discovery of carbonates is exciting because on Earth they sometimes form in habitable environments and preserve fossils. In this study, we show that it is equally likely that carbonates in Jezero crater formed by groundwater rather than forming in Jezero crater's ancient lake. We also find that contact with past groundwater likely changed the physical properties of some rocks in Jezero crater that contain carbonate, which made the carbonate composition more obvious from orbit. Many carbonates that form by groundwater on Earth preserve fossils from underground habitable environments, where organisms obtain energy from chemicals dissolved in water rather than from sunlight. We propose that fossils from similar underground ancient habitable environments could exist in the Jezero carbonates, exposed at the surface by rock erosion over billions of years.

1.0 Introduction

The Nili Fossae region lies immediately west of the ~3.96 Gyr old (Werner, 2008) Isidis impact structure on Mars and north of the Late Hesperian age (Greely and Guest, 1987) Syrtis Major volcano. Widespread occurrences of olivine were first reported in Nili Fossae using data from the Thermal Emission Spectrometer (TES; Christensen et al., 2001) aboard the Mars Global Surveyor spacecraft (Hoefen et al., 2003). Nili Fossae is one of the most mineralogically diverse exposures of the martian surface, with evidence for olivine, pyroxene (Mustard et al., 2009), phyllosilicates (Ehlmann et al., 2009; Mustard et al., 2008), carbonates (Ehlmann et al., 2008b), and sulfates (Ehlmann and Mustard, 2012; Quinn and Ehlmann, 2019) observed in orbital

spectroscopic data. Here we focus primarily on the olivine-bearing unit in Jezero crater and the surrounding Nili Fossae region, which we term the regional olivine-bearing unit (ROB unit).

Previously proposed origins for the ~3.82 $\pm$ 0.07 Gyr age (Mandon et al., 2020) ROB unit include an ultramafic ashfall deposit (Kremer et al., 2019; Mandon et al., 2020), an impact spherule deposit (Palumbo and Head, 2018) from an impact younger than Isidis (Mandon et al., 2020), or detrital sedimentary rock (Rogers et al., 2018). Spectral data interpreted by modeling suggest ~20-25% modal abundance of olivine in this unit (Edwards and Ehlmann, 2015) and average olivine grain sizes of 0.5 mm or larger (Brown et al., 2020). It has been variably altered to carbonate, phyllosilicate(s), and possibly hydrated silica (Bramble et al., 2017; Brown et al., 2010; Ehlmann et al., 2008b; Goudge et al., 2015; Mandon et al., 2020; Tarnas et al., 2019; Viviano et al., 2013) and has a fractured-to-rubbly texture (Bramble et al., 2017; Kremer et al., 2019). Its compositional and thermal inertia properties are similar to the Algonquin olivine-rich tephra deposit and Comanche carbonate investigated by NASA's Spirit rover (Ruff et al., 2019), as well as other high thermal inertia clastic rocks on Mars (Rogers et al., 2018). The ROB unit drapes into the Jezero crater rim and is present on the modern-day crater floor (Goudge et al., 2015; Kremer et al., 2019; Mandon et al., 2020; Sun and Stack, 2020). It is also incised by rivers that flowed into Jezero crater (Goudge et al., 2015) and deposited the deltaic outcrops there (Fassett and Head, 2005; Goudge et al., 2017; Schon et al., 2012). The Jezero delta deposits contain low calcium pyroxene, olivine, phyllosilicate(s), carbonate, and possible hydrated silica (Ehlmann et al., 2009; Goudge et al., 2018, 2015; Horgan et al., 2020a), much of which is likely detrital (Goudge et al., 2015), but some of which may be authigenic (Bristow and Milliken, 2011).

Recent photogeologic mapping has defined 15 bedrock units in western Jezero crater (Stack et al., 2020). Five of these units are carbonate-bearing: the delta blocky unit, delta truncated curvilinear layered unit, delta layered rough unit, crater floor fractured 2 unit, and margin fractured unit (Figure 1). Goudge et al., (2015) and Ehlmann et al., (2008) grouped the carbonate-bearing units exposed along the inner margin (margin fractured) and on the crater floor (crater floor fractured 2) of Jezero, and correlated these deposits within the crater with the surrounding ROB unit, due to their morphological and spectral similarities. Later work presented the evidence consistent with a fluviolacustrine origin for carbonates in the margin fractured unit, highlighting in particular the association of deeper 2.5 μm absorptions and low 2.3/2.5 μm band depth ratios with the approximate maximum height of the Jezero paleolake (Horgan et al., 2020a). These authors also highlighted possible spectral trends with respect to distance from the inlet valley. An unknown amount of fluviolacustrine sediment was deposited along the crater rim during highstanding periods of the Jezero paleolake, and it is possible that these sediments were carbonate-bearing and have since been lithified, as is common along margins of alkaline lakes on Earth (Horgan et al., 2020a). The observation of strong VNIR spectral signals of carbonate near the former margin of the Jezero paleolake is therefore consistent with formation of these carbonates in a near-shore fluviolacustrine environment. Here we compare the evidence for the carbonate formation scenario presented by Goudge et al., (2015) and Ehlmann et al., (2008)—where carbonate formation in the margin fractured unit and ROB occurs via the same processes—versus the fluviolacustrine carbonate formation scenario proposed by Horgan et al., (2020a).

Determining the conditions of carbonate formation in Jezero crater is key to evaluating past habitability and potential for biosignature preservation in rocks explored by the Perseverance rover. This must be undertaken using orbital data until the Perseverance rover encounters carbonate-bearing rocks, which it will be guided to via interpretations of orbital data. The Mars Science Laboratory Curiosity rover recently groundtruthed CRISM hematite detections in Gale crater (Fraeman et al., 2020b), providing valuable context for how interpretations of orbitally-acquired ~12-32 m/pixel VNIR hyperspectral images (Fraeman et al., 2013) compare to the true compositional nature of rocks determined in-situ (David et al., 2020; Fraeman et al., 2020a, 2020b; Frydenvang et al., 2020; Horgan et al., 2020b; Jacob et al., 2020; L'Haridon et al., 2020; McAdam et al., 2020; Morris et al., 2020; Rampe et al., 2020; Thompson et al., 2020). To evaluate the most likely origin scenarios for carbonate-bearing rocks in Jezero crater, we integrated data from the Compact Reconnaissance Imaging Spectrometer for Mars (CRISM; Murchie et al., 2007), images and digital elevation models (DEMs; Beyer et al., 2018) from the High Resolution Imaging Science Experiment (HiRISE; McEwen et al., 2007) and Context Camera (CTX; Malin et al., 2007), as well as data from the Thermal Emission Imaging System (THEMIS; Christensen et al., 2004).

2.0 Background

Phyllosilicates in the Nili Fossae region were first discovered using data from the Observatoire pour la Minéralogie, l'Eau, les Glaces et l'Activité (OMEGA; Bibring et al., 2004) instrument aboard Mars Express (Poulet et al., 2005), indicating that this landscape preserves evidence of past aqueous activity. Higher spatial resolution data from CRISM aboard the Mars

Reconnaissance Orbiter (MRO) found evidence for phyllosilicates (Ehlmann et al., 2009; Mustard et al., 2008), carbonates (Ehlmann et al., 2008b), sulfates (Ehlmann and Mustard, 2012; Quinn and Ehlmann, 2019), and mafic minerals (Mustard et al., 2009) in Nili Fossae and showed that these minerals were correlated with specific units in a regionally extensive stratigraphy. From oldest to youngest, the Nili Fossae region includes a basement sequence, an olivine-bearing unit, a capping unit, and a sulfate-bearing unit (Ehlmann and Mustard, 2012). The basement sequence has been further subdivided into the Stratified Basement Unit, Blue Fractured Unit, Mixed Lithology Plains Unit, LCP-bearing Plateaus Unit, and Fe/Mg-smectite-bearing Mounds Unit (Scheller and Ehlmann, 2020) and contains well-preserved martian crust older than 3.9 Gyr (Mustard et al., 2009), which has no comparably well-preserved analog in Earth's geologic record. The basement sequence contains widespread low calcium pyroxene and phyllosilicate VNIR spectral signatures (Scheller and Ehlmann, 2020), as well as outcrops containing kaolinite (Bramble et al., 2017; Ehlmann et al., 2009) and hydrated silica (Tarnas et al., 2019). The capping unit is associated with spectra consistent with mafic minerals (Bramble et al., 2017; Mustard et al., 2009) and glass (Cannon et al., 2017) and is interpreted to be volcaniclastic (Bramble et al., 2017; Hundal et al., 2020). The sulfate-bearing unit records evidence for standing bodies of water, diagenesis under acidic conditions, and fluvial activity (Quinn and Ehlmann, 2019).

Alteration hypotheses for the ROB unit, including the exposures on the Jezero crater floor and margin, include groundwater percolation under geothermal gradient-driven temperatures (Ehlmann et al., 2009), alteration under a thick CO_2 atmosphere (Edwards and Ehlmann, 2015; van Berk and Fu, 2011), simultaneous serpentinization and carbonation that

occurred during dehydration of the underlying phyllosilicate basement (Brown et al., 2010; Viviano et al., 2013), carbonation of partially serpentinized olivine (Viviano et al., 2013), alteration under the conditions of the modern day martian atmosphere (Kelemen et al., 2020a), low temperature water-rock alteration (Edwards and Ehlmann, 2015), low temperature carbonate rind formation (Ehlmann et al., 2008b; Jull et al., 1988), or surface weathering to carbonate (Ehlmann et al., 2008b). Distinguishing between these hypotheses using orbital data alone is challenging, but mineral identifications and geologic context observed by the Mars 2020 Perseverance rover should be sufficient to constrain the causes of carbonation and other alteration, as mineral assemblages and their distributions can be used to constrain reaction conditions.

Carbonation of Fe, Mg, and Ca-bearing silicate material on Earth—including mafic and ultramafic rock—occurs via water-rock-gas reactions with high CO_2 activity/partial pressure in both high and low temperature and pressure conditions. Direct carbonation of olivine occurs via the reaction

(1) $(Ca,Mg,Fe)_2SiO_4$ (olivine) + $2CO_{2,aq} \rightarrow 2(Ca,Mg,Fe)CO_3$ (carbonate)+SiO_2 (hydrated silica)

while carbonation of pyroxene and olivine can occur via the reaction series

(2) $(Ca,Mg,Fe)_2SiO_4$ (olivine) + $(Ca,Mg,Fe)_2Si_2O_6$ (pyroxene) + $2CO_{2,aq}$ + $2H_2O \rightarrow$ $(Fe,Mg)_3Si_2O_5(OH)_4$ (serpentine) + $2(Ca,Mg,Fe)CO_3$ (carbonate)

(3) $(Mg,Fe)_2SiO_4$ (olivine) + $6H_2O \rightarrow 2(Fe,Mg)_3Si_2O_5(OH)_4$ (serpentine) + $2(Fe,Mg)(OH)_2$ (brucite)

(4) $2(Fe,Mg)(OH)_2$ (brucite) + $2CO_{2,aq} \rightarrow 2(Fe,Mg)CO_3$ (carbonate) + $2H_2O$

(5) $2(Fe,Mg)_3Si_2O_5(OH)_4$ (serpentine) + $3CO_{2,aq}$ → $Mg_3Si_4O_{10}(OH)_2$ (talc) + $3(Mg,Fe)CO_3$ (carbonate) + $5H_2O$

(6) $Mg_3Si_4O_{10}(OH)_2$ (talc) + $3CO_{2,aq}$ → $3(Mg,Fe)CO_3$ (carbonate) + $4SiO_2$ (hydrated silica) + $6H_2O$

which forms carbonate, hydrated silica, serpentine, talc, and brucite (Kelemen et al., 2011; Matter and Kelemen, 2009; Moody, 1976; Oelkers et al., 2008). If reactions 1-6 all proceed to completion, the resulting minerals are carbonates and hydrated silica. This is what has occurred in listvenite deposits where all primary minerals have been altered to form carbonate and hydrated silica (e.g., Falk and Kelemen, 2015). Carbonation of olivine always results in precipitation of additional silicate minerals that contain the Si atoms from olivine and pyroxene that lose their hosted cations to more thermodynamically stable carbonate minerals (e.g., Falk and Kelemen, 2015; Kelemen et al., 2020b). The rate of olivine carbonation is maximized at ~185 ^{o}C, but also occurs at slower rates at temperatures between ~1-350 ^{o}C (Kelemen and Hirth, 2012; O'Connor et al., 2005). The rate of carbonation is more sensitive to temperature than pressure (Kelemen and Hirth, 2012) and is most sensitive to CO_2 partial pressure (P_{CO2}), with carbonation rates increasing roughly linearly as a function of increasing P_{CO2} (O'Connor et al., 2005). Fluids associated with carbonation of olivine typically have high pH, high alkalinity, and low oxygen fugacity (Kelemen et al., 2011). Fluid chemistries associated with carbonation of silicates are habitable when temperatures are less than 122 ^{o}C, the currently known high temperature limit for life (Takai et al., 2008), resulting in microbial inhabitation of many peridotites actively experiencing serpentinization/carbonation (e.g., Kraus et al., 2021; Rempfert et al., 2017; Schrenk et al., 2013).

198 During carbonation of silicates, reaction-driven cracking due to volume expansion
199 exposes fresh primary mineral surfaces (Kelemen and Hirth, 2012; Klein and Le Roux, 2020) and
200 produces fracture networks filled with mineralized carbonate veins (Evans et al., 2020; Kelemen
201 and Matter, 2008). Carbonation of ultramafic rocks occurs in submarine oceanic crust as well as
202 in obducted oceanic crust –ophiolites (Falk and Kelemen, 2015; Kelemen et al., 2020b).
203 Subaerial and submarine ultramafic volcanics, including komatiites, kimberlites, and boninites,
204 are also typically carbonated (Mitchell et al., 2019). Some of this carbonate is igneous, erupting
205 from the mantle as carbonatite-ultramafic melts/tuffs, which have the lowest SiO_2 activity of
206 any known volcanic material (Agashev et al., 2008; Dongre and Tappe, 2019; Doroshkevich et
207 al., 2019; Duke et al., 2014; Melluso et al., 2010; Russell et al., 2012; Shavers et al., 2016; Sparks
208 et al., 2009; White et al., 2012). Kimberlites erupt from >150 km depth, have high CO_2 activity,
209 and typically contain carbonates of secondary origins, in addition to primary carbonates from
210 carbonatite melt components (Sparks, 2013). Some aqueous alteration/carbonation during
211 emplacement likely occurs via alteration by volatiles hosted in melts during their eruption
212 (Mitchell, 2013, 2008; Mitchell et al., 2019, 2009), while some aqueous alteration likely occurs
213 via assimilation of surface/near-surface fluids in a hydrothermal system within the hot
214 ultramafic tuff or solidifying lava (Sparks et al., 2009).
215 Carbonate can also abiotically precipitate independently of the presence of ultramafic
216 materials, including in evaporite deposits (e.g., Kah et al., 2001), within carbonate-saturated
217 water columns (e.g., Given and Wilkinson, 1985), and as pedogenic carbonate in soils
218 (Zamanian et al., 2016). Biomediated precipitation of carbonate occurs in soils (e.g., Whiffin et
219 al., 2007) and within water columns (e.g., Dupraz et al., 2004), or in structures such as microbial

mats (e.g., Dupraz et al., 2009), shells, and reefs (e.g., Webb, 1996). Evaporite deposits often contain other minerals in assemblage with carbonate, depending on the initial fluid composition, including various sulfates and chlorides (e.g., Kah et al., 2001). Biomediated carbonate precipitation in the water column is not necessarily accompanied by precipitation of other minerals (e.g., Dupraz et al., 2009, 2004; Webb, 1996). Both abiotically and biotically precipitated carbonates preserve biosignatures on Earth. The habitability of conditions under which carbonates precipitate is therefore the most important control on carbonate biosignature preservation potential.

Martian carbonates have been identified in meteorites ALH 84001, Nakhla, Governor Valadares, Lafayette, and EETA 79001 (McSween, 1994), in the Comanche carbonate investigated by the Spirit rover (Morris et al., 2010), in soil surrounding the Phoenix lander (Boynton et al., 2009), possibly globally in Mars dust (Bandfield et al., 2003) using TES–though sulfates could also explain this spectral signature (Lane et al., 2004), and in bedrock in multiple localities on the planet using CRISM (Amador et al., 2017; Bultel et al., 2019; Carrozzo et al., 2017; Carter et al., 2015; Ehlmann et al., 2008b; Jain and Chauhan, 2015; Michalski et al., 2017, 2013; Michalski and Niles, 2010; Wray et al., 2016) and TES (Glotch and Rogers, 2013). Carbonate detections using CRISM are typically associated with mixed or proximal phyllosilicates (Bultel et al., 2019; Carrozzo et al., 2017; Michalski et al., 2017; Wray et al., 2016). Assuming equilibrium conditions, carbonates in ALH 84001 formed at 18 ± 4 °C (Halevy et al., 2011) 3.9-4.0 Gyr ago (Borg et al., 1999) and are present as concretions or as massive carbonate intergrown with feldspathic glass and orthopyroxene (Corrigan and Harvey, 2004; Steele et al., 2007), while Nahkla and Governor Valadares meteorites contain vein-filling

carbonate (Gooding et al., 1991) and carbonate associated with silicate alteration zones (Bridges and Grady, 2000). The Comanche carbonate has been proposed to form via hydrothermal alteration (Morris et al., 2010) or evaporite precipitation following alteration of the Algonquin volcanic tephra deposits (Ruff et al., 2014).

3.0 Methodology

To characterize the properties of carbonate-bearing rocks in Jezero crater to the greatest extent possible from orbit, we integrated all orbital datasets that are at sufficiently high spatial resolution to investigate individual carbonate-bearing outcrops. We used CRISM to identify VNIR spectra consistent with the presence of carbonate and minerals in assemblage with carbonate, images and DEMs from HiRISE and CTX to characterize morphology and place detections in their geologic and, if possible, stratigraphic contexts, as well as thermal inertia (TI) estimates from THEMIS measurements to evaluate dust cover and rock competency, which we then linked to identified VNIR spectral absorption features. We also used results from recent photogeologic mapping of Jezero crater by the Mars 2020 Rover Science Team (Stack et al., 2020) to determine which of these units are carbonate-bearing. This integrated approach permits evaluation of hypotheses for the origins of carbonate-bearing rocks in Jezero crater.

3.1 CRISM analysis

For this analysis, we focused on CRISM images HRL000040FF (32 m/pixel), FRT000047A3 (18 m/pixel), and FRT00005C5E (18 m/pixel), which cover the Perseverance rover landing site, the geologic units mapped by Stack et al. (2020), and previously identified carbonates. We used

CRISM data produced via three different processing techniques to identify spectral features consistent with the presence of carbonate and additional assemblage minerals. These included (1) the CRISM TRR3 pipeline, (2) the CRISM TER pipeline, and (3) the University of Massachusetts at Amherst (UMass) pipeline (Itoh and Parente, 2021). To identify regions with spectral signatures consistent with carbonate, we combined three separate mineral mapping approaches: (1) Band parameters (Viviano-Beck et al., 2014), (2) Dynamic aperture factor analysis/target transformation (DAFA/TT; Lin et al., 2021), (3) a Generative Adversarial Network based feature extraction technique (GAN; Saranathan and Parente, 2021). We compared the results from each of these techniques to test their validity. We also used DAFA/TT to locate unique spectra that are not present in the Minerals Identified through CRISM Analysis (MICA; Viviano-Beck et al., 2014) library that is employed during typical GAN mapping of CRISM data, then used those DAFA/TT-discovered spectra as prototypes for more detailed GAN mapping. After characterizing the spatial distribution of spectral signals in the three CRISM images analyzed, and interpreting the spectrally-dominant mineralogy consistent with those signals, we isolated CRISM pixels with similar spectral signals that outcropped over defined geologic units (e.g., dunes, differently textured bedrock, low thermal inertia material, high thermal inertia material, and specific geologic units) based on morphology, thermal inertia, and the mapping results from Stack et al. (2020). We then interpreted the mineral assemblages consistent with spectra from these pixels in all three CRISM data types (TRR3, TER, and UMass) via comparison to library spectra. Carbonate minerals are identified by the presence of absorptions centered at 2.3 and 2.5 μm, Fe/Mg-phyllosilicates by a narrow absorption centered at 2.3 μm, Al-phyllosilicate by a narrow absorption centered at 2.2 μm, hydrated silica by a

broad absorption centered at 2.2 μm, and olivine and siderite by a broad absorption centered at 1.0 μm. Integrating this information, we characterized the mineral composition of specific rock units or debris in Jezero crater to the greatest extent currently possible using orbitally-acquired VNIR hyperspectral data.

We compared carbonate spectral signals in Jezero crater with those in the ROB unit elsewhere in the Nili Fossae region using CRISM TRR3 images FRT0000C256, FRT00009D96, FRT000095FE, and FRT000028BA. We chose these images based on the strong carbonate absorption features in this area that were reported by Mandon et al., (2020). Following Horgan et al. (2020a), we mapped the value of the 2.3/2.5 μm absorption band depths in these images to determine whether the carbonate absorption strength seen in the margin fractured unit is unique to Jezero, or is consistent with carbonate spectral signals in the ROB unit throughout the Nili Fossae region. We also used the Hyperspectral Subspace Identification (HySime) algorithm (Bioucas-Dias and Nascimento, 2008) to calculate endmembers imparting spectral variance in CRISM pixels covering outcrops of carbonate-bearing rocks in Jezero crater as well as in the CRISM images covering the ROB in the greater Nili Fossae region. We used information from band parameter mapping (Viviano-Beck et al., 2014) to isolate CRISM pixels used for spectral endmember extraction. If the endmembers resembled spectra characteristic of specific minerals, they were interpreted to reflect the composition of the surface covered by those CRISM pixels. This spectral endmember extraction and interpretation process is analogous to methods applied in past studies (e.g., Bandfield et al., 2002, 2000; Fischer et al., 2015; Glotch and Bandfield, 2006; Smith et al., 2000). It allowed us to extract clean mineral assemblage spectra from both Jezero crater and the surrounding Nili Fossae region CRISM images, even

308 though the images from the surrounding region lacked spectrally bland pixels that would be
309 required for spectral ratioing (e.g., Mustard et al., 2008). This allowed us to directly compare
310 the spectra of carbonate-bearing mineral assemblages in Jezero crater with those in the ROB
311 unit outside of Jezero crater, while also comparing how relative absorption strengths varied
312 across each image.
313
314 *3.2 HiRISE and CTX images and DEMs*
315 We used the HiRISE and CTX image/DEM mosaics of Jezero crater generated by
316 Fergason et al., (2020), as well as HiRISE image/DEM mosaics and a global CTX mosaic
317 generated by Dickson et al., (2020). HiRISE images were used to characterize unit morphology,
318 distinguish between differently textured bedrock units, and differentiate between bedrock and
319 aeolian bedforms or other clearly unconsolidated materials. This information was used to
320 isolate specific CRISM pixels for spectral analysis and mineral assemblage interpretation
321 (Section 3.1). We also used HiRISE DEMs to extract cross sections of CRISM detections and
322 broader-scale geologic units for spectral and stratigraphic interpretations.
323
324 *3.3 THEMIS thermal inertia mapping*
325 We first used the qualitative THEMIS thermal inertia mosaic from Fergason et al.,
326 (2006), which the Dickson et al. (2020) HiRISE image/DEM and CTX image mosaics are
327 coregistered to, in order to differentiate bedrock exposures from unconsolidated material. This
328 information was used to isolate CRISM pixel clusters for spectral analysis and mineral
329 assemblage interpretation (Section 3.1). After characterizing the spectra of different bedrock

330 units and unconsolidated materials in Jezero crater, we noticed a possible correlation between
331 the band depth of the 2.5 μm absorption features—consistent with and attributed to the
332 presence of carbonate—with thermal inertia. To further investigate this relationship, we used a
333 quantitative thermal inertia map to characterize the relationship between thermal inertia and
334 VNIR spectral features in Jezero crater.
335 Quantitative thermal inertia maps of Gale crater were generated by inputting nighttime
336 THEMIS images (~100 m/px) (Christensen et al., 2004b) taken during the southern hemisphere
337 summer into the KRC thermal model (Edwards et al., 2018a; Fergason et al., 2006b; Kieffer,
338 2013), which fits surface temperature estimates at each pixel to seasonally stable thermal
339 inertia values. Additional inputs include observation time parameters (e.g., season, local time,
340 solar azimuth, dust opacity, and modeled air temperatures), surface geometry (e.g., slope
341 angle, aspect, and elevation) and estimates of material properties (e.g., albedo, emissivity,
342 specific heat, and thermal conductivity) (Kieffer, 2013; Putzig et al., 2005).
343
344 *3.4 THEMIS thermal inertia and CRISM band parameter correlation*
345 Using a THEMIS quantitative thermal inertia mosaic combined with CRISM MTRDR data
346 of image HRL000040FF, we evaluated the relationship between quantitative thermal inertia and
347 other band parameters in Jezero crater. In our CRISM and qualitative thermal inertia analysis,
348 we noticed a similarity between thermal inertia and the absorption depth of BD860—attributed
349 to hematite—in Gale crater and thermal inertia and the absorption depth of BD2500_2—
350 attributed to carbonate—in Jezero crater. In Gale crater, Vera Rubin ridge (VRR) has the
351 strongest and most widespread BD860 feature of hematite in northern Mount Sharp (Fraeman

et al., 2013), as well as high thermal inertia relative to the surrounding terrain (Edwards et al., 2018b). In Jezero crater, the margin fractured unit has the strongest BD2500_2 feature of carbonate (Horgan et al., 2020a), as well as high thermal inertia relative to the surrounding terrain (Figure 2). After a detailed campaign by Curiosity, the deeper VNIR hematite absorptions in VRR were attributed to hematite crystallinity enhanced by groundwater and less coverage by unconsolidated material due to cementation that gives VRR its topographic prominence (David et al., 2020; Fraeman et al., 2020a, 2020b; Frydenvang et al., 2020; Horgan et al., 2020b; Jacob et al., 2020; L'Haridon et al., 2020; McAdam et al., 2020; Morris et al., 2020; Rampe et al., 2020; Thompson et al., 2020). Because of the qualitative correlation between CRISM signal and thermal inertia in these localities, we quantitatively compared CRISM VNIR band parameters and quantitative thermal inertia in Gale crater and Jezero crater, interpreting that a similarity in their relationship may be indicative of similar groundwater alteration histories impacting the modern-day physical and spectral properties of VRR and the margin fractured unit. The 1 μm absorption of olivine has previously been shown to not correlate with thermal inertia (Brown et al., 2020).

The algorithm for comparing CRISM band parameters and quantitative thermal inertia data uses Principal Components Analysis to identify which band parameters contribute to the largest variability in the data and reveals how linked each parameter is to the variability in thermal inertia. Using thermal inertia maps resampled to CRISM spatial resolution, data points are then clustered into Gaussian mixtures using only key high-variability band parameters and thermal inertia as inputs. Correlation coefficients between band parameters and a representative average thermal inertia can then be calculated for individual geologic units.

Further details of the classification method can be found in Koeppel et al., (In Review). While we found interesting relationships between multiple CRISM band parameters and thermal inertia, here we focus on BD860 in Gale crater and BD2500_2 in Jezero crater to constrain possible hypotheses for margin fractured unit emplacement, mechanisms for carbonation, and the relationship between orbital observations and anticipated landed observations in Jezero crater.

4.0 Results

Combining the results of our mineral mapping with the photogeologic map of Jezero crater from Stack et al. (2020), we found VNIR spectra consistent with the presence of carbonate (Figure 3) in (1) high TI bedrock in the margin fractured unit (Figures 4-6, S1-S3), (2) large aeolian bedforms proximal to the margin fractured unit (Figures 7, S4-S5), (3) the delta blocky unit (Figure 8), (4) the delta truncated curvilinear unit (Figure 9), (5) undifferentiated smooth material on the western delta (Figures 10, S6), (6) the delta layered rough unit (Figures 11, S7), (7) moderate TI bedrock in the crater floor fractured 2 (CFF 2) unit (Figures 12-13, S8), and (8) low TI dunes and unconsolidated dark-toned material in the CFF 2 unit (Figure 14). We also report five newly discovered occurrences of hydrated silica in the same dark-toned material that Tarnas et al. (2019) and Dundar et al. (2019) reported hydrated silica in (Figures 15-16, S9). Below we describe the VNIR spectral features of these outcrops and associated mineral assemblage interpretations based on these spectral features (Figure 17). We also describe their morphology, thermal inertia properties, geologic context, and if possible stratigraphic relationship to other units in Jezero crater.

396

397 *4.1 Crater floor fractured 2 unit*

398 *4.1.1 VNIR spectra*

399 We find VNIR spectra consistent with the presence of carbonate in bedrock within the
400 crater floor fractured 2 unit (Figures 12, S8), as well as dunes and dark-toned unconsolidated
401 material directly overlying crater floor fractured 2 unit bedrock (Figure 14). The spectra are
402 consistent with a mixture of carbonate, phyllosilicate(s), olivine, and possibly hydrated silica.
403 The presence of carbonate is indicated by absorptions centered at 2.3 and 2.5 μm and has
404 previously been mapped in this unit by Ehlmann et al., (2009) and Goudge et al., (2015). The
405 higher 2.3/2.5 μm absorption band depth ratio of these spectra compared to spectra of pure
406 carbonate, as well as the narrowing of the 2.3 μm feature relative to that of pure carbonate,
407 indicates mixing with phyllosilicate (Figures 12, 14, 17, S8). The broad absorption feature
408 centered at 1.0 μm is consistent with the presence of olivine and/or siderite (Figure 17).
409 Because the crater floor fractured 2 unit contains widespread spectra consistent with olivine,
410 we interpret olivine to be the more likely cause of the 1.0 μm centered broad absorption.
411 The presence of olivine, carbonate, and phyllosilicate(s) in the crater floor fractured 2
412 unit is consistent with past interpretations of the mineral assemblage in this unit in Jezero
413 crater (Horgan et al., 2020b) and the ROB unit in Nili Fossae (Brown et al., 2010). Based on the
414 presence of a 2.2 μm feature (e.g., Figure 17 hydrated silica and montmorillonite spectra) that
415 combines with the narrow 2.3 μm absorption (e.g., Figure 17 saponite, talc, and serpentine
416 spectra), we interpret the presence of hydrated silica and/or Al-phyllosilicate, consistent with
417 the interpretation of this same feature in a similar spectrum from the ROB unit in Tarnas et al.

418 (2019). We reason that this feature is more likely to be caused by presence of hydrated silica
419 rather than Al-phyllosilicate if the protolith material is ultramafic, as hydrated silica is
420 ubiquitous in 100% carbonated olivine deposits (listvenites). However, if the protolith
421 composition of this unit is mafic rather than ultramafic, Al-phyllosilicates may have formed via
422 alteration of plagioclase during carbonation of olivine, as occurs during carbonation of mafic
423 rocks on Earth (Matter and Kelemen, 2009).
424 We find five new outcrops of the smooth dark-toned hydrated-silica-bearing material
425 reported by Tarnas et al. (2019) and Dundar et al. (2019) (Figures 15-16, S9). As reported by
426 Tarnas et al. (2019), this smooth dark-toned material always outcrops immediately above the
427 crater floor fractured unit. We also find an outcrop where smooth dark-toned material partially
428 covers crater floor fractured unit bedrock, but does not cover it entirely, and over this area we
429 find a stronger 2.2 μm absorption consistent with hydrated silica relative to the 2.5 μm
430 absorption consistent with carbonate (Figure 16). This indicates that at least some of the 2.2
431 μm absorption signal from the crater floor fractured 2 unit is due to coverage of crater floor
432 fractured 2 unit bedrock by hydrated-silica-bearing smooth dark-toned material. However,
433 there is likely some material in crater floor fractured 2 bedrock bearing a 2.2 μm absorption
434 feature consistent with hydrated silica and/or Al-phyllosilicate, as this absorption feature is
435 present even when there is no obvious dark-toned material covering the outcrop (e.g., Figure
436 12). The origin and stratigraphic position of this smooth dark-toned hydrated-silica-bearing
437 material remains ambiguous.
438
439 *4.1.2 Morphology, thermal inertia, and geologic context*

Crater floor fractured unit 2 bedrock outcrops containing carbonate-bearing mineral assemblages have fractures and linear ridges that are characteristic of this unit both within Jezero crater and regionally (Bramble et al., 2017; Goudge et al., 2017, 2015). This unit also contains larger-scale topographic features including broader ridges (Figure 13). Carbonate-bearing bedrock textures also include aeolian bedforms and dark-toned rubble overlying light-toned bedrock, which protrudes through this unconsolidated material (Figure 14). The morphology of crater floor fractured 2 unit bedrock with VNIR spectra consistent with carbonate at CRISM spatial scales is not appreciably different from outcrops of this unit with no clear VNIR carbonate spectral absorptions, nor is it appreciably different from the surface textures in much of the margin fractured unit. Parts of the crater floor fractured 2 unit with VNIR spectra consistent with the presence of carbonate are also not topographically higher than unit components that do not have clear VNIR spectral signatures of carbonate. Qualitative thermal inertia estimates (Fergason et al., 2006a) of these outcrops are also consistent with both bedrock and overlying unconsolidated material containing VNIR spectra consistent with the presence of carbonate. The ROB unit is banded (Kremer et al., 2019) and some of this banding is visible in Jezero crater, but only in the crater floor fractured 1 unit. None of these banded outcrops have VNIR spectra at CRISM spatial scales consistent with the presence of carbonate. HiRISE images show no clear contacts between the crater floor fractured 1 and 2 units and the margin fractured unit. A cross section from the ROB unit outside of the crater to the edge of the largest northernmost outcrop of crater floor fractured 1 and 2 units shows a gradational relationship as this unit drapes into Jezero crater (Figure 18). Including the margin fractured unit in this cross section results in the same relationship (Figure 18).

462

463 *4.2 Deltaic units*

464 *4.2.1 VNIR spectra*

465 There are CRISM VNIR spectra consistent with the presence of carbonate in the delta
466 blocky unit (Figure 8), the delta truncated curvilinear unit (Figure 9; Goudge et al., 2017),
467 undifferentiated smooth material on the western delta (Figures 10, S6), and the delta layered
468 rough unit (Figures 11, S7). The spectra are consistent with a mixture of carbonate,
469 phyllosilicate, and either hydrated silica and/or Al-phyllosilicate. The presence of carbonate is
470 indicated by absorptions centered at 2.3 and 2.5 μm. All VNIR spectra containing carbonate
471 absorptions in the deltaic units have higher 2.3/2.5 μm ratios compared to carbonate-bearing
472 VNIR spectra in the crater floor fractured 2 and margin fractured units, indicating a higher
473 spectral abundance of Fe/Mg-phyllosilicates mixed with carbonate in the deltas (Figure 17). The
474 2.2/2.3 μm absorption depth ratios are also lower in the deltaic outcrops of carbonate-bearing
475 assemblages compared to those in the crater floor fractured 2 unit, indicating a higher spectral
476 abundance of Fe/Mg-phyllosilicate relative to the phase imparting the 2.2 μm absorption
477 (Figure 17). It is unclear if the 2.2 μm absorptions in VNIR spectra of carbonate-bearing
478 assemblages are caused by hydrated silica and/or Al-phyllosilicate (Figure 17). As noted by
479 previous studies (Goudge et al., 2015) carbonate spectral absorptions are more spatially
480 widespread in the northern fan deposit relative to the western delta deposit (Figures 8-10 and
481 S6-S7 compared to Figures 11 and S7).

482

483 *4.2.2 Morphology, thermal inertia, and geologic context*

The morphological properties and stratigraphic relationships between the individual units in the Jezero delta are detailed in Stack et al. (2020). The units are, from stratigraphically youngest to oldest, the delta blocky, thickly layered and truncated curvilinear layered, thinly layered, and layered rough units. In the western delta, clear bedrock exposures of carbonate-bearing material at spatial resolutions measurable using CRISM are present in the delta blocky (Figure 8) and delta truncated curvilinear (Figure 9) units. These carbonate-bearing outcrops have previously been reported by (Ehlmann et al., 2009, 2008b; Goudge et al., 2015). Other locations with VNIR spectra consistent with the presence of carbonate are undifferentiated smooth, dark-toned material (Figures 10, S6). Light-toned bedrock exposures of carbonate-bearing material also have moderate thermal inertia (Figures 8-9) while carbonate-bearing undifferentiated smooth material has low thermal inertia (Figures 10, S6), consistent with the interpretation that the undifferentiated smooth material is unconsolidated relative to the light-toned bedrock. In the northern fan deposit, carbonate-bearing rock is widespread, both in moderate thermal inertia (Figure 11) and low thermal inertia (Figure S7) material. All outcrops of deltaic carbonate-bearing rocks are not morphologically distinct from other rocks within their units, nor do they show notable stratigraphic relationships with other rocks in their units. It is unclear whether the undifferentiated smooth material is eroded unconsolidated material from the deltaic bedrock units, or if it has experienced a different authigenic or detrital formation history compared to those deltaic bedrock units.

4.3 Margin fractured unit and proximal aeolian bedforms

4.3.1 VNIR spectra

506 Outcrops of bedrock in the margin fractured unit have VNIR absorption features
507 consistent with a mixture of carbonate, phyllosilicate, and possible olivine, as has been
508 reported by previous studies (Goudge et al., 2015; Horgan et al., 2020a). The presence of
509 carbonate is indicated by absorptions centered at 2.3 and 2.5 μm. While spectra of the margin
510 fractured unit have the lowest 2.3/2.5 μm absorption band depth ratios within Jezero crater,
511 their relative strength is consistent with a mixture of carbonate and phyllosilicate (Figures 4-6,
512 S1-S3). This is further supported by the narrow shape of the 2.3 μm feature relative to that
513 typical of pure carbonate (Bishop et al., 2013) (Figure 17). The low 2.3/2.5 μm band depth ratio
514 values in the margin fractured unit are also found in the ROB unit elsewhere in Nili Fossae
515 (Figures 19, S10), including in the ROB unit immediately outside of Jezero (Figure 19a),
516 indicating that the carbonate spectral strength in the margin fractured unit is nonunique in a
517 regionally context. As indicated by Horgan et al., (2020a), the 1.0 μm feature in the margin
518 fractured unit could either be caused by olivine and/or siderite (Figures 4-6, 17, S1-S3) and
519 without clear absorption features of olivine in other outcrops of this unit, inferring that this
520 mineral is the cause of the 1.0 μm absorption is potentially less valid than in the crater floor
521 fractured 2 unit. However, the lack of clear contacts between the ROB unit draping into Jezero
522 crater and the margin fractured unit does favor the interpretation that the 1.0 μm absorption in
523 the margin fractured unit is due to olivine, which is present throughout the ROB unit.
524 The large aeolian bedforms immediately proximal to the margin fractured unit contain
525 very similar VNIR spectra to margin fractured bedrock (Figures 7, S4-S5), indicating that they
526 may be locally sourced sediments composed of the same carbonate-phyllosilicate-possible
527 olivine mixture as the margin fractured unit. Many aeolian bedforms in Jezero have similar VNIR

spectral properties as proximal bedrock, indicating that they are often locally sourced from erosion of that bedrock (Arvidson and Christian, 2020).

4.3.2 Morphology, thermal inertia, and geologic context

The margin fractured unit has a fractured, sometimes rubbly, and occasionally ridged appearance similar to the crater floor fractured 2 unit (Figures 4-6, S1-S3). It has high thermal inertia compared to other units in Jezero crater (Figure 2b-c) and rocks with the strongest carbonate VNIR absorption features also have high thermal inertia (Figure 2a). There are no visible contacts between the margin fractured unit and the crater floor fractured 2 unit, nor the margin fractured unit and the ROB unit that drapes into Jezero crater (Goudge et al., 2015), with cross sections showing a gradational relationship in all cases (Figure 18). The morphology, high thermal inertia, and VNIR spectral signatures resemble the ROB unit (Goudge et al., 2015), including the ROB component immediately north of the crater rim from the margin fractured unit, and the component of the ROB that drapes into Jezero crater (Figure 2b-c). Many of the strongest carbonate absorption features in this unit are associated with elevation of the estimated maximum Jezero lake level (Horgan et al., 2020a). The delta blocky unit outcrops stratigraphically above the margin fractured unit and there are clear contacts in many locations (e.g., Figure 4c). In one area, a cross-section exposure of the margin fractured unit shows possible banding similar to that seen in the crater floor fractured 1 unit (Figure 3b), though these may actually be diagenetically-generated ridges rather than beds. The largest margin fractured unit outcrops contain either plateaus (e.g., Figures 5, S1-S2) or mounds of bedrock bearing the characteristic fractured morphology of the unit (e.g., Figures 4, 6, S3).

The large aeolian bedforms proximal to the margin fractured unit have low thermal inertia—which is expected for unconsolidated material—and overly margin fractured bedrock in many locations (Figure S5c). These aeolian bedforms are longer wavelength than those in lower elevations of western Jezero crater, likely due to a combination of physical properties of the unconsolidated grains and the predominant wind patterns in Jezero crater (Day and Dorn, 2019).

4.4 Carbonate-bearing rocks outside of Jezero

We find outcrops of carbonate-bearing rocks in the ROB unit with strong spectral similarities to carbonates in the crater floor fractured and margin fractured units in Jezero crater (Figure 19, S10). The 2.3/2.5 μm band depth ratios in carbonate-bearing rocks outside of Jezero crater are equivalent to those found in the margin fractured unit (Figure 19, S10). This is true in outcrops of the ROB 100-200 km northeast of Jezero crater (Figure 19b-d), outcrops of the ROB immediately northwards of the Jezero crater rim from the margin fractured unit (Figure 19a), and outcrops of ROB that drape into Jezero crater (Figure 19a). These low 2.3/2.5 μm band depth ratios span extensive amounts of outcrop regionally (Figure 19b, S10), and indeed may be present in many outcrops without CRISM FRT, HRL, FRS, HRS, or ATO image coverage. The spectral endmembers associated with CRISM pixels with BD2500_2 values greater than 0.005 inside and outside of Jezero crater are similar and contain absorptions consistent with the presence of carbonate, Fe/Mg-phyllosilicate, and olivine (Figure 19e). In summary, we find extensive carbonate-bearing rocks in the ROB unit that resemble the carbonate spectral signatures of the margin fractured unit.

572

573 **5.0 Discussion**

574 Our results indicate that it is equally likely that carbonates in Jezero crater formed via
575 groundwater alteration rather than fluviolacustrine precipitation, but neither of these
576 hypotheses can be definitively proven using orbital data. We include pedogenic carbonate
577 formation in the groundwater formation scenario, as the fluids causing carbonate formation
578 would be present in the subsurface, though they made have originally precipitated on the
579 surface and percolated downwards. It is also possible that a hypothesis intermediate to
580 groundwater and fluviolacustrine carbonate formation may be true, whereby some carbonate
581 formed in the subsurface and some formed as fluviolacustrine sediment, as discussed by
582 Horgan et al., (2020a).

583 In this section, we evaluate the observations that favor carbonate formation by
584 groundwater (Sections 5.1 and 5.2) and carbonate formation in a fluviolacustrine environment
585 (Sections 5.1 and 5.3). We discuss the facies that could preserve biosignatures in either scenario
586 based on Earth analogs (Section 5.4). Finally, we discuss the possibility that some carbonate in
587 Jezero crater and the surrounding Nili Fossae region may have formed under the conditions of
588 the modern martian atmosphere (Section 5.5; Kelemen et al., 2020a).

589

590 *5.1 Thickness of the margin fractured unit*

591 The margin fractured unit is topographically higher than the crater floor fractured 2 unit
592 (Horgan et al., 2020a; Figure 18). If the margin fractured and crater floor fractured 2 units are
593 both part of the ROB unit, then this topographic difference could be caused by ROB unit

thickness variations (Scenario 1) or topographic variations in the underlying unit draped by the ROB unit (Scenario 2). If unit thickness variations are the cause of topographic variations, then the margin fractured unit would be ~10-100 times thicker than the ROB is elsewhere in Nili Fossae and ~3-6 times thicker than the ROB is in Libya Montes (Kremer et al., 2019). Another possible explanation for the observed topographic difference is that 100s of meters of lithified fluviolacustrine sediments have been emplaced atop the ROB unit (Scenario 3).

5.1.1 Scenario 1: The margin fractured unit is a thick outcrop of ROB unit

Our observations favor Scenario 1 over Scenario 2, as some margin fractured outcrops show possible banding (e.g., Figure S3b, S4a) and are ~200 meters thick (e.g., Figure 18 Cross Section E). Perhaps the ROB unit was originally 100s of meters thick when originally emplaced, similar to its less-eroded outcrops in Libya Montes (Kremer et al., 2019), and has been substantially eroded to <10% of its original thickness in the Nili Fossae region. This interpretation is consistent with the typical material properties of high TI clastic rocks on Mars, which are interpreted to be friable, eroding faster than surrounding rocks to expose relatively dust-free surfaces (Rogers et al., 2018).

If Scenario 1 (Figure 18) is the correct interpretation for topographic variability between the margin fractured and crater floor fractured units, then the margin fractured unit component of the ROB unit was more cemented and/or protected from erosion compared to the ROB elsewhere in Jezero crater and the Nili Fossae region. Because the delta blocky unit is locally stratigraphically above the margin fractured unit (e.g., Figure 4c), it is possible that the delta originally covered part of the margin fractured unit, protecting it from erosion.

Furthermore, coverage by the delta and/or any since-eroded overlying units would likely provide a pathway for later groundwater flow. This is similar to the proposed setting for past enhanced groundwater flow in VRR, Gale crater, where the contact between the Murray Formation and the Stimson Formation is thought to have provided a pathway for groundwater, which cemented VRR relative to surrounding rocks and also protected it from physical erosion while the overlying material was being removed (Bryk et al., 2019; Rampe et al., 2020). This constitutes another possible similarity between the origins of VRR in Gale crater and the margin fractured unit in Jezero crater. The position of the margin fractured unit immediately interior to Jezero crater's rim also increases the likelihood that this material experienced enhanced groundwater alteration relative to the ROB unit further interior to Jezero crater, as well as outside of Jezero crater, because bedrock surrounding impact craters is fractured and more permeable than non-impacted bedrock (Collins, 2014). Such enhanced permeability would increase groundwater flow around and into Jezero crater, possibly resulting in enhanced mineral dissolution, disequilibria from fluid mixing, and more favorable redox conditions for chemolithotrophic microorganisms. These observations are consistent with enhanced groundwater alteration producing the topographic (Figure 19), VNIR spectral, and thermal inertia properties of the margin fractured unit, similar to hypotheses proposed for the formation of VRR (Bryk et al., 2019; Fraeman et al., 2020b, 2020a; Jacob et al., 2020; Rampe et al., 2020), but under less acidic aqueous conditions. Differences in fluid chemistry could cause groundwater-driven formation of hematite in the Murray Formation under oxidizing conditions, but cause groundwater-driven formation of carbonate in Jezero crater given high dissolved CO_2 concentrations.

638

639 *5.1.2 Scenario 2: The margin fractured unit is the ROB unit draping underlying topography*

640 Our observations do not rule out Scenario 2 (Figure 19), where topographic differences
641 between the margin fractured and crater floor fractured units are controlled by topographic
642 variations of an underlying unit. Fresh ~40 km diameter impact craters do not typically have
643 shelves immediately interior to their rims, therefore this is unlikely to be the cause of any
644 underlying topographic variability. Furthermore, if there was a thick unit emplaced beneath the
645 margin fractured unit, it would likely be present within the Nili Fossae regional stratigraphy
646 (Ehlmann and Mustard, 2012) between the basement and ROB units; no such unit is observed
647 outside of Jezero crater. Still, Jezero crater has been filled by ~1 km of material relative to the
648 shape expected of a fresh impact crater of its size (Fassett and Head, 2005; Schon et al., 2012)
649 and the nature of that material remains ambiguous, as it would also likely outcrop between the
650 basement and ROB units if it was emplaced across the entire Nili Fossae region. The ROB drapes
651 topography across the entire Nili Fossae region, as well as in Libya Montes (Kremer et al., 2019),
652 with outcrop thicknesses from ~1-25 meters in Nili Fossae and ~50-100 meters in Libya Montes.
653 It is therefore possible that the topography of the margin fractured unit compared to the crater
654 floor fractured unit is entirely dictated by underlying topography, without any thickness
655 variations greater than ~100 meters in the unit itself. If this is the case, and the unit is only ~10
656 meters thick, it is possible that the Radar Imager for Mars' Subsurface Exploration (RIMFAX;
657 Hamran et al., 2020) might see an unconformable contact between it and the underlying unit
658 that controls topography.

659

660 *5.1.3 Scenario 3: The margin fractured unit is lithified fluviolacustrine sediment*

661 Scenario 3, where thickness differences between the margin fractured and crater floor
662 fractured units are caused by deposition of fluviolacustrine sediments, is another possible
663 explanation for the observations reported here (Figure 18). As proposed in the study detailing a
664 fluviolacustrine origin hypothesis for the margin fractured unit carbonates (Horgan et al.,
665 2020a), these sediments could be deposited in a shallow water setting during the highstanding
666 period of ancient Lake Jezero. Such carbonate-bearing fluviolacustrine sediments form
667 topographic highs at the former margins of lakes on Earth (e.g., Antalya region, SW Turkey;
668 Glover and Robertson, 2003), therefore this could be the cause of the thickness variations
669 reported here (Figure 18). In this scenario, hundreds of meters of lithified fluviolacustrine
670 sediment could be protected from erosion by overlying deltaic material and/or a since eroded
671 overlying unit, similar to the argument presented in Scenario 1. This fluviolacustrine sediment
672 would be deposited before the outflow channel in eastern Jezero crater was breached.
673 Authigenic and detrital sedimentation rates on early Mars are unconstrained, therefore we do
674 not estimate the amount of time required for deposition of 100s of meters of lithified
675 fluviolacustrine sediments in the Jezero paleolake before the breach event occurred. However,
676 the Curiosity rover has traversed ~300 meters of a fluvial, deltaic, lacustrine, and aeolian
677 sediments in Gale crater, which is also a crater lake basin, therefore a paleolacustrine
678 sedimentary sequences 100s of meters thick is not unprecedented in the martian geologic
679 record.

680 In summary, the topographic difference between the margin fractured and crater floor
681 fractured units favors either cementation by groundwater, draping of underlying topography,

682 or fluviolacustrine sediment deposition, depending on the preferred interpretation of the cross
683 sections presented here (Figure 18). Both the groundwater alteration and fluviolacustrine
684 scenarios (Scenarios 1 & 3) have high potential to preserve biosignatures. In the groundwater
685 scenario (Scenario 1), biosignatures would be entombed in mineralized veins where previously
686 habitable alkaline groundwater flowed, whereas in the fluviolacustrine scenario (Scenario 3),
687 biosignatures would be entombed in fine-grain sedimentary carbonates that authigenically
688 formed in the lake water column.
689
690 *5.2 Formation of carbonates by alkaline groundwater*
691 It is possible that the margin fractured and crater floor fractured 2 units are both part of
692 the ROB unit. This interpretation is based on the morphologic, VNIR spectral, and stratigraphic
693 properties shared by these units. Furthermore, the ROB unit drapes into Jezero crater and has
694 no visible contact or morphologic differences with the margin fractured unit (Figure 18),
695 implying that they are the same unit. The ROB unit also has carbonate absorptions of similar
696 strength to those found in the margin fractured unit both immediately outside of Jezero crater
697 (Figure 19a), which are contiguous with the margin fractured unit, and in other locations of this
698 unit in Nili Fossae (Figure 19b-d). 2.3/2.5 μm band depth ratios also show no significant
699 differences between carbonate-bearing mineral assemblage spectra in the margin fractured
700 unit, the ROB unit immediately outside of Jezero crater, the ROB unit draping into the Jezero
701 crater rim, or the ROB unit 100-200 km northeast of Jezero crater (Figure 19). The lack of any
702 contacts between the margin fractured and crater floor fractured units, as well as the VNIR
703 spectral and morphological similarities between these units, implies a shared carbonate

formation process. This interpretation is consistent with past interpretations of the relationship between the margin fractured, crater floor fractured 2, and ROB units (Ehlmann et al., 2009; Goudge et al., 2015).

Spectral variations between the margin fractured and crater floor fractured 2 units could be attributed to groundwater alteration and cementation. Groundtruthing of orbitally-measured VNIR spectra by Curiosity in Gale crater demonstrates that variations in groundwater activity can substantially alter VNIR spectral properties of rocks without appreciably changing their modal mineralogy (Fraeman et al., 2020b, 2020a; Rampe et al., 2020). The Curiosity rover recently completed a campaign to characterize the Vera Rubin ridge (VRR), which had originally been called the hematite ridge based on its strong 0.86 μm absorption band in CRISM data, which was attributed to hematite (Fraeman et al., 2013). This extensive campaign indicated that VRR appears to be a component of the more widespread Murray Formation, but has experienced episodes of groundwater alteration that cemented the rocks in the ridge to make them more resistant to erosion relative to other rocks in the Murray Formation (David et al., 2020; Fraeman et al., 2020a, 2020b; Frydenvang et al., 2020; Horgan et al., 2020b; Jacob et al., 2020; L'Haridon et al., 2020; McAdam et al., 2020; Morris et al., 2020; Rampe et al., 2020; Thompson et al., 2020). This has resulted in less coverage by unconsolidated material and higher thermal inertia relative to the majority of the Murray Formation (Edwards et al., 2018). This same groundwater alteration also increased the crystallinity of hematite in the ridge, producing a strong 0.86 μm absorption attributed to hematite without substantially changing rock modal mineralogy from that of the rest of the Murray Formation (Rampe et al., 2020). Indeed, hematite modal abundances in drill cores in and near VRR ranged from 3-15% (Rampe

et al., 2020), compared to 1-14% elsewhere in the Murray Formation (Bristow et al., 2018; Rampe et al., 2017). Stoer, the drill core sampled during the VRR campaign with the highest hematite modal abundance, was not located on a part of VRR with a particularly strong 0.86 μm hematite absorption in CRISM data (Fraeman et al., 2020b, 2020a; Rampe et al., 2020). Based on these results, physical and spectral mixing of phases, variations in cementation and grain sizes of rock components, variability of coverage by unconsolidated material, and differences in spatial resolutions between datasets can manifest in substantial differences between orbital interpretations and groundtruth.

A similar groundwater-driven history would explain the properties of the margin fractured unit relative to the crater floor fractured 2 unit, though under different fluid chemistries compared to groundwater in the Murray Formation. The margin fractured unit is high-standing compared to the crater floor fractured 2 unit (Figure 18), indicating that it is cemented and more resistant to erosion. It also has high thermal inertia relative to the crater floor fractured unit (Figure 2b-c). Margin fractured unit rocks with the strongest VNIR carbonate absorptions also have high thermal inertia (Figure 2a-c), just as VRR rocks with the strongest VNIR hematite absorptions have high thermal inertia (Figure 2d-f). The ROB unit has outcrops of high thermal inertia rocks with strong VNIR carbonate absorptions both inside and outside of Jezero crater (Figure 19). Because there is no clear contact between these rocks and those with identical properties in the margin fractured unit, it is likely that they constitute the same unit. In sedimentary rocks, high thermal inertia can be attributed to lower coverage by unconsolidated material as well as increased rock cementation. The topographically-highstanding nature of the margin fractured unit indicates that cementation is likely a factor

affecting its thermal inertia, but the particularly light-toned nature of these rocks compared to others in Jezero crater indicates that they are also less covered by unconsolidated material. These properties are shared by VRR in Gale crater. As such, a simple explanation for our observations is that the margin fractured unit is the same as the crater floor fractured 2 and ROB units, but has experienced more cementation and crystallinity enhancement by groundwater alteration. This, combined with less coverage by unconsolidated material, is likely what generates its strong VNIR absorptions consistent with carbonate. It is possible that increased crystallization by groundwater could erase or overprint biosignatures in these rocks (McMahon et al., 2018), but increased cementation of the rocks could also make them resistant to physical weathering and decrease their permeability, lowering susceptibility to later groundwater infiltration episodes that could overprint biosignatures. The cementing material could also be authigenic carbonate precipitated from alkaline groundwater with high dissolved carbonate concentrations, which could preserve biosignatures of microorganisms inhabiting the groundwater (McMahon et al., 2018; Summons et al., 2011).

5.3 Formation of fluviolacustrine carbonates

A fluviolacustrine origin for carbonates in the margin fractured unit of Jezero crater (Horgan et al., 2020a) is equally as likely as groundwater carbonate formation given orbital observations. If the 1.0 μm absorption in this unit is caused by presence of olivine rather than presence of siderite, as seems probable based on the continuity between the margin fractured and ROB units, then authigenic lacustrine carbonates may be mixed with detrital mafic material that is present in the Jezero delta (Brown et al., 2020; Ehlmann et al., 2008a; Goudge et al.,

770 2017; Horgan et al., 2020a; Parente et al., 2019). Evidence for a fluviolacustrine origin for
771 carbonates in the margin fractured unit includes the association of strong 2.5 μm absorptions
772 and low 2.3/2.5 μm band depth ratios near the estimated shoreline of the Jezero paleolake at
773 its highstand (Horgan et al., 2020a). However, similar carbonate spectral features can be seen in
774 CRISM data or the ROB unit elsewhere in Nili Fossae (Figures 19, S10). Horgan et al., (2020a)
775 also present evidence for spectral variability in the margin fractured unit as a function of
776 distance from the inlet channel, but these observations could also be explained by variations in
777 groundwater activity, cementation, and coverage by unconsolidated material. Based on these
778 observations, as well as similarities in the relationship between VNIR spectral properties and
779 thermal inertia in the margin fractured unit in Jezero crater and VRR in Gale crater (Figure 2),
780 we consider a groundwater origin for enhanced VNIR carbonate absorptions to be equally as
781 likely as a fluviolacustrine origin. In this scenario, the presence of deep VNIR carbonate
782 absorptions between the highstand and breach levels of the Jezero paleolake is coincidental.
783 Deposition of ~200-300 meters of fluvial, deltaic, and lacustrine sediments during the
784 highstand of the paleolake in Jezero crater could explain the greater thickness of the margin
785 fractured unit relative to other carbonate-bearing rocks in Jezero crater and the Nili Fossae
786 region (Section 5.1.3). In this scenario, the Jezero paleolake must have existed at its highstand
787 level for sufficient amounts of time for this sediment to be deposited. Sedimentation rates vary
788 widely on Earth and are largely controlled by climate and substrate properties. Since both of
789 these parameters are largely unconstrained for Noachian Mars, it is difficult to accurately
790 assess the amount of time required for ~200-300 meters of sediment to be deposited in the
791 paleolake during its highstand. However, the Curiosity rover has traversed ~300 meters of

fluvial, deltaic, aeolian, and lacustrine sediments at Mount Sharp, therefore it is plausible that a similarly thick carbonate-bearing sedimentary sequence could have been deposited in Jezero crater during continuous or intermittent lake-forming eras. We conclude that a fluviolacustrine sedimentary origin for carbonates in the margin fractured unit is plausible based on orbital observations, but that carbonate formation by alkaline groundwater is equally likely based on similarities between carbonates within and outside of Jezero crater, as well as similarities between the rock properties of VRR and the margin fractured unit as observed from orbit.

5.4 Possible biosignatures from subsurface habitable environments

Our results suggest multiple possible formation mechanisms for the carbonates in Jezero crater, some of which may have created taphonomic windows conducive to biosignature preservation. It has been suggested that the stronger VNIR absorptions of carbonate in the margin fractured unit represent a carbonate deposit that formed in a fluviolacustrine environment (Horgan et al., 2020a). In this scenario, carbonate precipitation would have a high likelihood of preserving biosignatures like stromatolites and organic matter if the Jezero paleolake was inhabited at the time of carbonate formation. Our results do not preclude this formation mechanism, but indicate that it is equally likely that these carbonates formed from alkaline groundwaters, which commonly form subsurface habitable environments on Earth. While the surface of Mars was sporadically habitable (Wordsworth et al., 2021), deep subsurface environments likely constituted the longest-lived habitable environments on Mars (Michalski et al., 2018, 2013; Tarnas et al., 2018), providing a refugia for martian life. Near-subsurface groundwaters that connect to deep subsurface groundwater through liquid veins that cross-cut the cryosphere would introduce life from deep subsurface refugia into near-surface

environments, potentially entombing it in mineralized veins. This possible connectivity to deep subsurface refugia makes groundwater-derived carbonates particularly compelling targets for biosignature preservation in Jezero crater. Minerals precipitated around surface springs from subsurface fluid systems also preserve biosignatures on Earth (Hays et al., 2017), and spring-fed carbonate precipitants in Jezero crater would have high biosignature preservation potential.

If the margin fractured, crater floor fractured 2, and ROB units are the same rock unit, then carbonates in the margin fractured unit would have effectively the same material biosignature preservation potential as carbonates in the crater floor fractured or ROB units, although local conditions would dictate the likelihood for biosignatures to exist within different carbonate-bearing outcrops. The likelihood that these units contain biosignatures is therefore dictated by the temperature of any alteration by groundwater, as well as redox compound availability in those possible aqueous solutions. Mafic and ultramafic rock is carbonated on Earth under both habitable and uninhabitable conditions. Carbonate-bearing facies in subseafloor altered mafic and ultramafic rocks preserve biosignatures (Ivarsson et al., 2018, 2012; Klein et al., 2015), as do carbonates in terrestrial serpentinites formed by groundwater alteration of ophiolites (Newman et al., 2020), and cross-cutting alteration veins in terrestrial mafic and granitic sedimentary rocks that have been altered by groundwater (Drake et al., 2017; McKinley, 2000; Onstott et al., 2019).

5.5 Possibility of carbonate formation in modern day Mars atmospheric conditions

Kelemen et al., (2020a) presented the hypothesis that carbonation of olivine, particularly in the Nili Fossae region, could occur under the conditions of the modern day

martian atmosphere at temperatures > 0 °C. Under these conditions, carbonation of olivine would occur without precipitation of serpentine, brucite, or talc, which have not been unambiguously confirmed to exist in the ROB unit. However, there is spectral evidence of either talc or saponite in the ROB unit, with some authors favoring the interpretation of the presence of talc (Brown et al., 2010; Viviano et al., 2013). Small outcrops of Mg-rich serpentine have been reported in the ROB unit (Ehlmann et al., 2010; Leask et al., 2018). Furthermore, if more widespread Fe-rich serpentine were present, it could not be differentiated from many other phyllosilicates in the wavelength range measured by CRISM (Figure 17; Calvin and King, 1997; Ehlmann et al., 2010). Additionally, groundtruthings of orbital compositional measurements on Mars (Arvidson et al., 2008, 2006; Bristow et al., 2018; Carter and Poulet, 2012; Clark et al., 2007; Dobrea et al., 2012; Fox et al., 2016; Fraeman et al., 2016, 2013; Glotch et al., 2006; Morris et al., 2010, 2006; Rampe et al., 2020, 2017; Rice et al., 2010; Ruff et al., 2011; Squyres et al., 2008; Wang et al., 2006; Wray et al., 2009) indicate that CRISM analysis can accurately identify the *presence* of minerals in rocks on Mars, but cannot be used as strong evidence for the *absence* of minerals due to phase mixing effects and obscuring by dust.

While orbital evidence cannot unambiguously confirm or deny this hypothesis, it may be inconsistent with the presence of widespread olivine on the surface of Mars (Ody et al., 2013) with no reported associated secondary minerals. Many of these unaltered olivine provinces are at more equatorial latitudes than the Nili Fossae region, where temperatures are greater than 0 °C for a higher portion of each martian year. However, due to precession of Mars on ~Myr timescales (Laskar et al., 2004), the modern day latitudinal distribution of olivine-bearing material on the surface of Mars may not correspond to the cumulative relative temperatures

859 experienced by those materials on Myr timescales. Still, if the modern day atmosphere of Mars
860 could carbonate olivine to sufficiently thick skin depths to be measurable by CRISM, it is unclear
861 why this would manifest in orbital carbonate identifications in Nili Fossae, but not in other
862 olivine-bearing regions of Mars. It is possible that the ROB unit in Nili Fossae is uniquely
863 permeable to the atmosphere compared to other olivine-rich rocks on Mars, which would
864 increase carbonate rind thickness (Cannon et al., 2015; Salvatore et al., 2013). However, many
865 of these olivine-rich terrains are likely clastic (Rogers et al., 2018) and therefore have similar
866 permeabilities to the ROB unit, which is also likely clastic (Kremer et al., 2019). Nonetheless,
867 carbonate rind formation in the ROB unit under modern Mars atmospheric conditions cannot
868 be ruled out.
869
870 **6.0 Conclusions**
871 In Table 1, we compile observations of the margin fractured unit derived from orbital data and
872 interpret whether they favor groundwater or fluviolacustrine origins for carbonates there. The
873 conclusions of this study are summarized below.
874
875 1) Carbonate and hydrated silica-bearing units in Jezero crater. There are VNIR spectral
876 absorptions consistent with carbonate in CRISM data covering (1) high TI bedrock in the margin
877 fractured unit (Figures 4-6, S1-S3), (2) large aeolian bedforms proximal to the margin fractured
878 unit (Figures 7, S4-S5), (3) the delta blocky unit (Figure 8), (4) the delta truncated curvilinear
879 unit (Figure 9), (5) undifferentiated smooth material on the western delta (Figures 10, S6), (6)
880 the delta layered rough unit (Figures 11, S7), (7) moderate TI bedrock in the crater floor

fractured 2 (CFF 2) unit (Figures 12-13, S8), and (8) low TI dunes and unconsolidated dark-toned material in the CFF 2 unit (Figure 14). We also find five previously unreported outcrops of hydrated silica in the same dark-toned material that Tarnas et al. (2019) and Dundar et al. (2019) reported hydrated silica in (Figures 15-16, S9).

2) Minerals in assemblage with carbonate in Jezero crater. Carbonate-bearing rocks in the crater floor fractured 2 unit also have absorption features consistent with a mixture of olivine, carbonate, Fe/Mg-phyllosilicate(s), and hydrated silica and/or Al-phyllosilicate (Figures 12, 14, 17, S8). VNIR spectra with carbonate absorptions in the deltaic unit have deeper and narrower 2.3 μm absorptions compared to carbonate spectra elsewhere in the crater (Figures 1, 8-11 17, S6-S7), implying a higher spectral abundance of Fe/Mg-phyllosilicate(s). These spectra also have 2.2 μm absorption features consistent with hydrated silica and/or Al-phyllosilicate and a broad 1.0 μm band consistent with olivine and/or siderite (Figure 17). The margin fractured unit and proximal aeolian bedforms have spectra consistent with a mixture of olivine and/or siderite, carbonate, and Fe/Mg-phyllosilicate(s) (Figures 4-6, 17, S1-S3). As reported by Horgan et al. (2020a), rocks in the margin fractured unit have the lowest 2.3/2.5 μm band depth ratios in Jezero crater, consistent with a higher spectral abundance of carbonate (Figure 19a).

3) Bedrock with strong carbonate absorptions has high thermal inertia. Margin fractured unit outcrops with the deepest 2.5 μm absorptions also have high thermal inertia relative to surrounding rocks, similar to the relationship between the 0.86 μm absorption and thermal inertia in VRR at Gale crater (Figure 2), implying that groundwater alteration/cementation may

903 generate the topographic features of the margin fractured unit as well as its spectral properties,
904 as has been reported via the Curiosity rover campaign at VRR (Fraeman et al., 2020a). It is
905 possible that this groundwater alteration/cementation would not increase the modal
906 abundance of carbonate in the margin fractured unit, but rather would increase carbonate
907 crystallinity as well as rock cementation, resulting in lesser coverage by unconsolidated material
908 and increasing of the 2.5 μm absorption band depth. These groundwater-induced physical
909 differences are what cause the deep 0.86 μm absorption in VRR (Fraeman et al., 2020b, 2020a;
910 Horgan et al., 2020b; Jacob et al., 2020) without appreciably increasing the modal abundance of
911 hematite in VRR compared to the rest of the Murray Formation (Bristow et al., 2018; Rampe et
912 al., 2020, 2017).
913
914 4. Carbonates outside of Jezero crater are spectrally similar to margin fractured unit
915 carbonates. Carbonates in the margin fractured unit have the lowest 2.3/2.5 μm band depth
916 ratios observed inside Jezero crater. We find widespread outcrops with similar 2.3/2.5 μm band
917 depth ratios in the ROB unit 100-200 km NNE of Jezero crater (Figure 19b-d, S10), as well as
918 immediately outside of Jezero crater (Figure 19a), showing that the spectral signatures of the
919 margin fractured unit are not unique in a regional context. While we do not rule out the
920 possibility of a fluviolacustrine origin for carbonates in the margin fractured unit, we find that it
921 is equally likely that the margin fractured unit is part of the ROB unit, which drapes into Jezero
922 crater and has no clear contacts or major spectral differences with the margin fractured unit.
923 Whatever alteration has generated the low 2.3/2.5 μm absorption depth ratios in these rocks
924 has also occurred elsewhere in the ROB in Nili Fossae.

925

926 5. The margin fractured unit is likely 250-300 meters thick. The margin fractured unit is
927 topographically higher than the crater floor fractured unit (Horgan et al., 2020a). We propose
928 three hypotheses to explain this (Figure 19; Section 5.1). In Scenario 1, the margin fractured
929 unit is an exceptionally (~250-300 meters) thick outcrop of the ROB unit because it has been
930 cemented by groundwater and protected from erosion by overlying deltaic and since-eroded
931 material. There may have been enhanced groundwater flow at the contact of the underlying
932 ROB unit and overlying deltaic unit, similar to what has been proposed between the underlying
933 Murray Formation and overlying Stimson Formation in Gale crater to enhance groundwater
934 activity, cementing the underlying material (Bryk et al., 2019; Fraeman et al., 2020b, 2020a;
935 Jacob et al., 2020; Rampe et al., 2020). ROB outcrops in Libya Montes are up to ~100 meters
936 thick (Kremer et al., 2019), therefore it is possible that the ROB was originally deposited as a
937 ~300 meter thick unit that has since been heavily eroded, except in the margin fractured unit
938 where it was cemented by groundwater and protected from erosion by overlying units. In
939 Scenario 2, the margin fractured unit is part of the ROB with a regionally-common thickness of
940 1-25 meters. In this case, topographic variations of an underlying unit—which does not outcrop
941 between the basement and ROB units elsewhere in the Nili Fossae region—controls
942 topography. In Scenario 3, the margin fractured unit is thicker than the ROB unit because it is
943 covered by hundreds of meters of lithified fluviolacustrine sediments. This is feasible given that
944 the Mars Science Laboratory Curiosity rover has traversed ~300 meters of a fluvial, deltaic,
945 lacustrine, and aeolian sediments in Gale crater. Based on the outcropping of strong carbonate

absorptions in cross sections of the margin fractured unit (Figs. 18 Cross Section E, S3), we consider Scenarios 1 and 3 to be the most likely.

6. Margin fractured unit carbonates may have formed in a subsurface environment. Our results indicate that a groundwater origin for carbonates in the Jezero crater margin fractured unit is equally likely as a fluviolacustrine origin for these carbonates. In this scenario, carbonates would form via alteration of primary volcanic minerals by groundwater, which commonly forms alkaline waters and habitable subsurface environments on Earth (Kraus et al., 2021; Rempfert et al., 2017; Schrenk et al., 2013) that preserve biosignatures (Ivarsson et al., 2018; Newman et al., 2020; Onstott et al., 2019). Near-surface, carbonate-forming groundwaters that connected to deep subsurface habitable refugia (Michalski et al., 2013; Tarnas et al., 2018) could have transported life towards the surface, where it may be preserved in near-surface mineralized veins of carbonate and other alteration minerals. After billions of years of erosion, the alteration material formed in these possible subsurface habitable environments, including the carbonates in Jezero crater, would now be exposed at the surface. It is also possible that carbonates in the margin fractured unit formed via both groundwater alteration and fluviolacustrine sediment deposition in multiple distinct episodes, as discussed in Horgan et al., (2020a). In-situ investigation by the Perseverance rover will constrain how these carbonates formed, the habitability of their formation conditions, and the likelihood of this material to preserve biosignatures. Subsurface habitability should be considered in this investigation, as rocks from ancient subsurface habitable environments in Jezero crater may preserve biosignatures.

Acknowledgments

Thanks to Jennifer Buz and Christopher Edwards for generating and providing quantitative THEMIS thermal inertia data that was used int this study. J.D.T. was funded by a NASA Postdoctoral Fellowship to work at the NASA Jet Propulsion Laboratory. This research was carried out at the Jet Propulsion Laboratory, California Institute of Technology, under a contract with the National Aeronautics and Space Administration (80NM0018D0004).

Data availability

Datasets used in this research will be made available on Harvard Dataverse.

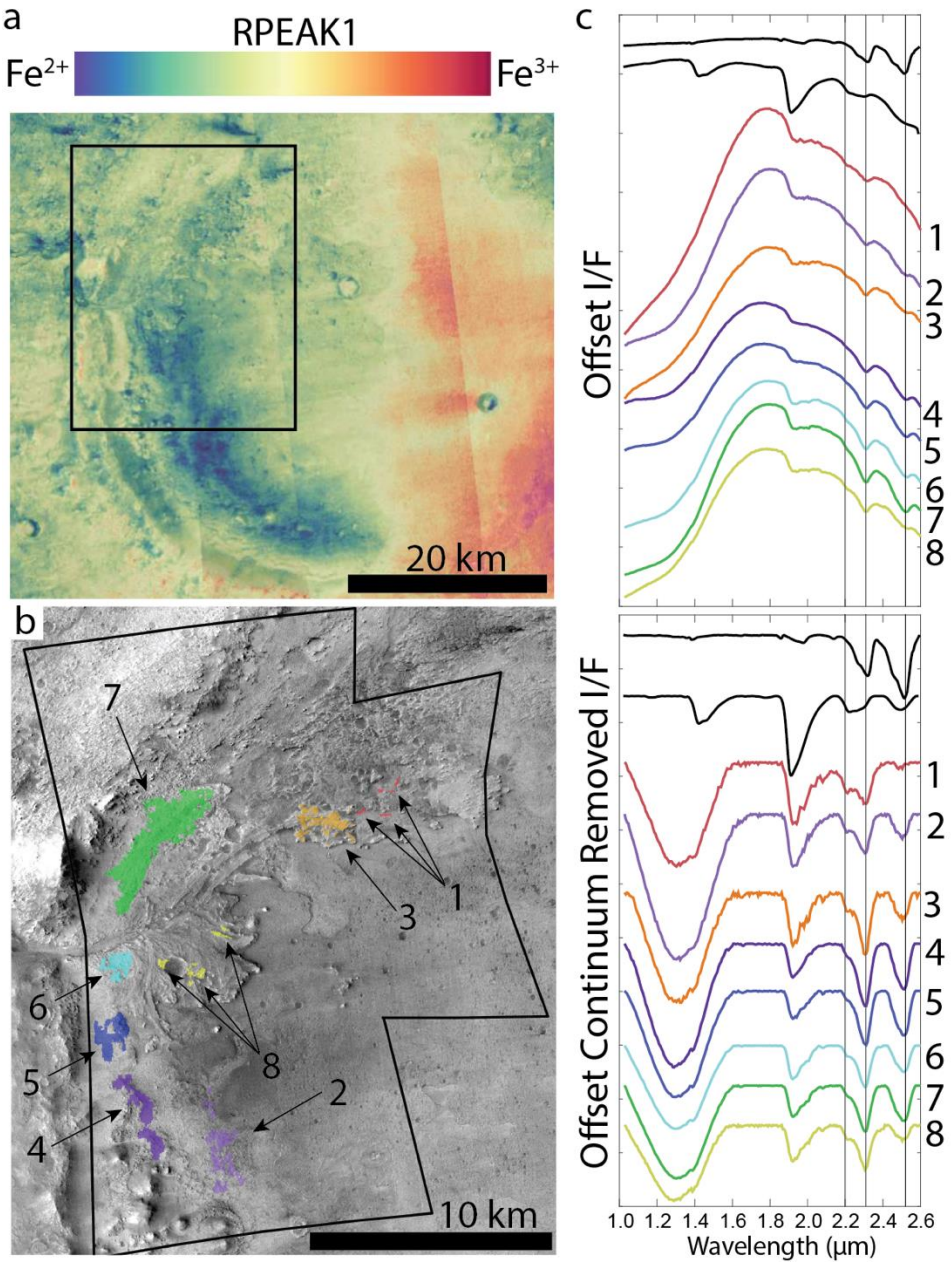

Figure 1 | Overview of Jezero crater carbonate-bearing rocks. (a) RPEAK1 parameter map of CRISM Multispectral TRDR image mosaic, which corresponds to presence of ferric (red color) and ferrous (blue color) Fe. Ferric iron is attributed to presence of martian dust, which occludes spectral signals in the visible-to-near-infrared wavelengths measured by CRISM. The western region of Jezero crater has lower dust coverage, and therefore be less spectrally dominated by dust. (b) Carbonate-bearing rocks are present in the delta truncated curvilinear layered, delta blocky, and undifferentiated smooth units (8), the delta layered rough unit (3), the crater floor fractured 2 unit (2), the margin fractured unit and proximal large aeolian bedforms (4-7) described in Stack et al. (2020). Silica-bearing material is identified in the smooth dark-toned material described in Tarnas et al. (2019). The combined footprints of CRISM images HRL000040FF and FRT000047A3 are shown as black lines. The regions of interest from which

these spectra were extracted are analyzed in greater detail in the Figures covering locations shown in Figure 2. CTX mosaic from Dickson et al. (2018). The colors show the pixels from which the spectra shown in (c) were extracted. Colors and numbers correlate between (b) and (c). (c) Spectra from the University of Massachusetts at Amherst processed CRISM data shown with (bottom) and without (top) continuum removal.

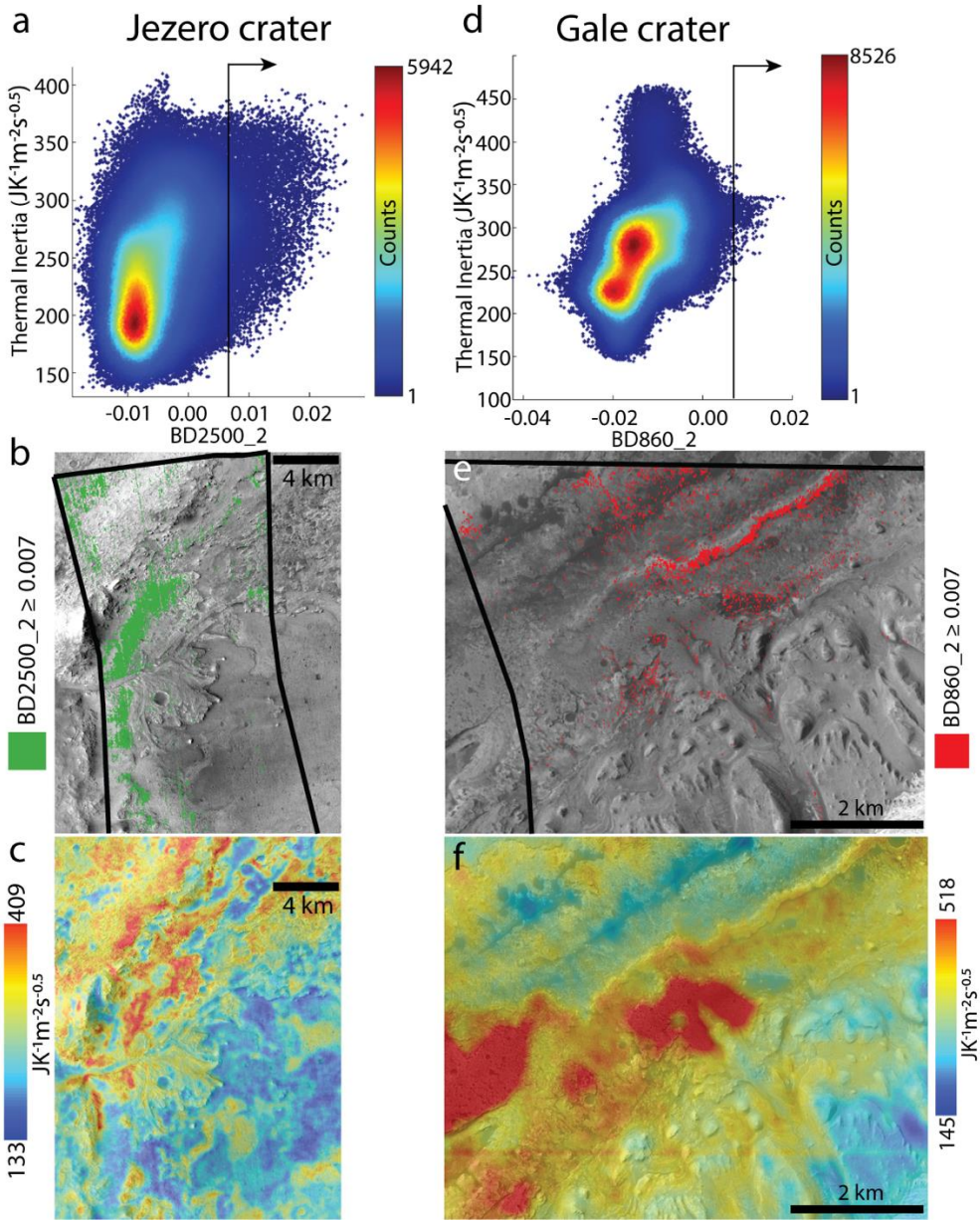

Figure 2 | Similarities between the margin fractured unit in Jezero crater and Vera Rubin ridge in Gale crater. Band parameters are from Viviano-Beck et al., (2014). (a) Relationship between band depth of the 2.5 µm absorption (BD2500_2) in CRISM image HRL000040FF and THEMIS quantitative thermal inertia (TI). The points to the right of the vertical line are the ones that appear in part (b). Pixels with the strongest 2.5 µm absorption band depths also have high TI, except for in regions covered by dunes. (b) CRISM pixels with BD2500_2 values ≥ 0.007,

consistent with the presence of carbonate. The black lines show the outline of CRISM image HRL000040FF. (c) Quantitative TI of the same area shown in (b). (d) Relationship between band depth of the 0.86 μm absorption (BD860_2) in CRISM image FRT0000B6F1 and THEMIS quantitative (TI). The points to the right of the vertical line are the ones that appear in part (e). Pixels with the strongest 0.86 μm absorption band depths also have high-to-moderate TI. (e) CRISM pixels with BD860_2 values ≥ 0.007, consistent with the presence of hematite. The black lines show the outline of CRISM image FRT0000B6F1. (f) Quantitative TI of the same area shown in (e).

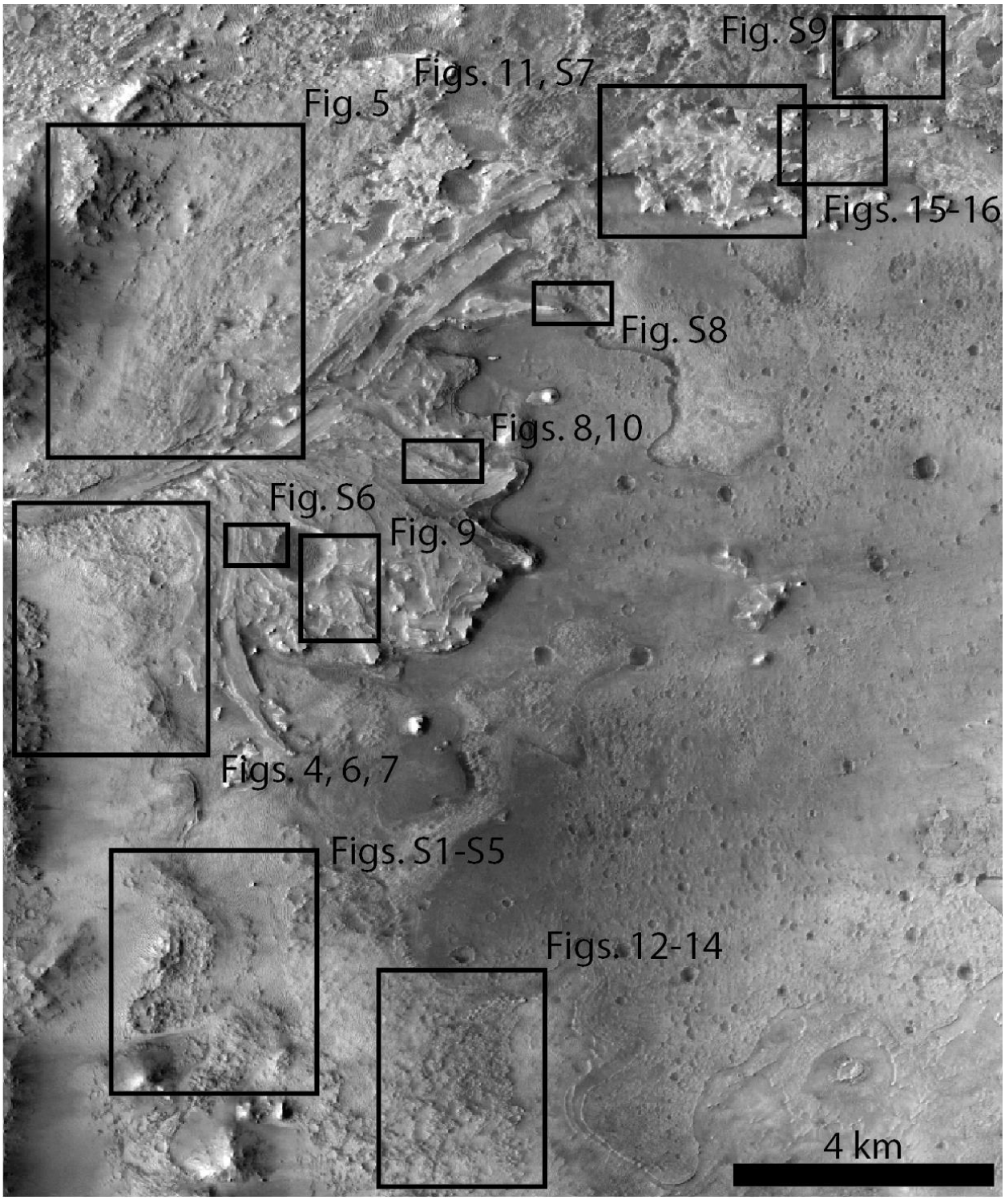

Figure 3 | Locations of sites characterized in this study.

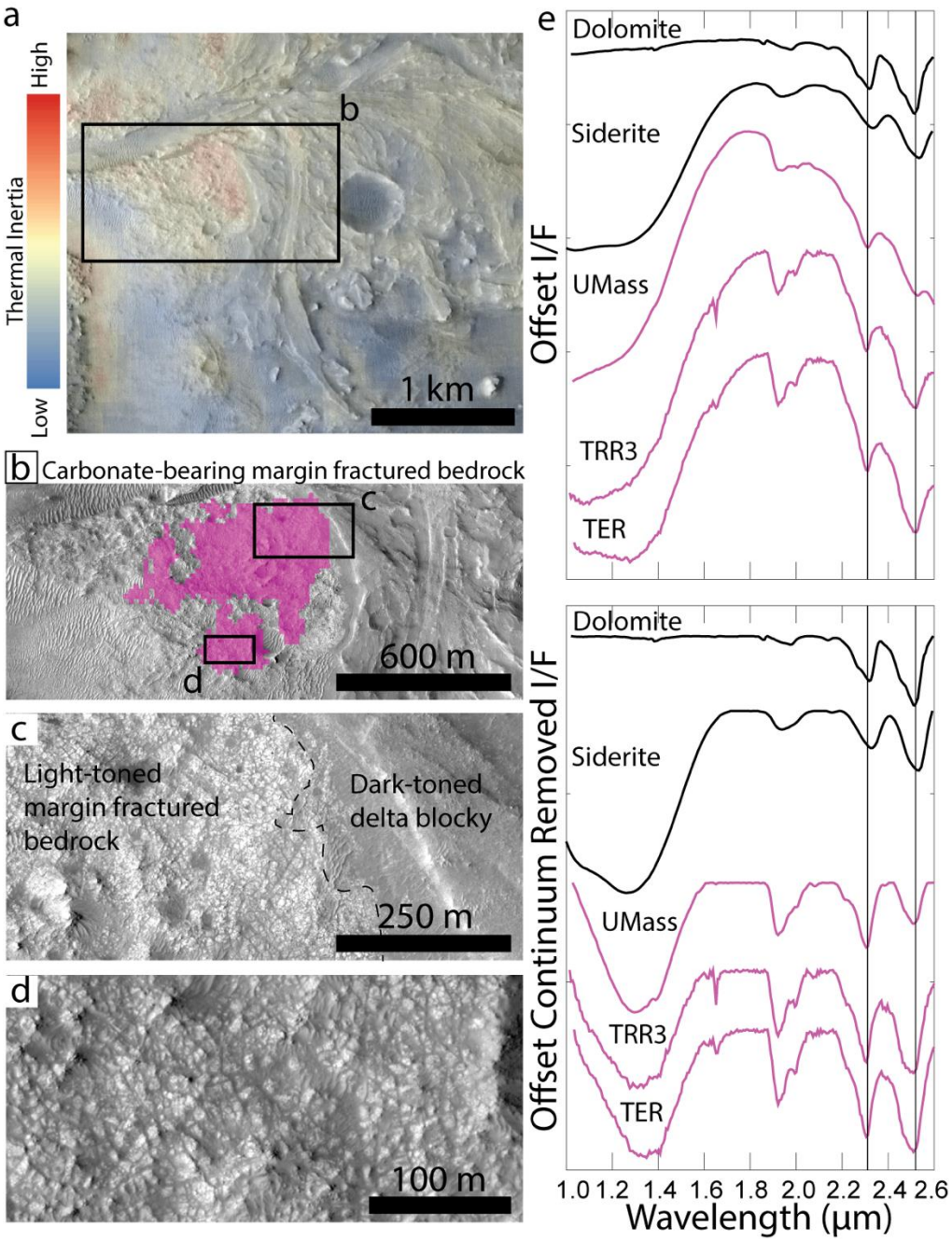

Figure 4 | Carbonate and phyllosilicate-bearing bedrock in the margin fractured unit. (a) THEMIS qualitative thermal inertia map of region of interest. (b) CRISM pixels (pink) for spectra shown in (e). These CRISM pixels cover light-toned fractured bedrock with notably high thermal inertia. (c) Enlarged view of light-toned margin-fractured unit bedrock and contact with dark-toned delta blocky unit material. (d) Enlarged view of light-toned margin fractured unit bedrock. (e) UMass, TRR3, And TER CRISM spectra of pink pixels shown in (b). The 2.3 and 2.5 μm features are consistent with the presence of carbonate-bearing rock. The ratio of the 2.3/2.5 μm absorptions is consistent with presence of some phyllosilicate-bearing material. The absorption centered at 1.0 μm may be due to presence of olivine or presence of siderite.

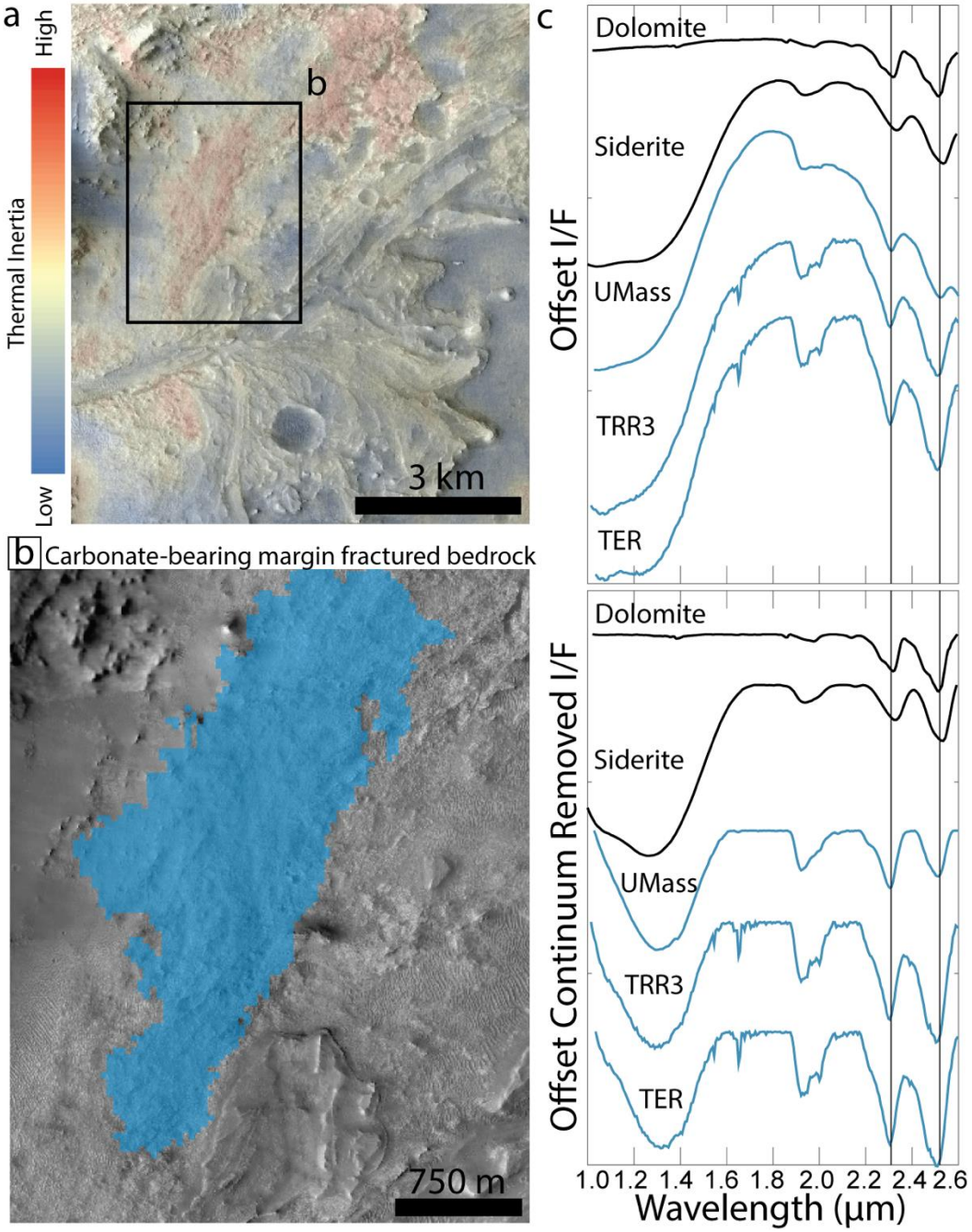

Figure 5 | Carbonate and phyllosilicate-bearing bedrock in the margin fractured unit. (a) THEMIS qualitative thermal inertia map of region of interest. (b) CRISM pixels (blue) for spectra shown in (c). These CRISM pixels cover light-toned fractured bedrock with notably high thermal inertia. (c) UMass, TRR3, And TER CRISM spectra of blue pixels shown in (b). The spectral and geologic interpretation is the same as is described in Figure 4.

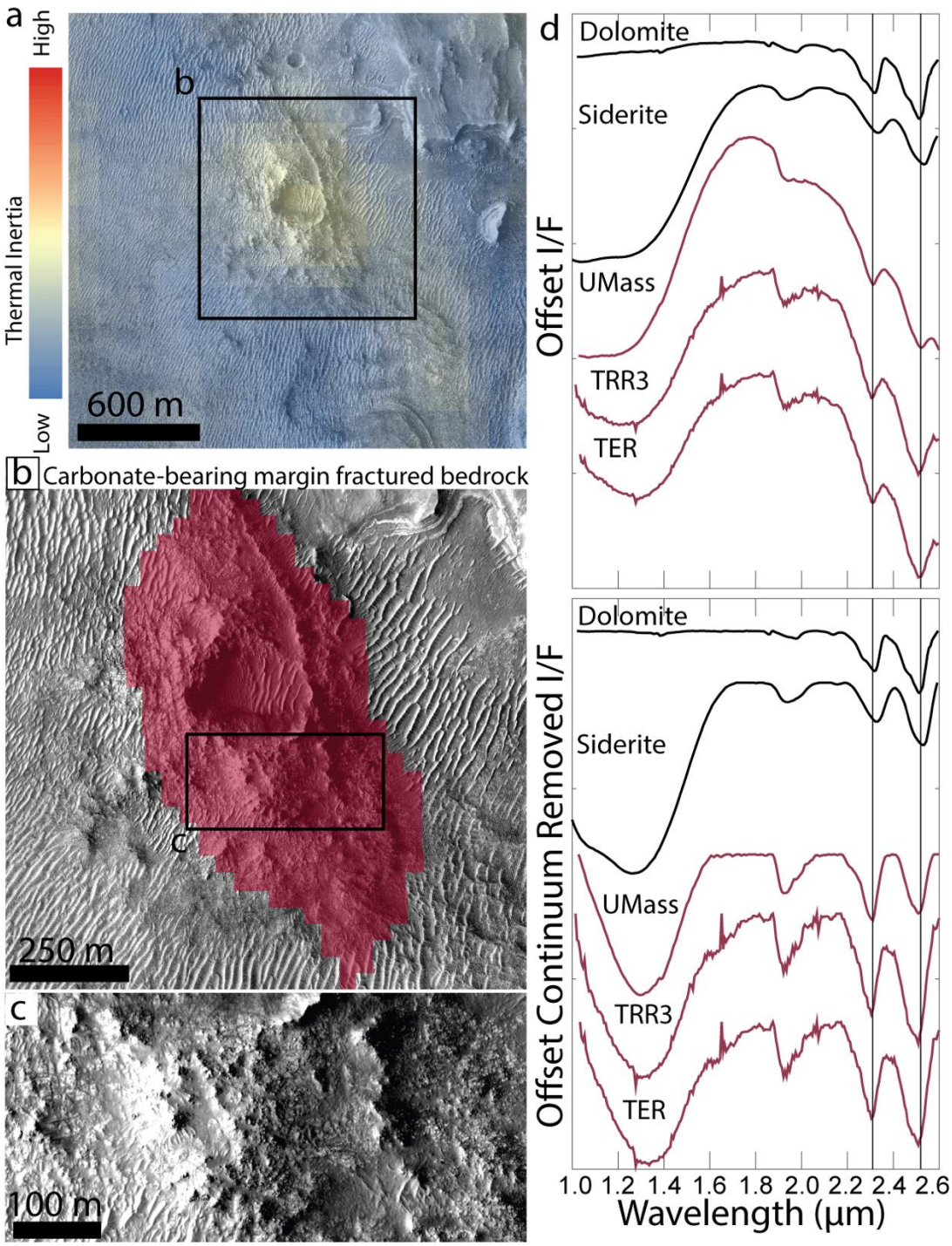

Figure 6 | Carbonate and phyllosilicate-bearing bedrock in the margin fractured unit. (a) THEMIS qualitative thermal inertia map of region of interest. (b) CRISM pixels (dark red) for spectra shown in (e). These CRISM pixels cover light-toned fractured bedrock with notably high thermal inertia. (c) Enlarged view of light-toned margin-fractured unit bedrock and contact with dark-toned delta blocky unit material. (d) UMass, TRR3, And TER CRISM spectra of dark red pixels shown in (b). The spectral and geologic interpretation is the same as is described in Figure 4.

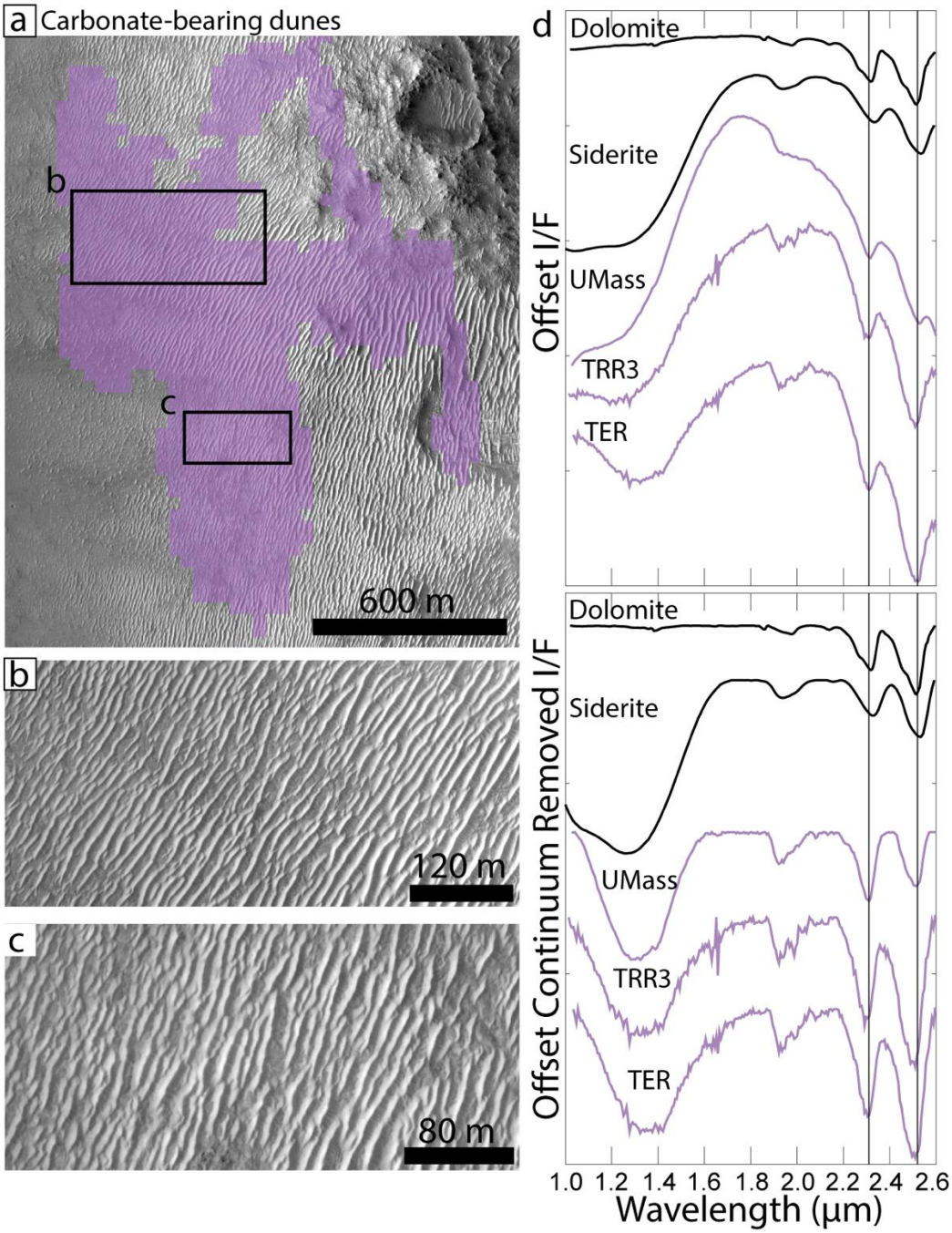

Figure 7 | Carbonate and phyllosilicate-bearing aeolian bedforms proximal to margin fractured unit. (a) CRISM pixels (purple) for the spectra shown in (d). These pixels cover aeolian bedforms immediately west of the margin fractured bedrock shown in Figure 6. (b-c) Enlarged views of carbonate and phyllosilicate-bearing aeolian bedforms. (d) UMass, TRR3, And TER CRISM spectra from purple pixels shown in (a). The spectral interpretation is the same as described in Figure 4. This aeolian material is therefore interpreted to derive from the proximal margin fractured unit bedrock.

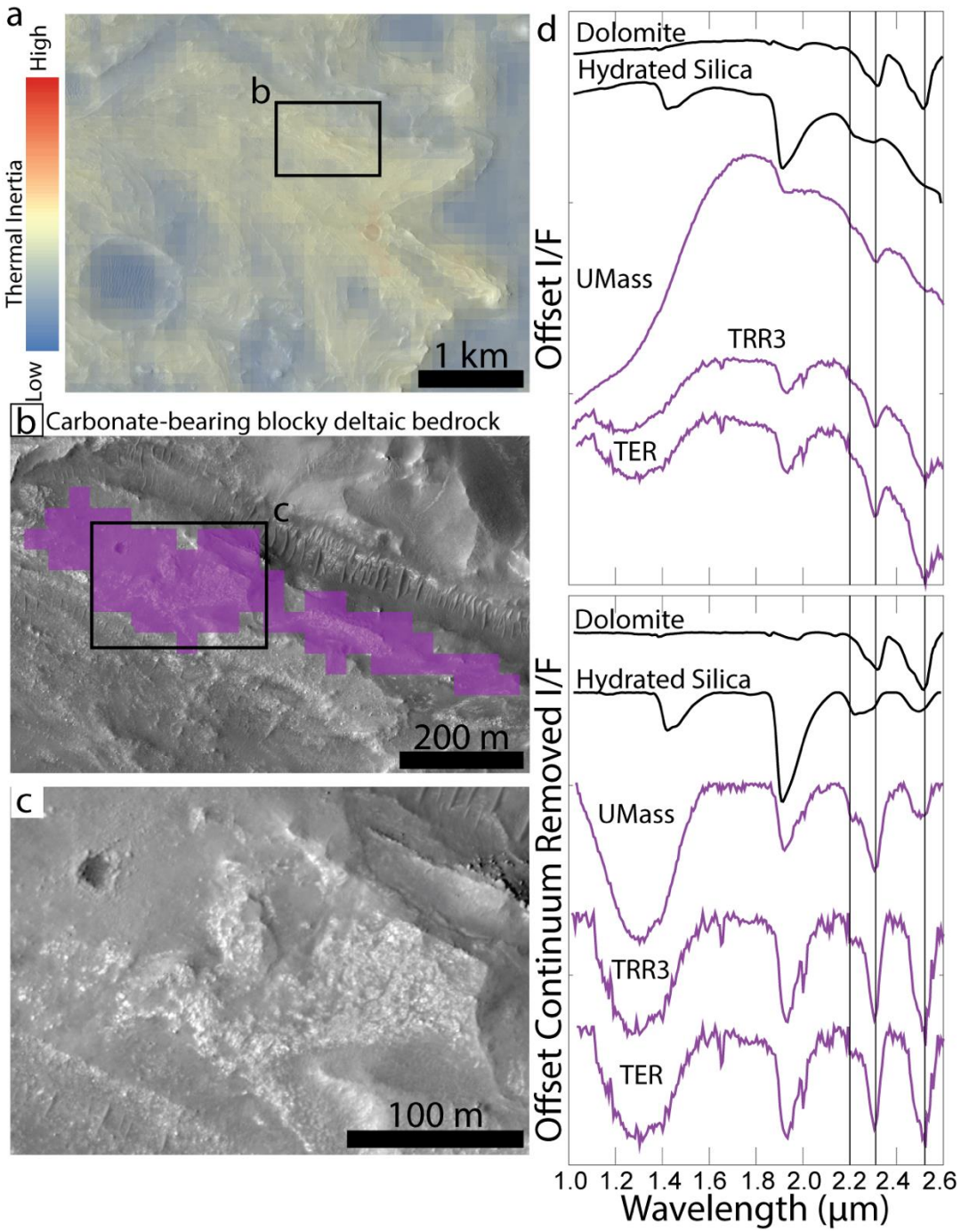

Figure 8 | Carbonate and phyllosilicate-bearing rock in the western Jezero delta blocky unit. (a) THEMIS thermal inertia map of region of interest. (b) CRISM pixels (purple) for spectra shown in (d), which cover light and dark-toned bedrock in the delta blocky unit. (c) Enlarged view of light and dark-toned bedrock. (d) UMass, TRR3, And TER CRISM spectra from purple pixels shown in (b). The 2.3 and 2.5 μm absorptions are consistent with the presence of carbonate-bearing rock. The 2.3/2.5 μm absorptions are consistent with the presence of phyllosilicate-bearing material. The small absorption at 2.2 μm is consistent with the presence

of either hydrated silica and/or Al-phyllosilicate. Overall, this composition resembles the crater floor fractured 2 unit, but with a stronger 2.3 µm feature, consistence with stronger spectral presence of phyllosilicates.

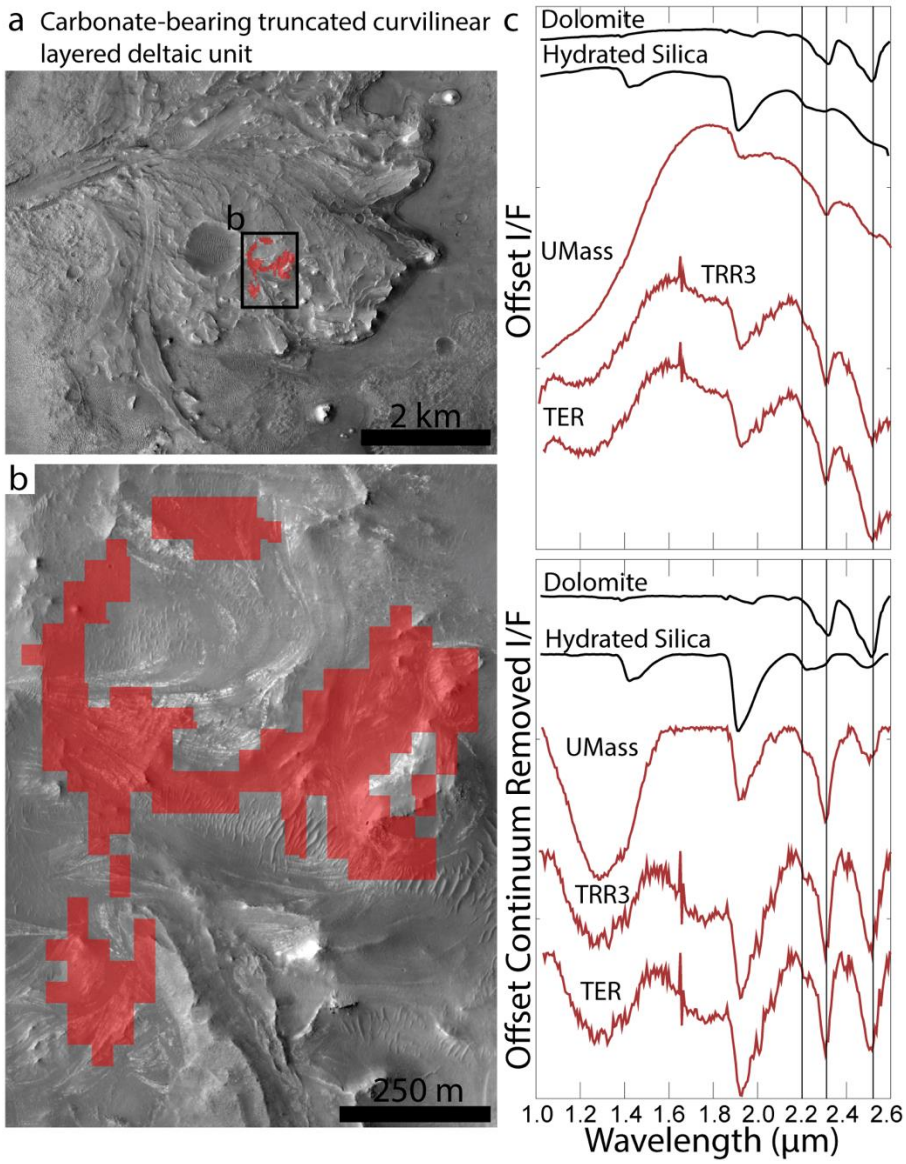

Figure 9 | Carbonate and phyllosilicate-bearing rock in the western Jezero delta truncated curvilinear layered unit. (a) Regional view of reported compositional detections from CRISM pixels shown in red. (b) CRISM pixels (red) for spectra shown in (c), which cover possible point bar strata in the delta truncated curvilinear layered unit (Goudge et al. 2018). (c) UMass, TRR3, And TER CRISM spectra from red pixels shown in (a & b). The spectral interpretation is the same as described in Figure 8, but is present on a different deltaic unit.

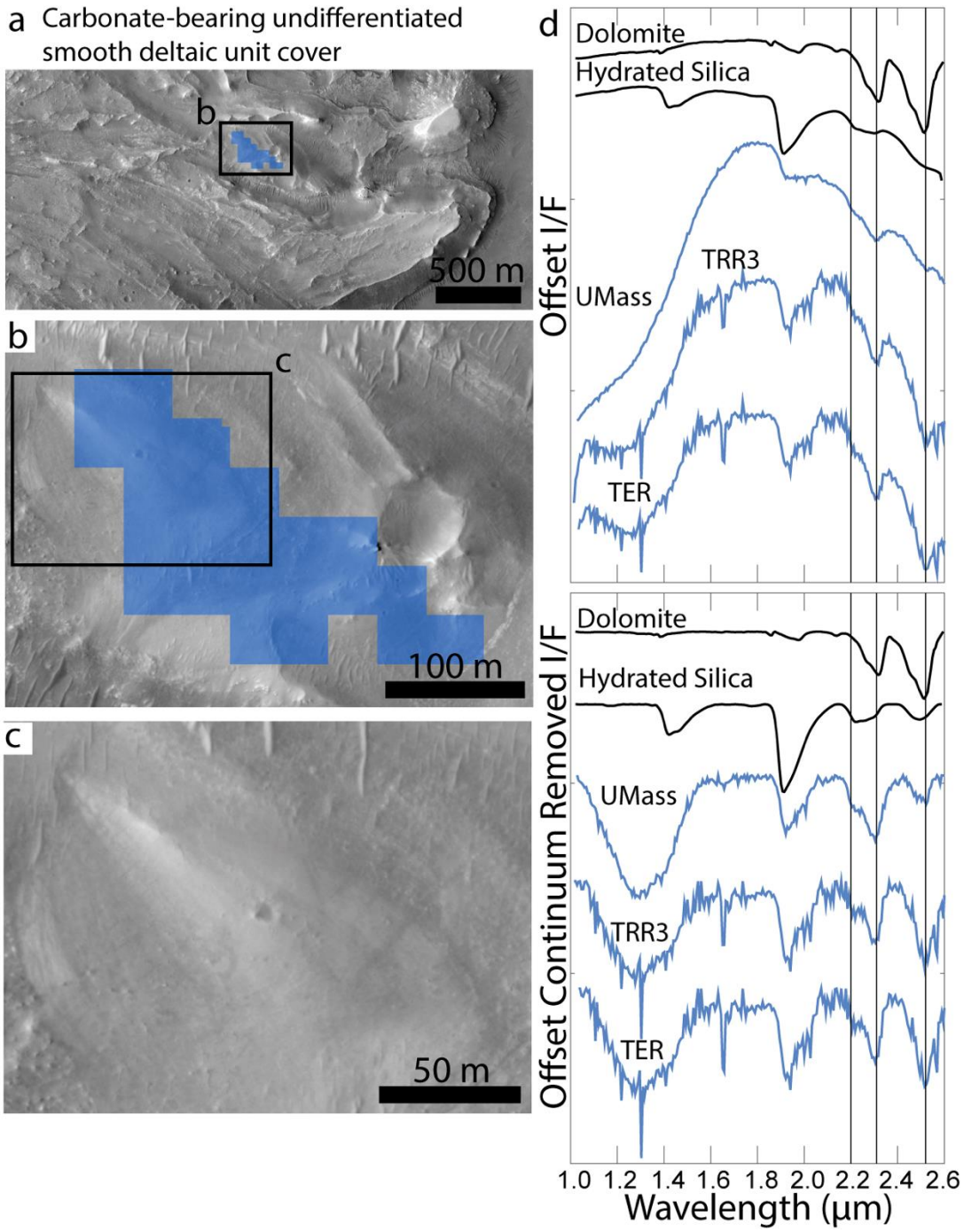

Figure 10 | Carbonate and phyllosilicate-bearing rock in the western Jezero delta undifferentiated smooth unit. (a) Regional view of reported compositional detections from CRISM pixels shown in blue. (b) CRISM pixels (blue) for spectra shown in (c), which cover primarily dark-toned bedrock in the delta undifferentiated smooth unit. (c) UMass, TRR3, And TER CRISM spectra from blue pixels shown in (a & b). The spectral interpretation is the same as described in Figure 8, but is present on a different deltaic unit.

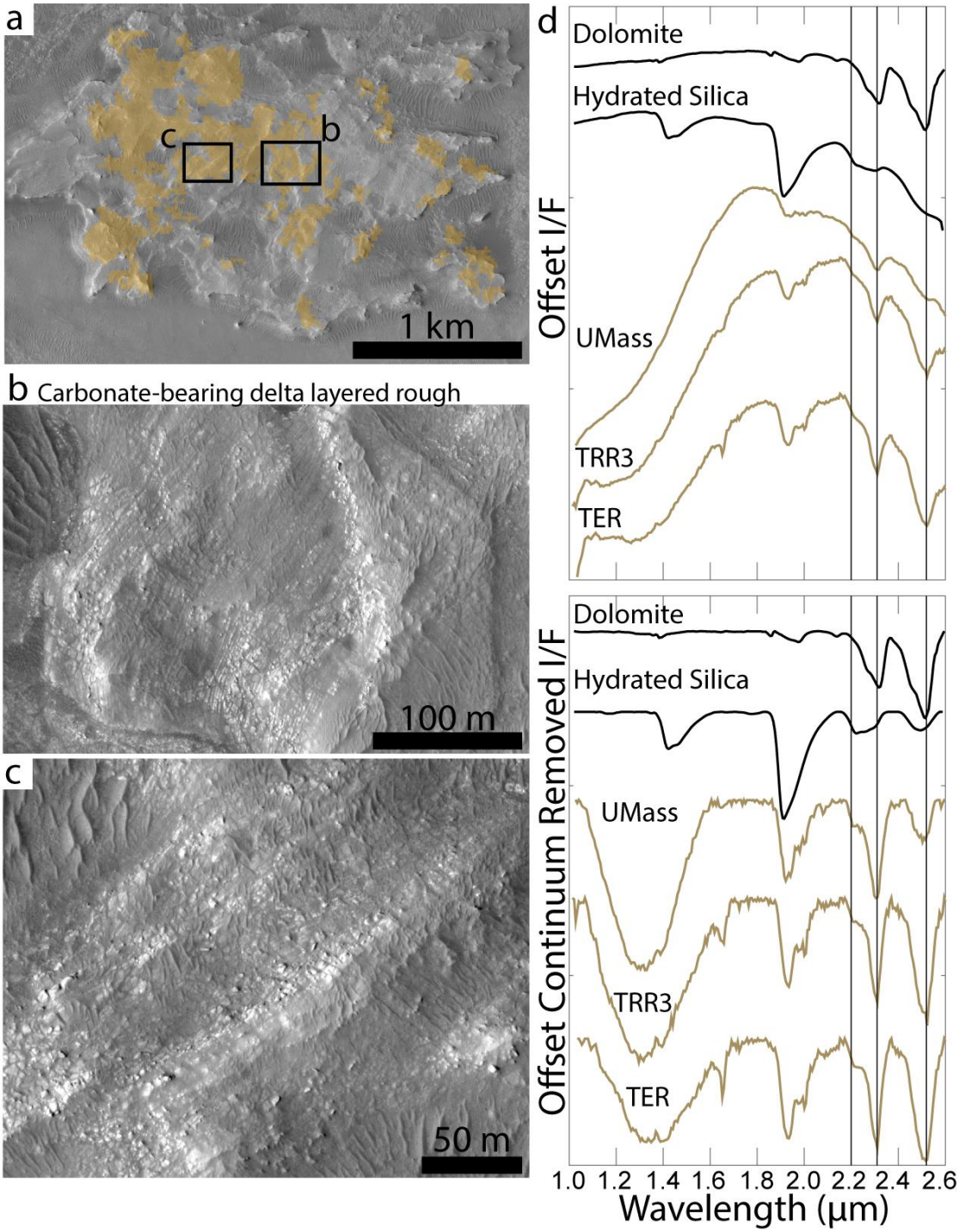

Figure 11 | Carbonate and phyllosilicate-bearing rock in the northern Jezero delta layered rough unit. (a) Regional view of reported compositional detections from CRISM pixels shown in orange, which cover the northern delta. (b & c) Enlarged views of layered light-toned bedrock in northern delta. (d) UMass, TRR3, And TER CRISM spectra from orange pixels shown in (a & b). The spectral interpretation is the same as described in Figure 8, but is present on a different deltaic unit.

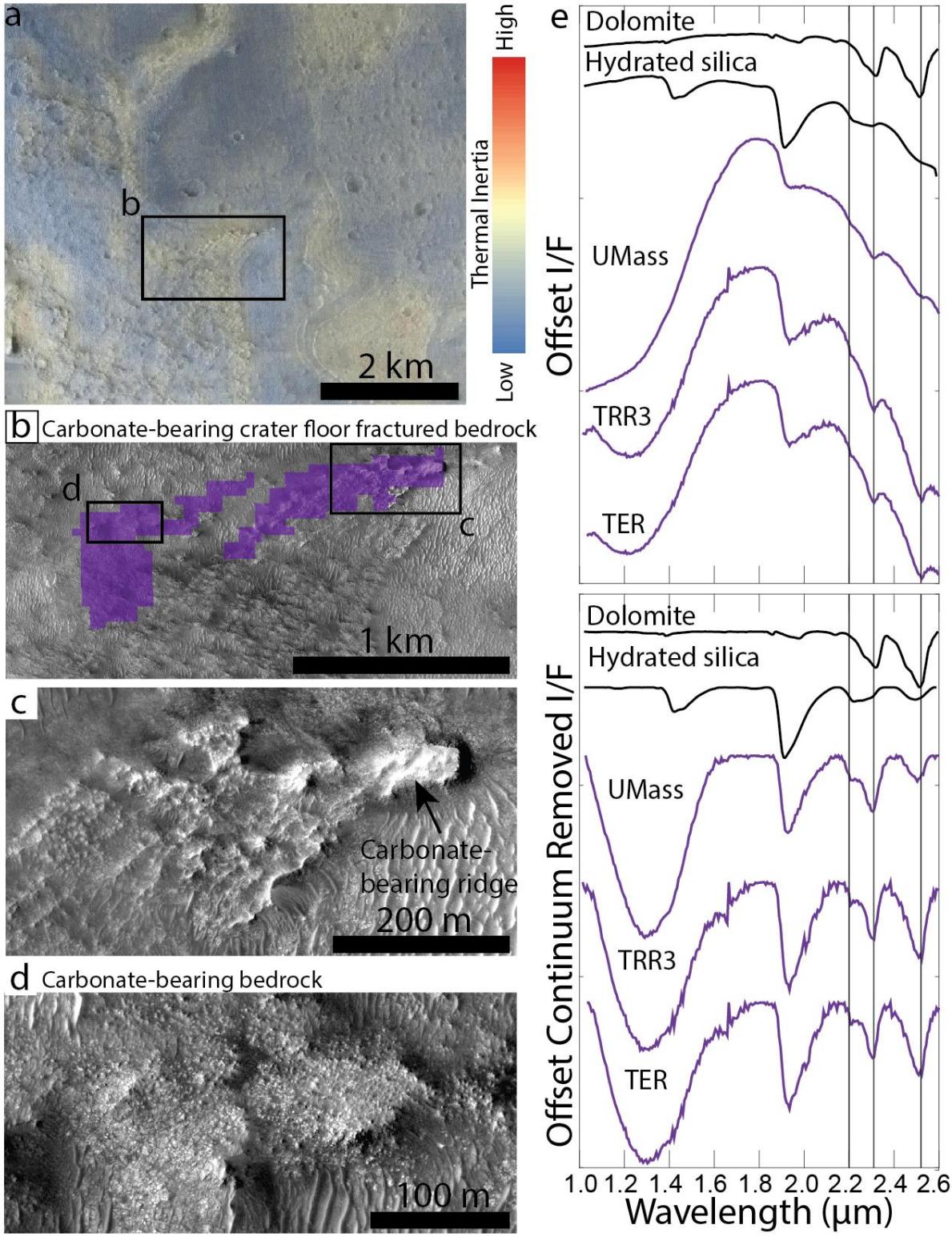

Figure 12 | Carbonate, silica, and olivine-bearing bedrock. (a) THEMIS qualitative thermal inertia map from Fergason et al. (2006), coregistered to CTX and HiRISE mosaics by Dickson et al. (2018). Warmer colors correspond to more consolidated (warmer colors) and less

consolidated (cooler colors) materials. (b) CRISM pixels (purple) on HiRISE image from which the spectra shown in (e) are derived. The CRISM pixels were selected based on THEMIS thermal inertia and HiRISE data to cover bedrock in the crater floor fractured 2 unit. (c) Enlarged view of a ridge in the crater floor fractured 2 unit (Stack et al. 2020). (d) Enlarged view of rubbly bedrock in the crater floor fractured 2 unit. (e) Spectra from UMass, TRR3, And TER processed CRISM data (purple) extracted from the pixels shown in (b) and compared to laboratory spectra of dolomite (RELAB ID C1CY07) and hydrated silica. The spectra are consistent with the presence of carbonate-bearing rock based on the presence of 2.3 and 2.5 µm features. The ratio of 2.3/2.5 µm band depth and narrow shape of the 2.3 µm feature are also consistent with the presence of phyllosilicate-bearing rock. The absorption at 2.2 µm, which combines with the 2.3 µm absorption to create a broad band, is consistent with the presence of hydrated silica and/or Al-phyllosilicate. The absorption centered at 1.0 µm is consistent with the presence of olivine-bearing rock, which is widespread throughout this unit. Hydrated silica is a product of carbonation of olivine (Falk & Kelemen, 2015). The thermal inertia, visible texture and topography, geologic context, and VNIR spectra of this outcrop are consistent with carbonate, hydrated silica, and olivine-bearing bedrock.

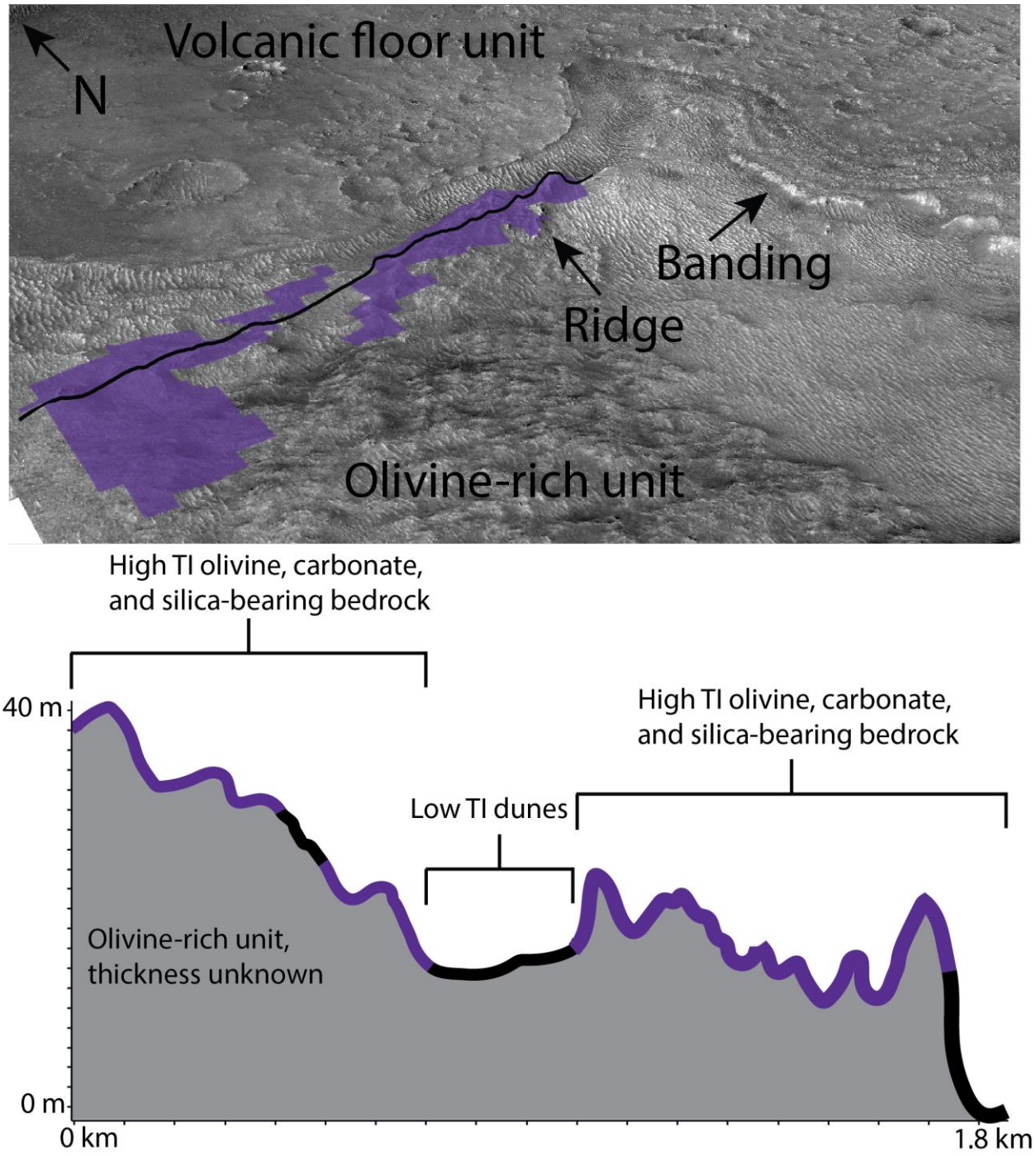

Figure 13 | Olivine, carbonate, and silica-bearing ridge in crater floor fractured 2 unit. (top) HiRISE mosaic overlain on HiRISE digital elevation model (DEM). The ridge occurs near the contact between the crater floor fractured 2 and undifferentiated smooth floor units as described by Stack et al. (2020). Banding can be seen at this contact towards the east. (bottom) The spectra shown in Figure 12 were extracted from topographic highs with moderate thermal inertia, which is consistent with the hypothesis that this material is olivine, carbonate, phyllosilicate, and silica-bearing bedrock.

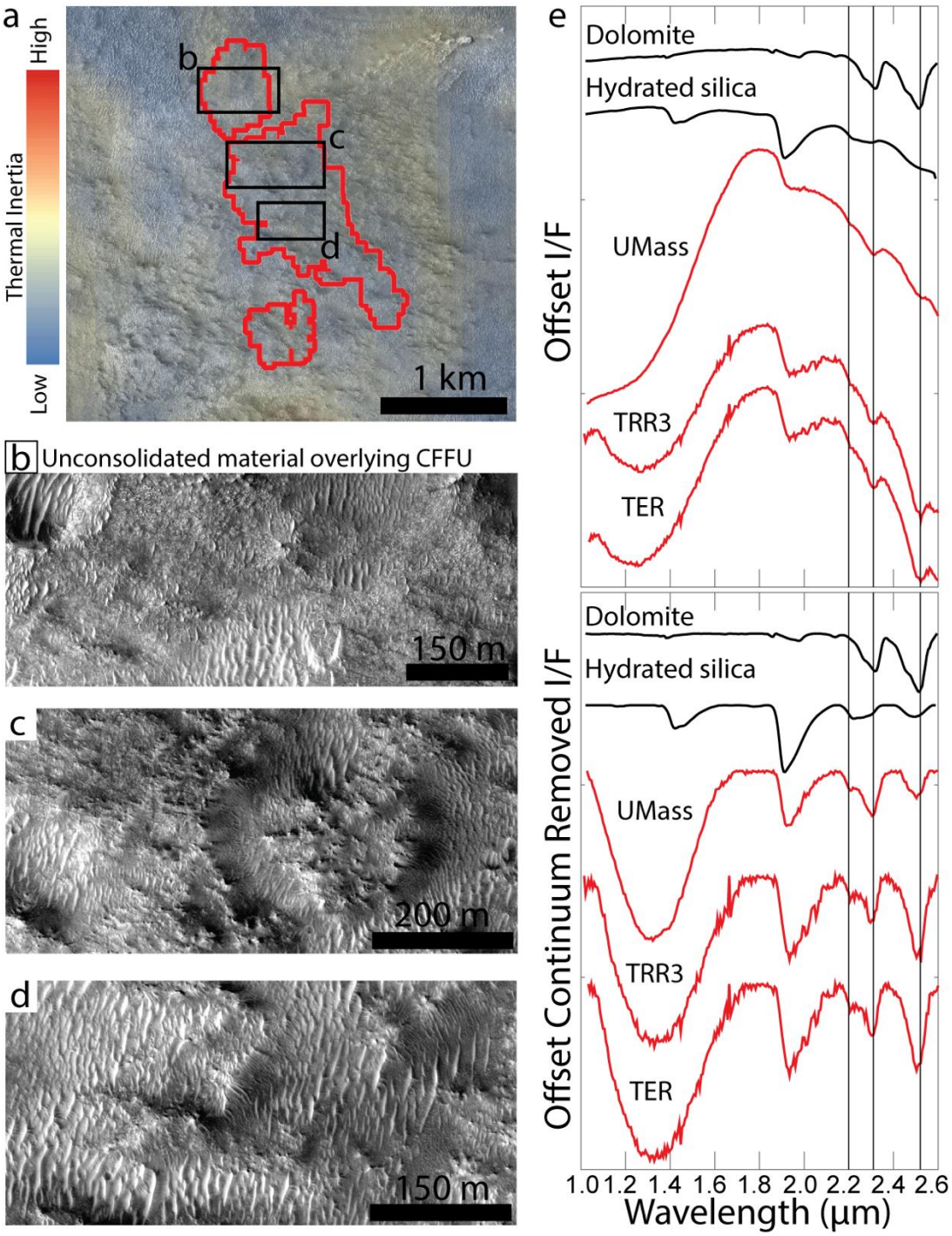

Figure 14 | Olivine, carbonate, phyllosilicate, and silica-bearing unconsolidated material in crater floor fractured 2 unit. (a) THEMIS qualitative thermal inertia map. The CRISM pixels for the spectra in (e), which are within the red outlines, cover dunes and unconsolidated dark-toned material that has low thermal inertia. (b) Enlarged view of dunes and dark-toned unconsolidated dark-toned material overlying bedrock, which in some locations protrudes through this material. (c) Enlarged view of dunes and knobby bedrock that is covered by dark-toned unconsolidated material. (d) Enlarged view of dunes and unconsolidated dark-toned

material overlying bedrock. (e) UMass, TRR3, and TER processed CRISM spectra from pixels shown in (b) compared to library spectra of dolomite and hydrated silica. The spectral features are the same as those described for bedrock in Figure 12, implying that the dunes and unconsolidated dark-toned material are locally sourced and have the same composition as the proximal and underlying crater floor fractured 2 unit bedrock.

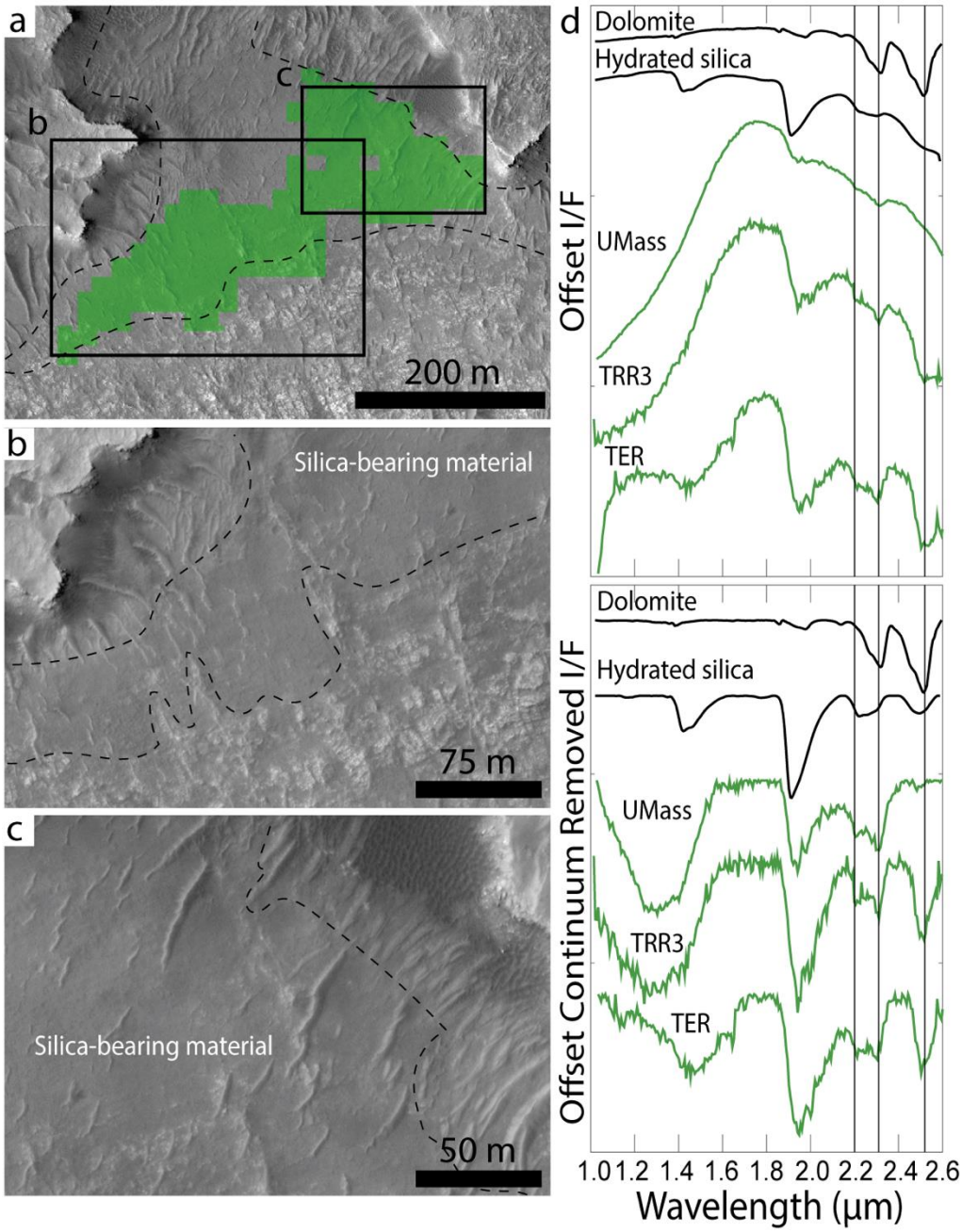

Figure 15 | Smooth dark-toned silica-bearing material overlying crater floor fractured unit. (a) CRISM pixels (green) for the spectra shown in (d). These pixels cover the smooth dark-toned

material reported to be silica-bearing by Tarnas et al. (2019). (b) Enlarged view of smooth dark-toned silica-bearing material overlying the crater floor fractured unit. (c) Another enlarged view of smooth dark-toned silica-bearing material overlying the crater floor fractured unit. (d) UMass, TRR3, And TER CRISM spectra from green pixels shown in (a). These spectra are consistent with hydrated silica and the Jezero crater hydrated silica detections reported in this material in different locations by Tarnas et al. (2019).

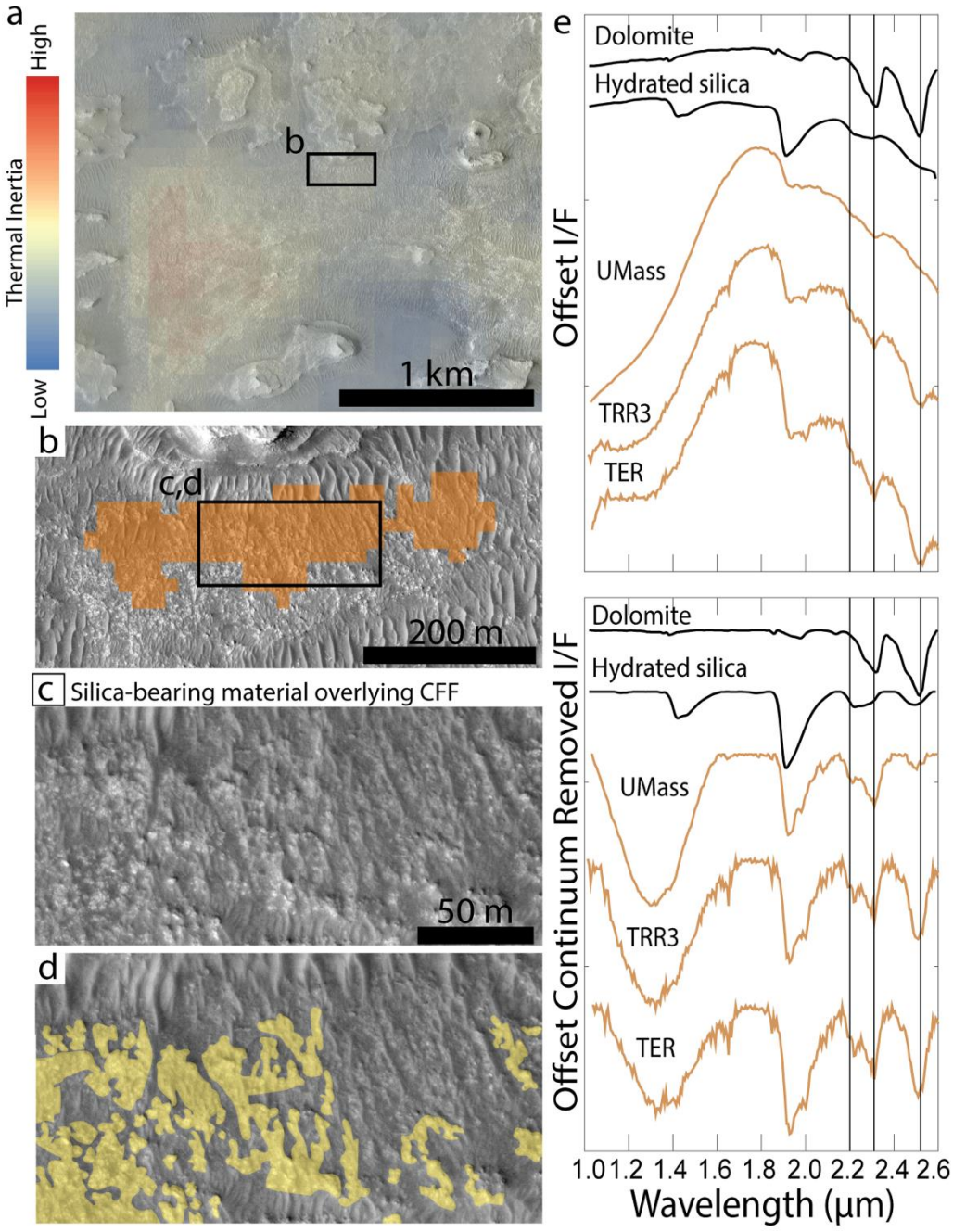

Figure 16 | Silica-bearing material overlying crater floor fractured unit. (a) THEMIS thermal inertia of target area. The area of interest (within the black outline) has moderate thermal inertia. (b) CRISM pixels for the spectra in (e) shown in orange. (c) Enlarged view of dark-toned

unconsolidated material overlying crater floor fractured unit bedrock. (d) Same image as (c), but with crater floor fractured unit bedrock mapped in yellow. Most of the area covered by the CRISM pixels shown in (a) is comprised of dark-toned unconsolidated material. (e) UMass, TRR3, And TER CRISM spectra of pixels shown in (a). The broad 2.2 µm feature is consistent with the presence of hydrated silica, which was also reported in smooth dark-toned material in Jezero crater by Tarnas et al. (2019). The additional 2.3 µm absorption that merges with the 2.2 µm features is consistent with the presence of phyllosilicate-bearing material. The geologic context, visible properties, and spectra of this outcrop are consistent with hydrated silica-bearing dark-toned unconsolidated material overlying phyllosilicate-bearing crater floor fractured unit bedrock.

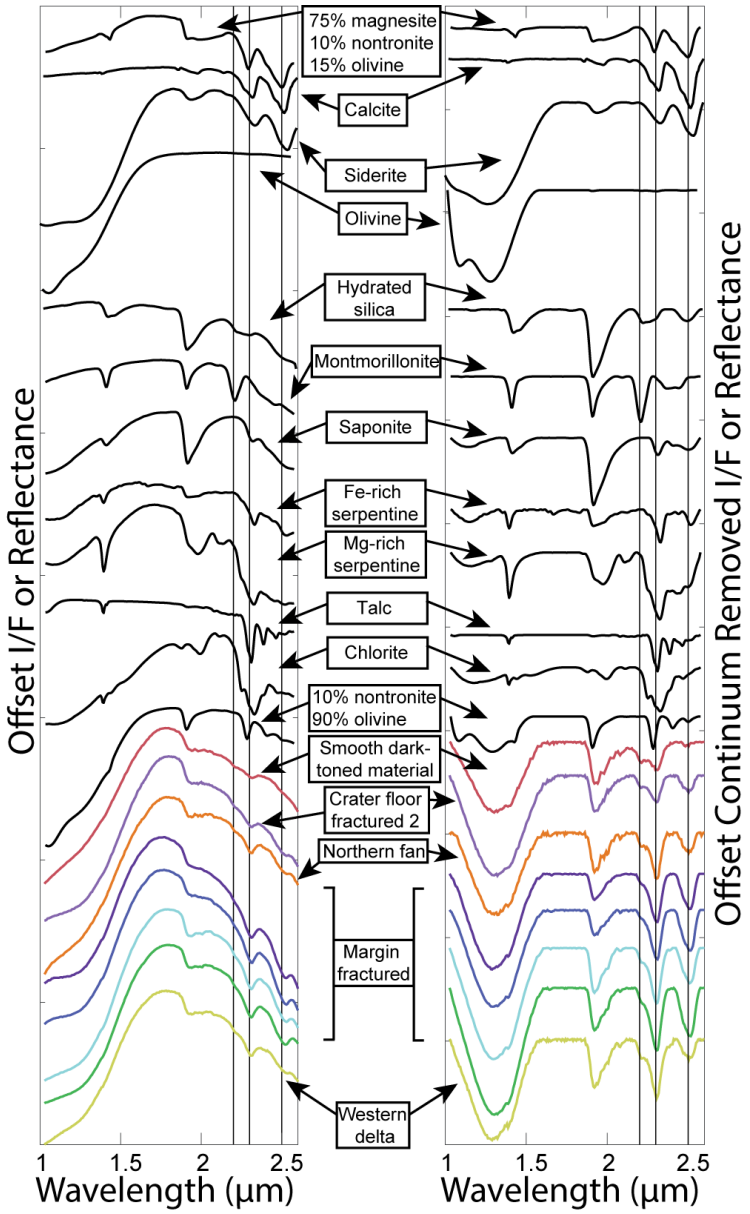

Figure 17 | Spectra of carbonate-bearing units in Jezero crater compared to library spectra. The colors of CRISM spectra correspond to those in Figure 1, while the library spectra are

shown in black. The CRISM spectra are likely mixtures of one or more of the minerals with displayed library spectra. Interpretations for mineral assemblages consistent with each CRISM spectrum are provided in the main text. The library spectra are RELAB IDs CABE01, BNR1BE052, BIR1BE030, C1CY07, CASA59, BIR1SR052A, C1RK67, 397S013, BKR1SR068, and 397S214.

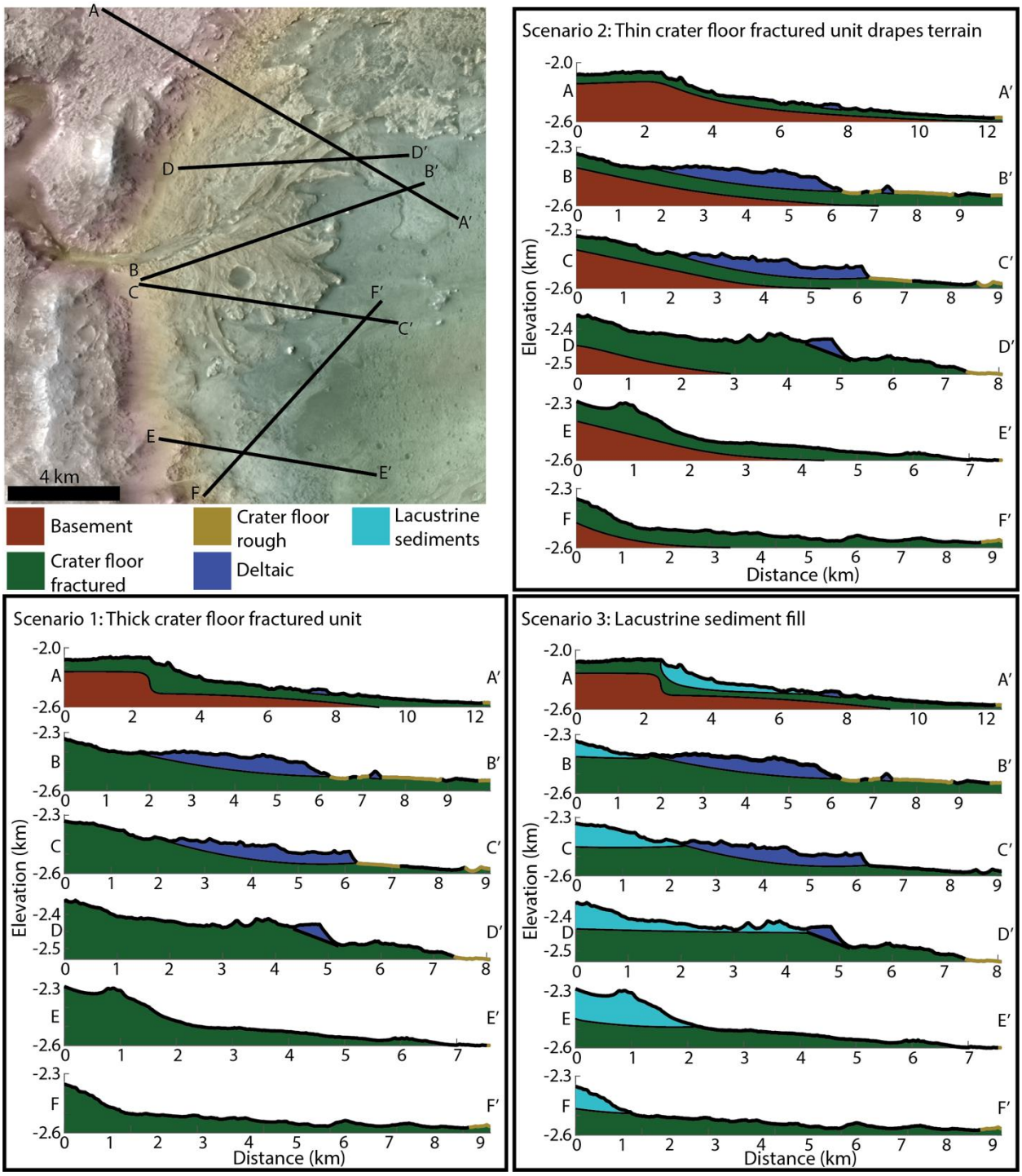

Figure 18 | Cross sections of topography in western Jezero crater, with different interpretations annotated. All illustrated hypothetical contacts are unconformable. Scenarios 1-3 are detailed in Section 5.2.

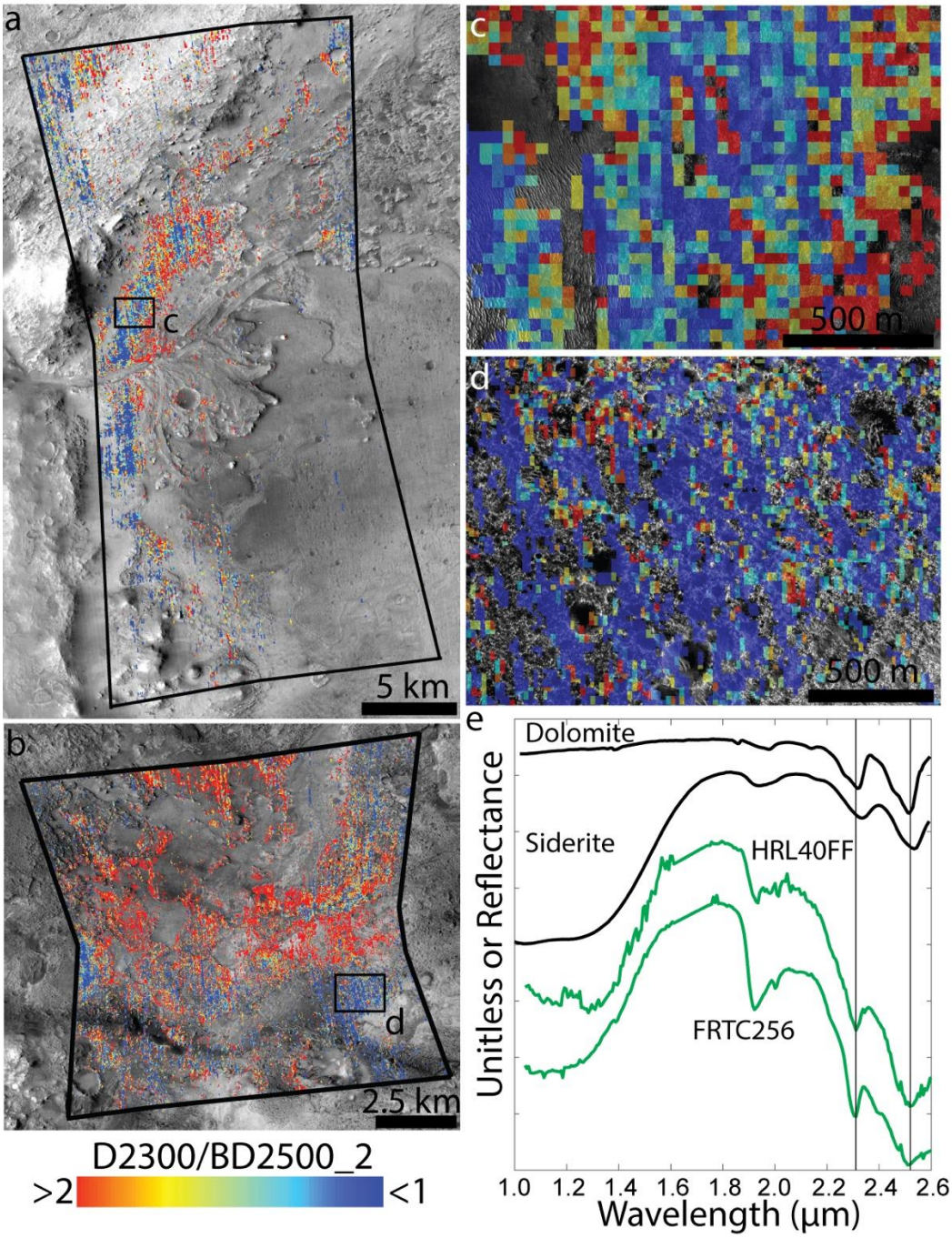

Figure 19 | Comparison of carbonate spectral properties in Jezero crater and elsewhere in the Nili Fossae region. (a) Ratio of the 2.3 and 2.5 μm absorptions (D2300/BD2500_2) in CRISM pixels of image HRL000040FF with BD2500_2 ≥ 0.005. As noted by Horgan et al., (2020a), the most widespread collection of pixels with the lowest 2.3/2.5 μm absorption band depth ratio is associated with the margin fractured unit. However, the 2.3/2.5 μm band depth ratio is also low

in the ROB unit immediately outside of Jezero crater. The black outline shows the extent of CRISM image HRL000040FF. (b) Ratio of the 2.3 and 2.5 μm absorptions (D2300/BD2500_2) in CRISM pixels of image FRT0000C256 with BD2500_2 ≥ 0.005. There are large outcrops of carbonate with similar 2.3/2.5 μm band depth ratios as the margin fractured unit. All pixels shown here are associated with the ROB unit. Figure S10 shows an expanded view of 2.3/2.5 μm band depth ratios in this region, mosaicking multiple CRISM images. (c) Enlarged view of box shown in (a). (d) Enlarged view of box shown in (b). (e) Spectral endmembers of pixels shown in (a) and (b) calculated via HySime (green, Section 3.1) compared to library spectra of carbonates (black). Both endmembers are consistent with a mixture of carbonate, phyllosilicate(s), and olivine.

Observations	Fluvio-acustrine	Not fluvio-lacustrine
Strong VNIR carbonate absorptions mostly surrounded by maximum lake level contour in Jezero	√	×
Gradational relationship, no contact, with regional olivine-bearing unit that drapes into Jezero crater	×	√
Strongest margin fractured VNIR carbonate absorptions are in the highest thermal inertia bedrock	~	√
Equivalent 2.3/2.5 µm band depth ratios inside Jezero crater and elsewhere in Nili Fossae	~	~
Thickness of margin fractured unit relative to regional olivine-bearing unit	√	~
Presence of primary minerals in margin fractured unit	√	√
Gradational relationship, no visible contact, with carbonate-bearing crater floor fractured 2 unit	~	~
Distribution of spectral features with respect to inlet channel	~	~

√ Consistent

× Inconsistent

~ Indeterminate

Table 1 | Orbital observations of Jezero margin fractured unit and interpreted favorability for either a fluviolacustrine or not fluviolacustrine (groundwater) origin for carbonates there. The evidence from orbit is inconclusive regarding the processes that formed carbonates in Jezero crater. Either hypothesis may be correct, or an intermediate hypothesis –where both carbonate formation mechanisms occurred during distinct time periods—may be correct. Observations by the Perseverance Mars 2020 rover will constrain carbonate formation processes in the Jezero crater margin fractured unit.

References

Agashev, A.M., Pokhilenko, N.P., Takazawa, E., McDonald, J.A., Vavilov, M.A., Watanabe, T., Sobolev, N.V., 2008. Primary melting sequence of a deep (>250 km) lithospheric mantle as recorded in the geochemistry of kimberlite–carbonatite assemblages, Snap Lake dyke system, Canada. Chemical Geology 255, 317–328. https://doi.org/10.1016/j.chemgeo.2008.07.003

Amador, E.S., Bandfield, J.L., Brazelton, W.J., Kelley, D., 2017. The Lost City Hydrothermal Field: A Spectroscopic and Astrobiological Analogue for Nili Fossae, Mars. Astrobiology 17, 1138–1160. https://doi.org/10.1089/ast.2016.1606

Arvidson, R.E., Christian, J.C., 2020. Use of CRISM, CTX, and HiRISE Data to Map Bedrock Sources and Wind-Blown Ripple Field Mineralogy On and Near the Jezero Crater Delta 51, 1194.

Arvidson, R.E., Ruff, S.W., Morris, R.V., Ming, D.W., Crumpler, L.S., Yen, A.S., Squyres, S.W., Sullivan, R.J., Bell, J.F., Cabrol, N.A., Clark, B.C., Farrand, W.H., Gellert, R., Greenberger, R., Grant, J.A., Guinness, E.A., Herkenhoff, K.E., Hurowitz, J.A., Johnson, J.R., Klingelhöfer, G., Lewis, K.W., Li, R., McCoy, T.J., Moersch, J., McSween, H.Y., Murchie, S.L., Schmidt, M., Schröder, C., Wang, A., Wiseman, S., Madsen, M.B., Goetz, W., McLennan, S.M., 2008. Spirit Mars Rover Mission to the Columbia Hills, Gusev Crater: Mission overview and selected results from the Cumberland Ridge to Home Plate. Journal of Geophysical Research: Planets 113. https://doi.org/10.1029/2008JE003183

Arvidson, R.E., Squyres, S.W., Anderson, R.C., Bell, J.F., Blaney, D., Brückner, J., Cabrol, N.A., Calvin, W.M., Carr, M.H., Christensen, P.R., Clark, B.C., Crumpler, L., Marais, D.J.D., Souza, P.A. de, d'Uston, C., Economou, T., Farmer, J., Farrand, W.H., Folkner, W., Golombek, M., Gorevan, S., Grant, J.A., Greeley, R., Grotzinger, J., Guinness, E., Hahn, B.C., Haskin, L., Herkenhoff, K.E., Hurowitz, J.A., Hviid, S., Johnson, J.R., Klingelhöfer, G., Knoll, A.H., Landis, G., Leff, C., Lemmon, M., Li, R., Madsen, M.B., Malin, M.C., McLennan, S.M., McSween, H.Y., Ming, D.W., Moersch, J., Morris, R.V., Parker, T., Rice, J.W., Richter, L., Rieder, R., Rodionov, D.S., Schröder, C., Sims, M., Smith, M., Smith, P., Soderblom, L.A., Sullivan, R., Thompson, S.D., Tosca, N.J., Wang, A., Wänke, H., Ward, J., Wdowiak, T., Wolff, M., Yen, A., 2006. Overview of the Spirit Mars Exploration Rover Mission to Gusev Crater: Landing site to Backstay Rock in the Columbia Hills. Journal of Geophysical Research: Planets 111. https://doi.org/10.1029/2005JE002499

Bandfield, J.L., Christensen, P.R., Smith, M.D., 2000. Spectral data set factor analysis and end-member recovery: Application to analysis of Martian atmospheric particulates. Journal of Geophysical Research: Planets 105, 9573–9587. https://doi.org/10.1029/1999JE001094

Bandfield, J.L., Edgett, K.S., Christensen, P.R., 2002. Spectroscopic study of the Moses Lake dune field, Washington: Determination of compositional distributions and source lithologies. Journal of Geophysical Research: Planets 107, 2-1-2–15. https://doi.org/10.1029/2000JE001469

Bandfield, J.L., Glotch, T.D., Christensen, P.R., 2003. Spectroscopic Identification of Carbonate Minerals in the Martian Dust. Science 301, 1084–1087. https://doi.org/10.1126/science.1088054

Beyer, R.A., Alexandrov, O., McMichael, S., 2018. The Ames Stereo Pipeline: NASA's Open Source Software for Deriving and Processing Terrain Data. Earth and Space Science 5, 537–548. https://doi.org/10.1029/2018EA000409

Bibring, J.-P., Soufflot, A., Berthé, M., Langevin, Y., Gondet, B., Drossart, P., Bouyé, M., Combes, M., Puget, P., Semery, A., 2004. OMEGA: Observatoire pour la Minéralogie, l'Eau, les Glaces et l'Activité, in: Mars Express: The Scientific Payload. pp. 37–49.

Bioucas-Dias, J.M., Nascimento, J.M.P., 2008. Hyperspectral Subspace Identification. IEEE Transactions on Geoscience and Remote Sensing 46, 2435–2445. https://doi.org/10.1109/TGRS.2008.918089

Bishop, J.L., Perry, K.A., Dyar, M.D., Bristow, T.F., Blake, D.F., Brown, A.J., Peel, S.E., 2013. Coordinated spectral and XRD analyses of magnesite-nontronite-forsterite mixtures and implications for carbonates on Mars. Journal of Geophysical Research: Planets 118, 635–650. https://doi.org/10.1002/jgre.20066

Borg, L.E., Connelly, J.N., Nyquist, L.E., Shih, C.-Y., Wiesmann, H., Reese, Y., 1999. The Age of the Carbonates in Martian Meteorite ALH84001. Science 286, 90–94. https://doi.org/10.1126/science.286.5437.90

Boynton, W.V., Ming, D.W., Kounaves, S.P., Young, S.M.M., Arvidson, R.E., Hecht, M.H., Hoffman, J., Niles, P.B., Hamara, D.K., Quinn, R.C., Smith, P.H., Sutter, B., Catling, D.C., Morris, R.V., 2009. Evidence for Calcium Carbonate at the Mars Phoenix Landing Site. Science 325, 61–64. https://doi.org/10.1126/science.1172768

Bramble, M.S., Mustard, J.F., Salvatore, M.R., 2017. The geological history of Northeast Syrtis Major, Mars. Icarus 293, 66–93. https://doi.org/10.1016/j.icarus.2017.03.030

Bridges, J.C., Grady, M.M., 2000. Evaporite mineral assemblages in the nakhlite (martian) meteorites. Earth and Planetary Science Letters 176, 267–279. https://doi.org/10.1016/S0012-821X(00)00019-4

Bristow, T.F., Milliken, R.E., 2011. TERRESTRIAL PERSPECTIVE ON AUTHIGENIC CLAY MINERAL PRODUCTION IN ANCIENT MARTIAN LAKES. Clays and Clay Minerals 59, 339–358. https://doi.org/10.1346/CCMN.2011.0590401

Bristow, T.F., Rampe, E.B., Achilles, C.N., Blake, D.F., Chipera, S.J., Craig, P., Crisp, J.A., Marais, D.J.D., Downs, R.T., Gellert, R., Grotzinger, J.P., Gupta, S., Hazen, R.M., Horgan, B., Hogancamp, J.V., Mangold, N., Mahaffy, P.R., McAdam, A.C., Ming, D.W., Morookian, J.M., Morris, R.V., Morrison, S.M., Treiman, A.H., Vaniman, D.T., Vasavada, A.R., Yen, A.S., 2018. Clay mineral diversity and abundance in sedimentary rocks of Gale crater, Mars. Science Advances 4, eaar3330. https://doi.org/10.1126/sciadv.aar3330

Brown, A.J., Hook, S.J., Baldridge, A.M., Crowley, J.K., Bridges, N.T., Thomson, B.J., Marion, G.M., de Souza Filho, C.R., Bishop, J.L., 2010. Hydrothermal formation of Clay-Carbonate alteration assemblages in the Nili Fossae region of Mars. Earth and Planetary Science Letters 297, 174–182. https://doi.org/10.1016/j.epsl.2010.06.018

Brown, A.J., Viviano, C.E., Goudge, T.A., 2020. Olivine-Carbonate Mineralogy of the Jezero Crater Region. Journal of Geophysical Research: Planets 125, e2019JE006011. https://doi.org/10.1029/2019JE006011

Bryk, A.B., Dietrich, W.E., Lamb, M.P., Grotzinger, J.P., Vasavada, A.R., Stack, K.M., Arvidson, R., Fedo, C., Bennett, K., Fox, V.K., Gupta, S., Wiens, R.C., Williams, R.M.E., 2019. In Curiosity's Path: The Geomorphology and Stratigraphy of the Greenheugh Pediment and Gediz Vallis Ridge in Gale Crater 50, 2263.

Bultel, B., Viennet, J.-C., Poulet, F., Carter, J., Werner, S.C., 2019. Detection of Carbonates in Martian Weathering Profiles. Journal of Geophysical Research: Planets 124, 989–1007. https://doi.org/10.1029/2018JE005845

Calvin, W.M., King, T.V.V., 1997. Spectral characteristics of iron-bearing phyllosilicates: Comparison to Orgueil (CI1), Murchison and Murray (CM2). Meteoritics & Planetary Science 32, 693–701. https://doi.org/10.1111/j.1945-5100.1997.tb01554.x

Cannon, K.M., Mustard, J.F., Parman, S.W., Sklute, E.C., Dyar, M.D., Cooper, R.F., 2017. Spectral properties of Martian and other planetary glasses and their detection in remotely sensed data. Journal of Geophysical Research: Planets 122, 249–268. https://doi.org/10.1002/2016JE005219

Cannon, K.M., Mustard, J.F., Salvatore, M.R., 2015. Alteration of immature sedimentary rocks on Earth and Mars: Recording aqueous and surface–atmosphere processes. Earth and Planetary Science Letters 417, 78–86. https://doi.org/10.1016/j.epsl.2015.02.017

Carrozzo, F.G., Di Achille, G., Salese, F., Altieri, F., Bellucci, G., 2017. Geology and mineralogy of the Auki Crater, Tyrrhena Terra, Mars: A possible post impact-induced hydrothermal system. Icarus 281, 228–239. https://doi.org/10.1016/j.icarus.2016.09.001

Carter, J., Poulet, F., 2012. Orbital identification of clays and carbonates in Gusev crater. Icarus 219, 250–253. https://doi.org/10.1016/j.icarus.2012.02.024

Carter, J., Viviano-Beck, C., Loizeau, D., Bishop, J., Le Deit, L., 2015. Orbital detection and implications of akaganéite on Mars. Icarus 253, 296–310. https://doi.org/10.1016/j.icarus.2015.01.020

Christensen, P.R., Bandfield, J.L., Hamilton, V.E., Ruff, S.W., Kieffer, H.H., Titus, T.N., Malin, M.C., Morris, R.V., Lane, M.D., Clark, R.L., Jakosky, B.M., Mellon, M.T., Pearl, J.C., Conrath, B.J., Smith, M.D., Clancy, R.T., Kuzmin, R.O., Roush, T., Mehall, G.L., Gorelick, N., Bender, K., Murray, K., Dason, S., Greene, E., Silverman, S., Greenfield, M., 2001. Mars Global Surveyor Thermal Emission Spectrometer experiment: Investigation description and surface science results. Journal of Geophysical Research: Planets 106, 23823–23871. https://doi.org/10.1029/2000JE001370

Christensen, P.R., Jakosky, B.M., Kieffer, H.H., Malin, M.C., McSween, H.Y., Nealson, K., Mehall, G.L., Silverman, S.H., Ferry, S., Caplinger, M., Ravine, M., 2004a. The Thermal Emission Imaging System (THEMIS) for the Mars 2001 Odyssey Mission. Space Science Reviews 110, 85–130. https://doi.org/10.1023/B:SPAC.0000021008.16305.94

Christensen, P.R., Jakosky, B.M., Kieffer, H.H., Malin, M.C., McSween, Jr., H.Y., Nealson, K., Mehall, G.L., Silverman, S.H., Ferry, S., Caplinger, M., Ravine, M., 2004b. The Thermal Emission Imaging System (THEMIS) for the Mars 2001 Odyssey Mission. Space Science Reviews 110, 85–130. https://doi.org/10.1023/B:SPAC.0000021008.16305.94

Clark, B.C., Arvidson, R.E., Gellert, R., Morris, R.V., Ming, D.W., Richter, L., Ruff, S.W., Michalski, J.R., Farrand, W.H., Yen, A., Herkenhoff, K.E., Li, R., Squyres, S.W., Schröder, C., Klingelhöfer, G., Bell, J.F., 2007. Evidence for montmorillonite or its compositional equivalent in Columbia Hills, Mars. Journal of Geophysical Research: Planets 112. https://doi.org/10.1029/2006JE002756

Collins, G.S., 2014. Numerical simulations of impact crater formation with dilatancy. Journal of Geophysical Research: Planets 119, 2600–2619. https://doi.org/10.1002/2014JE004708

Corrigan, C.M., Harvey, R.P., 2004. Multi-generational carbonate assemblages in martian meteorite Allan Hills 84001: Implications for nucleation, growth, and alteration. Meteoritics & Planetary Science 39, 17–30. https://doi.org/10.1111/j.1945-5100.2004.tb00047.x

David, G., Cousin, A., Forni, O., Meslin, P.-Y., Dehouck, E., Mangold, N., L'Haridon, J., Rapin, W., Gasnault, O., Johnson, J.R., Ollila, A.M., Newell, A.R., Salvatore, M., Gabriel, T.S.J., Wiens, R.C., Maurice, S., 2020. Analyses of High-Iron Sedimentary Bedrock and Diagenetic Features Observed With ChemCam at Vera Rubin Ridge, Gale Crater, Mars: Calibration and Characterization. Journal of Geophysical Research: Planets 125, e2019JE006314. https://doi.org/10.1029/2019JE006314

Day, M., Dorn, T., 2019. Wind in Jezero Crater, Mars. Geophysical Research Letters 46, 3099–3107. https://doi.org/10.1029/2019GL082218

Dickson, J.L., Ehlmann, B.L., Kerber, L., Fassett, C.I., Hare, T.M., Quinn, D.P., Plesea, L., Noss, D., 2020. The Global CTX Mosaic of Mars: Lessons for the Construction and Dissemination of Massive Imaging Data Sets 51, 2309.

Dobrea, E.Z.N., Wray, J.J., Calef, F.J., Parker, T.J., Murchie, S.L., 2012. Hydrated minerals on Endeavour Crater's rim and interior, and surrounding plains: New insights from CRISM data. Geophysical Research Letters 39. https://doi.org/10.1029/2012GL053180

Dongre, A., Tappe, S., 2019. Kimberlite and carbonatite dykes within the Premier diatreme root (Cullinan Diamond Mine, South Africa): New insights to mineralogical-genetic classifications and magma CO2 degassing. Lithos 338–339, 155–173. https://doi.org/10.1016/j.lithos.2019.04.020

Doroshkevich, A.G., Chebotarev, D.A., Sharygin, V.V., Prokopyev, I.R., Nikolenko, A.M., 2019. Petrology of alkaline silicate rocks and carbonatites of the Chuktukon massif, Chadobets upland, Russia: Sources, evolution and relation to the Triassic Siberian LIP. Lithos 332–333, 245–260. https://doi.org/10.1016/j.lithos.2019.03.006

Drake, H., Heim, C., Roberts, N.M.W., Zack, T., Tillberg, M., Broman, C., Ivarsson, M., Whitehouse, M.J., Åström, M.E., 2017. Isotopic evidence for microbial production and consumption of methane in the upper continental crust throughout the Phanerozoic eon. Earth and Planetary Science Letters 470, 108–118. https://doi.org/10.1016/j.epsl.2017.04.034

Duke, G.I., Carlson, R.W., Frost, C.D., Hearn, B.C., Eby, G.N., 2014. Continent-scale linearity of kimberlite–carbonatite magmatism, mid-continent North America. Earth and Planetary Science Letters 403, 1–14. https://doi.org/10.1016/j.epsl.2014.06.023

Dupraz, C., Reid, R.P., Braissant, O., Decho, A.W., Norman, R.S., Visscher, P.T., 2009. Processes of carbonate precipitation in modern microbial mats. Earth-Science Reviews, Microbial Mats in Earth's Fossil Record of Life: Geobiology 96, 141–162. https://doi.org/10.1016/j.earscirev.2008.10.005

Dupraz, C., Visscher, P.T., Baumgartner, L.K., Reid, R.P., 2004. Microbe–mineral interactions: early carbonate precipitation in a hypersaline lake (Eleuthera Island, Bahamas). Sedimentology 51, 745–765. https://doi.org/10.1111/j.1365-3091.2004.00649.x

Edwards, C.S., Ehlmann, B.L., 2015. Carbon sequestration on Mars. Geology 43, 863–866. https://doi.org/10.1130/G36983.1

Edwards, C.S., Piqueux, S., Hamilton, V.E., Fergason, R.L., Herkenhoff, K.E., Vasavada, A.R., Bennett, K.A., Sacks, L., Lewis, K., Smith, M.D., 2018a. The Thermophysical Properties of the Bagnold Dunes, Mars: Ground-Truthing Orbital Data. Journal of Geophysical Research: Planets 123, 1307–1326. https://doi.org/10.1029/2017JE005501

Edwards, C.S., Piqueux, S., Hamilton, V.E., Fergason, R.L., Herkenhoff, K.E., Vasavada, A.R., Bennett, K.A., Sacks, L., Lewis, K., Smith, M.D., 2018b. The Thermophysical Properties of the Bagnold Dunes, Mars: Ground-Truthing Orbital Data. Journal of Geophysical Research: Planets 123, 1307–1326. https://doi.org/10.1029/2017JE005501

Ehlmann, B.L., Mustard, J.F., 2012. An in-situ record of major environmental transitions on early Mars at Northeast Syrtis Major. Geophysical Research Letters 39. https://doi.org/10.1029/2012GL051594

Ehlmann, B.L., Mustard, J.F., Fassett, C.I., Schon, S.C., Head Iii, J.W., Des Marais, D.J., Grant, J.A., Murchie, S.L., 2008a. Clay minerals in delta deposits and organic preservation potential on Mars. Nature Geoscience 1, 355–358. https://doi.org/10.1038/ngeo207

Ehlmann, B.L., Mustard, J.F., Murchie, S.L., 2010. Geologic setting of serpentine deposits on Mars. Geophysical Research Letters 37. https://doi.org/10.1029/2010GL042596

Ehlmann, B.L., Mustard, J.F., Murchie, S.L., Poulet, F., Bishop, J.L., Brown, A.J., Calvin, W.M., Clark, R.N., Marais, D.J.D., Milliken, R.E., Roach, L.H., Roush, T.L., Swayze, G.A., Wray, J.J., 2008b. Orbital Identification of Carbonate-Bearing Rocks on Mars. Science 322, 1828–1832. https://doi.org/10.1126/science.1164759

Ehlmann, B.L., Mustard, J.F., Swayze, G.A., Clark, R.N., Bishop, J.L., Poulet, F., Marais, D.J.D., Roach, L.H., Milliken, R.E., Wray, J.J., Barnouin-Jha, O., Murchie, S.L., 2009. Identification of hydrated silicate minerals on Mars using MRO-CRISM: Geologic context near Nili Fossae and implications for aqueous alteration. Journal of Geophysical Research: Planets 114. https://doi.org/10.1029/2009JE003339

Evans, O., Spiegelman, M., Kelemen, P.B., 2020. Phase-Field Modeling of Reaction-Driven Cracking: Determining Conditions for Extensive Olivine Serpentinization. Journal of Geophysical Research: Solid Earth 125, e2019JB018614. https://doi.org/10.1029/2019JB018614

Falk, E.S., Kelemen, P.B., 2015. Geochemistry and petrology of listvenite in the Samail ophiolite, Sultanate of Oman: Complete carbonation of peridotite during ophiolite emplacement. Geochimica et Cosmochimica Acta 160, 70–90. https://doi.org/10.1016/j.gca.2015.03.014

Fassett, C.I., Head, J.W., 2005. Fluvial sedimentary deposits on Mars: Ancient deltas in a crater lake in the Nili Fossae region. Geophysical Research Letters 32. https://doi.org/10.1029/2005GL023456

Fergason, R.L., Christensen, P.R., Kieffer, H.H., 2006a. High-resolution thermal inertia derived from the Thermal Emission Imaging System (THEMIS): Thermal model and applications. Journal of Geophysical Research: Planets 111. https://doi.org/10.1029/2006JE002735

Fergason, R.L., Christensen, P.R., Kieffer, H.H., 2006b. High-resolution thermal inertia derived from the Thermal Emission Imaging System (THEMIS): Thermal model and applications. Journal of Geophysical Research E: Planets 111, 1–22. https://doi.org/10.1029/2006JE002735

Fergason, R.L., Hare, T.M., Mayer, D.P., Galuszka, D.M., Redding, B.L., Smith, E.D., Shinaman, J.R., Cheng, Y., Otero, R.E., 2020. Mars 2020 Terrain Relative Navigation Flight Product Generation: Digital Terrain Model and Orthorectified Image Mosaic 51, 2020.

Fischer, P.D., Brown, M.E., Hand, K.P., 2015. SPATIALLY RESOLVED SPECTROSCOPY OF EUROPA: THE DISTINCT SPECTRUM OF LARGE-SCALE CHAOS. AJ 150, 164. https://doi.org/10.1088/0004-6256/150/5/164

Fox, V.K., Arvidson, R.E., Guinness, E.A., McLennan, S.M., Catalano, J.G., Murchie, S.L., Powell, K.E., 2016. Smectite deposits in Marathon Valley, Endeavour Crater, Mars, identified using CRISM hyperspectral reflectance data. Geophysical Research Letters 43, 4885–4892. https://doi.org/10.1002/2016GL069108

Fraeman, A.A., Arvidson, R.E., Catalano, J.G., Grotzinger, J.P., Morris, R.V., Murchie, S.L., Stack, K.M., Humm, D.C., McGovern, J.A., Seelos, F.P., Seelos, K.D., Viviano, C.E., 2013. A hematite-bearing layer in Gale Crater, Mars: Mapping and implications for past aqueous conditions. Geology 41, 1103–1106. https://doi.org/10.1130/G34613.1

Fraeman, A.A., Edgar, L.A., Rampe, E.B., Thompson, L.M., Frydenvang, J., Fedo, C.M., Catalano, J.G., Dietrich, W.E., Gabriel, T.S.J., Vasavada, A.R., Grotzinger, J.P., L'Haridon, J., Mangold, N., Sun, V.Z., House, C.H., Bryk, A.B., Hardgrove, C., Czarnecki, S., Stack, K.M., Morris, R.V., Arvidson, R.E., Banham, S.G., Bennett, K.A., Bridges, J.C., Edwards, C.S., Fischer, W.W., Fox, V.K., Gupta, S., Horgan, B.H.N., Jacob, S.R., Johnson, J.R., Johnson, S.S., Rubin, D.M., Salvatore, M.R., Schwenzer, S.P., Siebach, K.L., Stein, N.T., Turner, S.M.R., Wellington, D.F., Wiens, R.C., Williams, A.J., David, G., Wong, G.M., 2020a. Evidence for a Diagenetic Origin of Vera Rubin Ridge, Gale Crater, Mars: Summary and Synthesis of Curiosity's Exploration Campaign. Journal of Geophysical Research: Planets 125, e2020JE006527. https://doi.org/10.1029/2020JE006527

Fraeman, A.A., Ehlmann, B.L., Arvidson, R.E., Edwards, C.S., Grotzinger, J.P., Milliken, R.E., Quinn, D.P., Rice, M.S., 2016. The stratigraphy and evolution of lower Mount Sharp from spectral, morphological, and thermophysical orbital data sets. Journal of Geophysical Research: Planets 121, 1713–1736. https://doi.org/10.1002/2016JE005095

Fraeman, A.A., Johnson, J.R., Arvidson, R.E., Rice, M.S., Wellington, D.F., Morris, R.V., Fox, V.K., Horgan, B.H.N., Jacob, S.R., Salvatore, M.R., Sun, V.Z., Pinet, P., Bell, J.F., Wiens, R.C., Vasavada, A.R., 2020b. Synergistic Ground and Orbital Observations of Iron Oxides on Mt. Sharp and Vera Rubin Ridge. Journal of Geophysical Research: Planets 125, e2019JE006294. https://doi.org/10.1029/2019JE006294

Frydenvang, J., Mangold, N., Wiens, R.C., Fraeman, A.A., Edgar, L.A., Fedo, C.M., L'Haridon, J., Bedford, C.C., Gupta, S., Grotzinger, J.P., Bridges, J.C., Clark, B.C., Rampe, E.B., Gasnault, O., Maurice, S.,

Gasda, P.J., Lanza, N.L., Olilla, A.M., Meslin, P.-Y., Payré, V., Calef, F., Salvatore, M., House, C.H., 2020. The Chemostratigraphy of the Murray Formation and Role of Diagenesis at Vera Rubin Ridge in Gale Crater, Mars, as Observed by the ChemCam Instrument. Journal of Geophysical Research: Planets 125, e2019JE006320. https://doi.org/10.1029/2019JE006320

Given, R.K., Wilkinson, B.H., 1985. Kinetic control of morphology, composition, and mineralogy of abiotic sedimentary carbonates. Journal of Sedimentary Research 55, 109–119. https://doi.org/10.1306/212F862A-2B24-11D7-8648000102C1865D

Glotch, T.D., Bandfield, J.L., 2006. Determination and interpretation of surface and atmospheric Miniature Thermal Emission Spectrometer spectral end-members at the Meridiani Planum landing site. Journal of Geophysical Research: Planets 111. https://doi.org/10.1029/2005JE002671

Glotch, T.D., Bandfield, J.L., Christensen, P.R., Calvin, W.M., McLennan, S.M., Clark, B.C., Rogers, A.D., Squyres, S.W., 2006. Mineralogy of the light-toned outcrop at Meridiani Planum as seen by the Miniature Thermal Emission Spectrometer and implications for its formation. Journal of Geophysical Research: Planets 111. https://doi.org/10.1029/2005JE002672

Glotch, T.D., Rogers, A.D., 2013. Evidence for magma-carbonate interaction beneath Syrtis Major, Mars. Journal of Geophysical Research: Planets 118, 126–137. https://doi.org/10.1029/2012JE004230

Glover, C., Robertson, A.H.F., 2003. Origin of tufa (cool-water carbonate) and related terraces in the Antalya area, SW Turkey. Geological Journal 38, 329–358. https://doi.org/10.1002/gj.959

Gooding, J.L., Wentworth, S.J., Zolensky, M.E., 1991. Aqueous alteration of the Nakhla meteorite. Meteoritics 26, 135–143. https://doi.org/10.1111/j.1945-5100.1991.tb01029.x

Goudge, T.A., Milliken, R.E., Head, J.W., Mustard, J.F., Fassett, C.I., 2017. Sedimentological evidence for a deltaic origin of the western fan deposit in Jezero crater, Mars and implications for future exploration. Earth and Planetary Science Letters 458, 357–365. https://doi.org/10.1016/j.epsl.2016.10.056

Goudge, T.A., Mohrig, D., Cardenas, B.T., Hughes, C.M., Fassett, C.I., 2018. Stratigraphy and paleohydrology of delta channel deposits, Jezero crater, Mars. Icarus 301, 58–75. https://doi.org/10.1016/j.icarus.2017.09.034

Goudge, T.A., Mustard, J.F., Head, J.W., Fassett, C.I., Wiseman, S.M., 2015. Assessing the mineralogy of the watershed and fan deposits of the Jezero crater paleolake system, Mars. Journal of Geophysical Research: Planets 120, 775–808. https://doi.org/10.1002/2014JE004782

Greely, R., Guest, J., 1987. Geologic map of the eastern equatorial region of Mars.

Halevy, I., Fischer, W.W., Eiler, J.M., 2011. Carbonates in the Martian meteorite Allan Hills 84001 formed at 18 ± 4 °C in a near-surface aqueous environment. PNAS 108, 16895–16899. https://doi.org/10.1073/pnas.1109444108

Hamran, S.-E., Paige, D.A., Amundsen, H.E.F., Berger, T., Brovoll, S., Carter, L., Damsgård, L., Dypvik, H., Eide, J., Eide, S., Ghent, R., Helleren, Ø., Kohler, J., Mellon, M., Nunes, D.C., Plettemeier, D., Rowe, K., Russell, P., Øyan, M.J., 2020. Radar Imager for Mars' Subsurface Experiment—RIMFAX. Space Sci Rev 216, 128. https://doi.org/10.1007/s11214-020-00740-4

Hays, L.E., Graham, H.V., Des Marais, D.J., Hausrath, E.M., Horgan, B., McCollom, T.M., Parenteau, M.N., Potter-McIntyre, S.L., Williams, A.J., Lynch, K.L., 2017. Biosignature Preservation and Detection in Mars Analog Environments. Astrobiology 17, 363–400. https://doi.org/10.1089/ast.2016.1627

Hoefen, T.M., Clark, R.N., Bandfield, J.L., Smith, M.D., Pearl, J.C., Christensen, P.R., 2003. Discovery of Olivine in the Nili Fossae Region of Mars. Science 302, 627–630. https://doi.org/10.1126/science.1089647

Horgan, B.H.N., Anderson, R.B., Dromart, G., Amador, E.S., Rice, M.S., 2020a. The mineral diversity of Jezero crater: Evidence for possible lacustrine carbonates on Mars. Icarus 339, 113526. https://doi.org/10.1016/j.icarus.2019.113526

Horgan, B.H.N., Johnson, J.R., Fraeman, A.A., Rice, M.S., Seeger, C., Bell, J.F., Bennett, K.A., Cloutis, E.A., Edgar, L.A., Frydenvang, J., Grotzinger, J.P., L'Haridon, J., Jacob, S.R., Mangold, N., Rampe, E.B., Rivera-Hernandez, F., Sun, V.Z., Thompson, L.M., Wellington, D., 2020b. Diagenesis of Vera Rubin Ridge, Gale Crater, Mars, From Mastcam Multispectral Images. Journal of Geophysical Research: Planets 125, e2019JE006322. https://doi.org/10.1029/2019JE006322

Hundal, C.B., Mustard, J.F., Kremer, C.H., 2020. Origin of the Pitted Capping Unit in Nili Fossae, Mars 51, 1629.

Itoh, Y., Parente, M., 2021. A new method for atmospheric correction and de-noising of CRISM hyperspectral data. Icarus 354, 114024. https://doi.org/10.1016/j.icarus.2020.114024

Ivarsson, M., Bach, W., Broman, C., Neubeck, A., Bengtson, S., 2018. Fossilized Life in Subseafloor Ultramafic Rocks. Geomicrobiology Journal 35, 460–467. https://doi.org/10.1080/01490451.2017.1370517

Ivarsson, M., Bengtson, S., Belivanova, V., Stampanoni, M., Marone, F., Tehler, A., 2012. Fossilized fungi in subseafloor Eocene basalts. Geology 40, 163–166. https://doi.org/10.1130/G32590.1

Jacob, S.R., Wellington, D.F., Bell, J.F., Achilles, C., Fraeman, A.A., Horgan, B., Johnson, J.R., Maurice, S., Peters, G.H., Rampe, E.B., Thompson, L.M., Wiens, R.C., 2020. Spectral, Compositional, and Physical Properties of the Upper Murray Formation and Vera Rubin Ridge, Gale Crater, Mars. Journal of Geophysical Research: Planets 125, e2019JE006290. https://doi.org/10.1029/2019JE006290

Jain, N., Chauhan, P., 2015. Study of phyllosilicates and carbonates from the Capri Chasma region of Valles Marineris on Mars based on Mars Reconnaissance Orbiter-Compact Reconnaissance Imaging Spectrometer for Mars (MRO-CRISM) observations. Icarus 250, 7–17. https://doi.org/10.1016/j.icarus.2014.11.018

Jull, A.J.T., Cheng, S., Gooding, J.L., Velbel, M.A., 1988. Rapid Growth of Magnesium-Carbonate Weathering Products in a Stony Meteorite from Antarctica. Science 242, 417–419. https://doi.org/10.1126/science.242.4877.417

Kah, L.C., Lyons, T.W., Chesley, J.T., 2001. Geochemistry of a 1.2 Ga carbonate-evaporite succession, northern Baffin and Bylot Islands: implications for Mesoproterozoic marine evolution. Precambrian Research 111, 203–234. https://doi.org/10.1016/S0301-9268(01)00161-9

Kelemen, P.B., Evans, O., Ghiorso, M., Mustard, J., Ehlmann, B.L., Spiegelman, M., 2020a. Carbonate in Olivine-Rich Unit(s) on Mars May Have Formed at Low P(H2O) 51, 1213.

Kelemen, P.B., Hirth, G., 2012. Reaction-driven cracking during retrograde metamorphism: Olivine hydration and carbonation. Earth and Planetary Science Letters 345–348, 81–89. https://doi.org/10.1016/j.epsl.2012.06.018

Kelemen, P.B., Matter, J., 2008. In situ carbonation of peridotite for CO2 storage. PNAS 105, 17295–17300. https://doi.org/10.1073/pnas.0805794105

Kelemen, P.B., Matter, J., Streit, E.E., Rudge, J.F., Curry, W.B., Blusztajn, J., 2011. Rates and Mechanisms of Mineral Carbonation in Peridotite: Natural Processes and Recipes for Enhanced, in situ CO2 Capture and Storage. Annual Review of Earth and Planetary Sciences 39, 545–576. https://doi.org/10.1146/annurev-earth-092010-152509

Kelemen, P.B., Teagle, D.A.H., Matter, J.M., Coggon, J.A., the Oman Drilling Project Science, 2020b. Oman Drilling Project, Scientific Drilling in the Samail Ophiolite, Sultanate of Oman [WWW Document]. https://doi.org/10.14379/OmanDP.proc.2020

Kieffer, H.H., 2013. Thermal model for analysis of Mars infrared mapping. Journal of Geophysical Research E: Planets 118, 451–470. https://doi.org/10.1029/2012JE004164

Klein, F., Humphris, S.E., Guo, W., Schubotz, F., Schwarzenbach, E.M., Orsi, W.D., 2015. Fluid mixing and the deep biosphere of a fossil Lost City-type hydrothermal system at the Iberia Margin. PNAS 112, 12036–12041. https://doi.org/10.1073/pnas.1504674112

Klein, F., Le Roux, V., 2020. Quantifying the volume increase and chemical exchange during serpentinization. Geology 48, 552–556. https://doi.org/10.1130/G47289.1

Kraus, E.A., Nothaft, D., Stamps, B.W., Rempfert, K.R., Ellison, E.T., Matter, J.M., Templeton, A.S., Boyd, E.S., Spear, J.R., 2021. Molecular Evidence for an Active Microbial Methane Cycle in Subsurface Serpentinite-Hosted Groundwaters in the Samail Ophiolite, Oman. Appl. Environ. Microbiol. 87. https://doi.org/10.1128/AEM.02068-20

Kremer, C.H., Mustard, J.F., Bramble, M.S., 2019. A widespread olivine-rich ash deposit on Mars. Geology 47, 677–681. https://doi.org/10.1130/G45563.1

Lane, M.D., Dyar, M.D., Bishop, J.L., 2004. Spectroscopic evidence for hydrous iron sulfate in the Martian soil. Geophysical Research Letters 31. https://doi.org/10.1029/2004GL021231

Laskar, J., Correia, A.C.M., Gastineau, M., Joutel, F., Levrard, B., Robutel, P., 2004. Long term evolution and chaotic diffusion of the insolation quantities of Mars. Icarus 170, 343–364. https://doi.org/10.1016/j.icarus.2004.04.005

Leask, E.K., Ehlmann, B.L., Dundar, M.M., Murchie, S.L., Seelos, F.P., 2018. Challenges in the Search for Perchlorate and Other Hydrated Minerals With 2.1-μm Absorptions on Mars. Geophysical Research Letters 45, 12,180-12,189. https://doi.org/10.1029/2018GL080077

L'Haridon, J., Mangold, N., Fraeman, A.A., Johnson, J.R., Cousin, A., Rapin, W., David, G., Dehouck, E., Sun, V., Frydenvang, J., Gasnault, O., Gasda, P., Lanza, N., Forni, O., Meslin, P.-Y., Schwenzer, S.P., Bridges, J., Horgan, B., House, C.H., Salvatore, M., Maurice, S., Wiens, R.C., 2020. Iron Mobility During Diagenesis at Vera Rubin Ridge, Gale Crater, Mars. Journal of Geophysical Research: Planets 125, e2019JE006299. https://doi.org/10.1029/2019JE006299

Lin, H., Tarnas, J.D., Mustard, J.F., Zhang, X., Wei, Y., Wan, W., Klein, F., Kellner, J.R., 2021. Dynamic aperture factor analysis/target transformation (DAFA/TT) for Mg-serpentine and Mg-carbonate mapping on Mars with CRISM near-infrared data. Icarus 355, 114168. https://doi.org/10.1016/j.icarus.2020.114168

Malin, M.C., Bell, J.F., Cantor, B.A., Caplinger, M.A., Calvin, W.M., Clancy, R.T., Edgett, K.S., Edwards, L., Haberle, R.M., James, P.B., Lee, S.W., Ravine, M.A., Thomas, P.C., Wolff, M.J., 2007. Context Camera Investigation on board the Mars Reconnaissance Orbiter. Journal of Geophysical Research: Planets 112. https://doi.org/10.1029/2006JE002808

Mandon, L., Quantin-Nataf, C., Thollot, P., Mangold, N., Lozac'h, L., Dromart, G., Beck, P., Dehouck, E., Breton, S., Millot, C., Volat, M., 2020. Refining the age, emplacement and alteration scenarios of the olivine-rich unit in the Nili Fossae region, Mars. Icarus 336, 113436. https://doi.org/10.1016/j.icarus.2019.113436

Matter, J.M., Kelemen, P.B., 2009. Permanent storage of carbon dioxide in geological reservoirs by mineral carbonation. Nature Geoscience 2, 837–841. https://doi.org/10.1038/ngeo683

McAdam, A.C., Sutter, B., Archer, P.D., Franz, H.B., Wong, G.M., Lewis, J.M.T., Eigenbrode, J.L., Stern, J.C., Knudson, C.A., Clark, J.V., Andrejkovičová, S., Ming, D.W., Morris, R.V., Achilles, C.N., Rampe, E.B., Bristow, T.F., Navarro-González, R., Mahaffy, P.R., Thompson, L.M., Gellert, R., Williams, A.J., House, C.H., Johnson, S.S., 2020. Constraints on the Mineralogy and Geochemistry of Vera Rubin Ridge, Gale Crater, Mars, From Mars Science Laboratory Sample Analysis at Mars Evolved Gas Analyses. Journal of Geophysical Research: Planets 125, e2019JE006309. https://doi.org/10.1029/2019JE006309

McEwen, A.S., Eliason, E.M., Bergstrom, J.W., Bridges, N.T., Hansen, C.J., Delamere, W.A., Grant, J.A., Gulick, V.C., Herkenhoff, K.E., Keszthelyi, L., Kirk, R.L., Mellon, M.T., Squyres, S.W., Thomas, N., Weitz, C.M., 2007. Mars Reconnaissance Orbiter's High Resolution Imaging Science Experiment (HiRISE). Journal of Geophysical Research: Planets 112. https://doi.org/10.1029/2005JE002605

McKinley, F.W., T.O. Stevens, 2000. Microfossils and Paleoenvironments in Deep Subsurface Basalt Samples. Geomicrobiology Journal 17, 43–54. https://doi.org/10.1080/014904500270486

McMahon, S., Bosak, T., Grotzinger, J.P., Milliken, R.E., Summons, R.E., Daye, M., Newman, S.A., Fraeman, A., Williford, K.H., Briggs, D.E.G., 2018. A Field Guide to Finding Fossils on Mars. Journal of Geophysical Research: Planets 123, 1012–1040. https://doi.org/10.1029/2017JE005478

McSween, H.Y., 1994. What we have learned about Mars from SNC meteorites. Meteoritics 29, 757–779. https://doi.org/10.1111/j.1945-5100.1994.tb01092.x

Melluso, L., Srivastava, R.K., Guarino, V., Zanetti, A., Sinha, A.K., 2010. MINERAL COMPOSITIONS AND PETROGENETIC EVOLUTION OF THE ULTRAMAFIC-ALKALINE – CARBONATITIC COMPLEX OF SUNG VALLEY, NORTHEASTERN INDIA. The Canadian Mineralogist 48, 205–229. https://doi.org/10.3749/canmin.48.1.205

Michalski, J.R., Cuadros, J., Niles, P.B., Parnell, J., Deanne Rogers, A., Wright, S.P., 2013. Groundwater activity on Mars and implications for a deep biosphere. Nature Geoscience 6, 133–138. https://doi.org/10.1038/ngeo1706

Michalski, J.R., Dobrea, E.Z.N., Niles, P.B., Cuadros, J., 2017. Ancient hydrothermal seafloor deposits in Eridania basin on Mars. Nature Communications 8, 15978. https://doi.org/10.1038/ncomms15978

Michalski, J.R., Niles, P.B., 2010. Deep crustal carbonate rocks exposed by meteor impact on Mars. Nature Geoscience 3, 751–755. https://doi.org/10.1038/ngeo971

Michalski, J.R., Onstott, T.C., Mojzsis, S.J., Mustard, J., Chan, Q.H.S., Niles, P.B., Johnson, S.S., 2018. The Martian subsurface as a potential window into the origin of life. Nature Geoscience 11, 21–26. https://doi.org/10.1038/s41561-017-0015-2

Mitchell, R.H., 2013. Paragenesis and Oxygen Isotopic Studies of Serpentine in Kimberlite, in: Pearson, D.G., Grütter, H.S., Harris, J.W., Kjarsgaard, B.A., O'Brien, H., Rao, N.V.C., Sparks, S. (Eds.), Proceedings of 10th International Kimberlite Conference. Springer India, New Delhi, pp. 1–12. https://doi.org/10.1007/978-81-322-1170-9_1

Mitchell, R.H., 2008. Petrology of hypabyssal kimberlites: Relevance to primary magma compositions. Journal of Volcanology and Geothermal Research, Kimberlite Emplacement 174, 1–8. https://doi.org/10.1016/j.jvolgeores.2007.12.024

Mitchell, R.H., Giuliani, A., O'Brien, H., 2019. What is a Kimberlite? Petrology and Mineralogy of Hypabyssal Kimberlites. Elements 15, 381–386. https://doi.org/10.2138/gselements.15.6.381

Mitchell, R.H., Skinner, E.M.W., Scott Smith, B.H., 2009. Tuffisitic kimberlites from the Wesselton Mine, South Africa: Mineralogical characteristics relevant to their formation. Lithos, Proceedings of the 9th International Kimberlite Conference 112, 452–464. https://doi.org/10.1016/j.lithos.2009.06.018

Moody, J.B., 1976. Serpentinization: a review. Lithos 9, 125–138. https://doi.org/10.1016/0024-4937(76)90030-X

Morris, R.V., Klingelhöfer, G., Schröder, C., Rodionov, D.S., Yen, A., Ming, D.W., Souza, P.A. de, Fleischer, I., Wdowiak, T., Gellert, R., Bernhardt, B., Evlanov, E.N., Zubkov, B., Foh, J., Bonnes, U., Kankeleit, E., Gütlich, P., Renz, F., Squyres, S.W., Arvidson, R.E., 2006. Mössbauer mineralogy of rock, soil, and dust at Gusev crater, Mars: Spirit's journey through weakly altered olivine basalt on the plains and pervasively altered basalt in the Columbia Hills. Journal of Geophysical Research: Planets 111. https://doi.org/10.1029/2005JE002584

Morris, R.V., Rampe, E.B., Vaniman, D.T., Christoffersen, R., Yen, A.S., Morrison, S.M., Ming, D.W., Achilles, C.N., Fraeman, A.A., Le, L., Tu, V.M., Ott, J.P., Treiman, A.H., Hogancamp, J.V., Graff, T.G., Adams, M., Hamilton, J.C., Mertzman, S.A., Bristow, T.F., Blake, D.F., Castle, N., Chipera, S.J., Craig, P.I., Marais, D.J.D., Downs, G., Downs, R.T., Hazen, R.M., Morookian, J.-M., Thorpe, M., 2020. Hydrothermal Precipitation of Sanidine (Adularia) Having Full Al,Si Structural Disorder

and Specular Hematite at Maunakea Volcano (Hawai'i) and at Gale Crater (Mars). Journal of Geophysical Research: Planets 125, e2019JE006324. https://doi.org/10.1029/2019JE006324
Morris, R.V., Ruff, S.W., Gellert, R., Ming, D.W., Arvidson, R.E., Clark, B.C., Golden, D.C., Siebach, K., Klingelhöfer, G., Schröder, C., Fleischer, I., Yen, A.S., Squyres, S.W., 2010. Identification of Carbonate-Rich Outcrops on Mars by the Spirit Rover. Science 329, 421–424. https://doi.org/10.1126/science.1189667
Murchie, S., Arvidson, R., Bedini, P., Beisser, K., Bibring, J.-P., Bishop, J., Boldt, J., Cavender, P., Choo, T., Clancy, R.T., Darlington, E.H., Marais, D.D., Espiritu, R., Fort, D., Green, R., Guinness, E., Hayes, J., Hash, C., Heffernan, K., Hemmler, J., Heyler, G., Humm, D., Hutcheson, J., Izenberg, N., Lee, R., Lees, J., Lohr, D., Malaret, E., Martin, T., McGovern, J.A., McGuire, P., Morris, R., Mustard, J., Pelkey, S., Rhodes, E., Robinson, M., Roush, T., Schaefer, E., Seagrave, G., Seelos, F., Silverglate, P., Slavney, S., Smith, M., Shyong, W.-J., Strohbehn, K., Taylor, H., Thompson, P., Tossman, B., Wirzburger, M., Wolff, M., 2007. Compact Reconnaissance Imaging Spectrometer for Mars (CRISM) on Mars Reconnaissance Orbiter (MRO). Journal of Geophysical Research: Planets 112. https://doi.org/10.1029/2006JE002682
Mustard, J.F., Ehlmann, B.L., Murchie, S.L., Poulet, F., Mangold, N., Head, J.W., Bibring, J.-P., Roach, L.H., 2009. Composition, Morphology, and Stratigraphy of Noachian Crust around the Isidis basin. Journal of Geophysical Research: Planets 114. https://doi.org/10.1029/2009JE003349
Mustard, J.F., Murchie, S.L., Pelkey, S.M., Ehlmann, B.L., Milliken, R.E., Grant, J.A., Bibring, J.-P., Poulet, F., Bishop, J., Dobrea, E.N., Roach, L., Seelos, F., Arvidson, R.E., Wiseman, S., Green, R., Hash, C., Humm, D., Malaret, E., McGovern, J.A., Seelos, K., Clancy, T., Clark, R., Marais, D.D., Izenberg, N., Knudson, A., Langevin, Y., Martin, T., McGuire, P., Morris, R., Robinson, M., Roush, T., Smith, M., Swayze, G., Taylor, H., Titus, T., Wolff, M., 2008. Hydrated silicate minerals on Mars observed by the Mars Reconnaissance Orbiter CRISM instrument. Nature 454, 305–309. https://doi.org/10.1038/nature07097
Newman, S.A., Lincoln, S.A., O'Reilly, S., Liu, X., Shock, E.L., Kelemen, P.B., Summons, R.E., 2020. Lipid Biomarker Record of the Serpentinite-Hosted Ecosystem of the Samail Ophiolite, Oman and Implications for the Search for Biosignatures on Mars. Astrobiology 20, 830–845. https://doi.org/10.1089/ast.2019.2066
O'Connor, W.K., Dahlin, D.C., Rush, G.E., Gerdemann, S.J., Penner, L.R., Nilsen, D., 2005. Aqueous mineral carbonation. Final Report–DOE/ARC-TR-04-002.
Ody, A., Poulet, F., Bibring, J.-P., Loizeau, D., Carter, J., Gondet, B., Langevin, Y., 2013. Global investigation of olivine on Mars: Insights into crust and mantle compositions. Journal of Geophysical Research: Planets 118, 234–262. https://doi.org/10.1029/2012JE004149
Oelkers, E.H., Gislason, S.R., Matter, J., 2008. Mineral Carbonation of CO2. Elements 4, 333–337. https://doi.org/10.2113/gselements.4.5.333
Onstott, T. c., Ehlmann, B. l., Sapers, H., Coleman, M., Ivarsson, M., Marlow, J. j., Neubeck, A., Niles, P., 2019. Paleo-Rock-Hosted Life on Earth and the Search on Mars: A Review and Strategy for Exploration. Astrobiology 19, 1230–1262. https://doi.org/10.1089/ast.2018.1960
Palumbo, A.M., Head, J.W., 2018. Impact cratering as a cause of climate change, surface alteration, and resurfacing during the early history of Mars. Meteoritics & Planetary Science 53, 687–725. https://doi.org/10.1111/maps.13001
Parente, M., Arvidson, R., Itoh, Y., Lin, H., Mustard, J.F., Saranathan, A.M., Seelos, F.P., Tarnas, J.D., 2019. Mineral Detections over Jezero Crater Using Advanced Data Processing Techniques for CRISM Data — The CRISM "Fandango." LPI Contributions 2089, 6382.
Poulet, F., Bibring, J.-P., Mustard, J.F., Gendrin, A., Mangold, N., Langevin, Y., Arvidson, R.E., Gondet, B., Gomez, C., 2005. Phyllosilicates on Mars and implications for early martian climate. Nature 438, 623–627. https://doi.org/10.1038/nature04274

Putzig, N.E., Mellon, M.T., Kretke, K.A., Arvidson, R.E., 2005. Global thermal inertia and surface properties of Mars from the MGS mapping mission. Icarus 173, 325–341. https://doi.org/10.1016/j.icarus.2004.08.017

Quinn, D.P., Ehlmann, B.L., 2019. The Deposition and Alteration History of the Northeast Syrtis Major Layered Sulfates. Journal of Geophysical Research: Planets 124, 1743–1782. https://doi.org/10.1029/2018JE005706

Rampe, E.B., Bristow, T.F., Morris, R.V., Morrison, S.M., Achilles, C.N., Ming, D.W., Vaniman, D.T., Blake, D.F., Tu, V.M., Chipera, S.J., Yen, A.S., Peretyazhko, T.S., Downs, R.T., Hazen, R.M., Treiman, A.H., Grotzinger, J.P., Castle, N., Craig, P.I., Marais, D.J.D., Thorpe, M.T., Walroth, R.C., Downs, G.W., Fraeman, A.A., Siebach, K.L., Gellert, R., Lafuente, B., McAdam, A.C., Meslin, P.-Y., Sutter, B., Salvatore, M.R., 2020. Mineralogy of Vera Rubin Ridge From the Mars Science Laboratory CheMin Instrument. Journal of Geophysical Research: Planets 125, e2019JE006306. https://doi.org/10.1029/2019JE006306

Rampe, E.B., Ming, D.W., Blake, D.F., Bristow, T.F., Chipera, S.J., Grotzinger, J.P., Morris, R.V., Morrison, S.M., Vaniman, D.T., Yen, A.S., Achilles, C.N., Craig, P.I., Des Marais, D.J., Downs, R.T., Farmer, J.D., Fendrich, K.V., Gellert, R., Hazen, R.M., Kah, L.C., Morookian, J.M., Peretyazhko, T.S., Sarrazin, P., Treiman, A.H., Berger, J.A., Eigenbrode, J., Fairén, A.G., Forni, O., Gupta, S., Hurowitz, J.A., Lanza, N.L., Schmidt, M.E., Siebach, K., Sutter, B., Thompson, L.M., 2017. Mineralogy of an ancient lacustrine mudstone succession from the Murray formation, Gale crater, Mars. Earth and Planetary Science Letters 471, 172–185. https://doi.org/10.1016/j.epsl.2017.04.021

Rempfert, K.R., Miller, H.M., Bompard, N., Nothaft, D., Matter, J.M., Kelemen, P., Fierer, N., Templeton, A.S., 2017. Geological and Geochemical Controls on Subsurface Microbial Life in the Samail Ophiolite, Oman. Front. Microbiol. 8. https://doi.org/10.3389/fmicb.2017.00056

Rice, M.S., Bell, J.F., Cloutis, E.A., Wang, A., Ruff, S.W., Craig, M.A., Bailey, D.T., Johnson, J.R., de Souza, P.A., Farrand, W.H., 2010. Silica-rich deposits and hydrated minerals at Gusev Crater, Mars: Vis-NIR spectral characterization and regional mapping. Icarus 205, 375–395. https://doi.org/10.1016/j.icarus.2009.03.035

Rogers, A.D., Warner, N.H., Golombek, M.P., Head, J.W., Cowart, J.C., 2018. Areally Extensive Surface Bedrock Exposures on Mars: Many Are Clastic Rocks, Not Lavas. Geophysical Research Letters 45, 1767–1777. https://doi.org/10.1002/2018GL077030

Ruff, S.W., Farmer, J.D., Calvin, W.M., Herkenhoff, K.E., Johnson, J.R., Morris, R.V., Rice, M.S., Arvidson, R.E., Bell, J.F., Christensen, P.R., Squyres, S.W., 2011. Characteristics, distribution, origin, and significance of opaline silica observed by the Spirit rover in Gusev crater, Mars. Journal of Geophysical Research: Planets 116. https://doi.org/10.1029/2010JE003767

Ruff, S.W., Hamilton, V.E., Rogers, A.D., Edwards, C.S., Horgan, B., 2019. Olivine-Rich, Carbonate-Bearing Ash Deposits Link Jezero and Gusev Craters. LPI 2775.

Ruff, S.W., Niles, P.B., Alfano, F., Clarke, A.B., 2014. Evidence for a Noachian-aged ephemeral lake in Gusev crater, Mars. Geology 42, 359–362. https://doi.org/10.1130/G35508.1

Russell, J.K., Porritt, L.A., Lavallée, Y., Dingwell, D.B., 2012. Kimberlite ascent by assimilation-fuelled buoyancy. Nature 481, 352–356. https://doi.org/10.1038/nature10740

Salvatore, M.R., Mustard, J.F., Head, J.W., Cooper, R.F., Marchant, D.R., Wyatt, M.B., 2013. Development of alteration rinds by oxidative weathering processes in Beacon Valley, Antarctica, and implications for Mars. Geochimica et Cosmochimica Acta 115, 137–161. https://doi.org/10.1016/j.gca.2013.04.002

Saranathan, A.M., Parente, M., 2021. Adversarial feature learning for improved mineral mapping of CRISM data. Icarus 355, 114107. https://doi.org/10.1016/j.icarus.2020.114107

Scheller, E.L., Ehlmann, B.L., 2020. Composition, Stratigraphy, and Geological History of the Noachian Basement Surrounding the Isidis Impact Basin. Journal of Geophysical Research: Planets 125, e2019JE006190. https://doi.org/10.1029/2019JE006190

Schon, S.C., Head, J.W., Fassett, C.I., 2012. An overfilled lacustrine system and progradational delta in Jezero crater, Mars: Implications for Noachian climate. Planetary and Space Science 67, 28–45. https://doi.org/10.1016/j.pss.2012.02.003

Schrenk, M.O., Brazelton, W.J., Lang, S.Q., 2013. Serpentinization, Carbon, and Deep Life. Reviews in Mineralogy and Geochemistry 75, 575–606. https://doi.org/10.2138/rmg.2013.75.18

Shavers, E.J., Ghulam, A., Encarnacion, J., Bridges, D.L., Luetkemeyer, P.B., 2016. Carbonatite associated with ultramafic diatremes in the Avon Volcanic District, Missouri, USA: Field, petrographic, and geochemical constraints. Lithos 248–251, 506–516. https://doi.org/10.1016/j.lithos.2016.02.005

Smith, M.D., Bandfield, J.L., Christensen, P.R., 2000. Separation of atmospheric and surface spectral features in Mars Global Surveyor Thermal Emission Spectrometer (TES) spectra. Journal of Geophysical Research: Planets 105, 9589–9607. https://doi.org/10.1029/1999JE001105

Sparks, R.S.J., 2013. Kimberlite Volcanism. Annual Review of Earth and Planetary Sciences 41, 497–528. https://doi.org/10.1146/annurev-earth-042711-105252

Sparks, R.S.J., Brooker, R.A., Field, M., Kavanagh, J., Schumacher, J.C., Walter, M.J., White, J., 2009. The nature of erupting kimberlite melts. Lithos, Proceedings of the 9th International Kimberlite Conference 112, 429–438. https://doi.org/10.1016/j.lithos.2009.05.032

Squyres, S.W., Arvidson, R.E., Ruff, S., Gellert, R., Morris, R.V., Ming, D.W., Crumpler, L., Farmer, J.D., Marais, D.J.D., Yen, A., McLennan, S.M., Calvin, W., Bell, J.F., Clark, B.C., Wang, A., McCoy, T.J., Schmidt, M.E., Souza, P.A. de, 2008. Detection of Silica-Rich Deposits on Mars. Science 320, 1063–1067. https://doi.org/10.1126/science.1155429

Stack, K.M., Williams, N.R., Calef, F., Sun, V.Z., Williford, K.H., Farley, K.A., Eide, S., Flannery, D., Hughes, C., Jacob, S.R., Kah, L.C., Meyen, F., Molina, A., Nataf, C.Q., Rice, M., Russell, P., Scheller, E., Seeger, C.H., Abbey, W.J., Adler, J.B., Amundsen, H., Anderson, R.B., Angel, S.M., Arana, G., Atkins, J., Barrington, M., Berger, T., Borden, R., Boring, B., Brown, A., Carrier, B.L., Conrad, P., Dypvik, H., Fagents, S.A., Gallegos, Z.E., Garczynski, B., Golder, K., Gomez, F., Goreva, Y., Gupta, S., Hamran, S.-E., Hicks, T., Hinterman, E.D., Horgan, B.N., Hurowitz, J., Johnson, J.R., Lasue, J., Kronyak, R.E., Liu, Y., Madariaga, J.M., Mangold, N., McClean, J., Miklusicak, N., Nunes, D., Rojas, C., Runyon, K., Schmitz, N., Scudder, N., Shaver, E., SooHoo, J., Spaulding, R., Stanish, E., Tamppari, L.K., Tice, M.M., Turenne, N., Willis, P.A., Aileen Yingst, R., 2020. Photogeologic Map of the Perseverance Rover Field Site in Jezero Crater Constructed by the Mars 2020 Science Team. Space Sci Rev 216, 127. https://doi.org/10.1007/s11214-020-00739-x

Steele, A., Fries, M.D., Amundsen, H.E.F., Mysen, B.O., Fogel, M.L., Schweizer, M., Boctor, N.Z., 2007. Comprehensive imaging and Raman spectroscopy of carbonate globules from Martian meteorite ALH 84001 and a terrestrial analogue from Svalbard. Meteoritics & Planetary Science 42, 1549–1566. https://doi.org/10.1111/j.1945-5100.2007.tb00590.x

Summons, R.E., Amend, J.P., Bish, D., Buick, R., Cody, G.D., Des Marais, D.J., Dromart, G., Eigenbrode, J.L., Knoll, A.H., Sumner, D.Y., 2011. Preservation of Martian Organic and Environmental Records: Final Report of the Mars Biosignature Working Group. Astrobiology 11, 157–181. https://doi.org/10.1089/ast.2010.0506

Sun, V.Z., Stack, K.M., 2020. Geologic map of Jezero crater and the Nili Planum region, Mars [WWW Document]. URL https://pubs.er.usgs.gov/publication/sim3464 (accessed 2.12.21).

Takai, K., Nakamura, K., Toki, T., Tsunogai, U., Miyazaki, M., Miyazaki, J., Hirayama, H., Nakagawa, S., Nunoura, T., Horikoshi, K., 2008. Cell proliferation at 122°C and isotopically heavy CH4 production by a hyperthermophilic methanogen under high-pressure cultivation. PNAS 105, 10949–10954. https://doi.org/10.1073/pnas.0712334105

Tarnas, J.D., Mustard, J.F., Lin, H., Goudge, T.A., Amador, E.S., Bramble, M.S., Kremer, C.H., Zhang, X., Itoh, Y., Parente, M., 2019. Orbital Identification of Hydrated Silica in Jezero Crater, Mars. Geophysical Research Letters 46, 12771–12782. https://doi.org/10.1029/2019GL085584

Tarnas, J.D., Mustard, J.F., Sherwood Lollar, B., Bramble, M.S., Cannon, K.M., Palumbo, A.M., Plesa, A.-C., 2018. Radiolytic H2 production on Noachian Mars: Implications for habitability and atmospheric warming. Earth and Planetary Science Letters 502, 133–145. https://doi.org/10.1016/j.epsl.2018.09.001

Thompson, L.M., Berger, J.A., Spray, J.G., Fraeman, A.A., McCraig, M.A., O'Connell-Cooper, C.D., Schmidt, M.E., VanBommel, S., Gellert, R., Yen, A., Boyd, N.I., 2020. APXS-Derived Compositional Characteristics of Vera Rubin Ridge and Murray Formation, Gale Crater, Mars: Geochemical Implications for the Origin of the Ridge. Journal of Geophysical Research: Planets 125, e2019JE006319. https://doi.org/10.1029/2019JE006319

van Berk, W., Fu, Y., 2011. Reproducing hydrogeochemical conditions triggering the formation of carbonate and phyllosilicate alteration mineral assemblages on Mars (Nili Fossae region). Journal of Geophysical Research: Planets 116. https://doi.org/10.1029/2011JE003886

Viviano, C.E., Moersch, J.E., McSween, H.Y., 2013. Implications for early hydrothermal environments on Mars through the spectral evidence for carbonation and chloritization reactions in the Nili Fossae region. Journal of Geophysical Research: Planets 118, 1858–1872. https://doi.org/10.1002/jgre.20141

Viviano-Beck, C.E., Seelos, F.P., Murchie, S.L., Kahn, E.G., Seelos, K.D., Taylor, H.W., Taylor, K., Ehlmann, B.L., Wiseman, S.M., Mustard, J.F., Morgan, M.F., 2014. Revised CRISM spectral parameters and summary products based on the currently detected mineral diversity on Mars. Journal of Geophysical Research: Planets 119, 1403–1431. https://doi.org/10.1002/2014JE004627

Wang, A., Korotev, R.L., Jolliff, B.L., Haskin, L.A., Crumpler, L., Farrand, W.H., Herkenhoff, K.E., Souza, P. de, Kusack, A.G., Hurowitz, J.A., Tosca, N.J., 2006. Evidence of phyllosilicates in Wooly Patch, an altered rock encountered at West Spur, Columbia Hills, by the Spirit rover in Gusev crater, Mars. Journal of Geophysical Research: Planets 111. https://doi.org/10.1029/2005JE002516

Webb, G.E., 1996. Was Phanerozoic reef history controlled by the distribution of non-enzymatically secreted reef carbonates (microbial carbonate and biologically induced cement)? Sedimentology 43, 947–971. https://doi.org/10.1111/j.1365-3091.1996.tb01513.x

Werner, S.C., 2008. The early martian evolution—Constraints from basin formation ages. Icarus 195, 45–60. https://doi.org/10.1016/j.icarus.2007.12.008

Whiffin, V.S., Paassen, L.A. van, Harkes, M.P., 2007. Microbial Carbonate Precipitation as a Soil Improvement Technique. Geomicrobiology Journal 24, 417–423. https://doi.org/10.1080/01490450701436505

White, J.L., Sparks, R.S.J., Bailey, K., Barnett, W.P., Field, M., Windsor, L., 2012. KIMBERLITE SILLS AND DYKES ASSOCIATED WITH THE WESSELTON KIMBERLITE PIPE, KIMBERLEY, SOUTH AFRICA. South African Journal of Geology 115, 1–32. https://doi.org/10.2113/gssajg.115.1.1

Wordsworth, R., Knoll, A.H., Hurowitz, J., Baum, M., Ehlmann, B.L., Head, J.W., Steakley, K., 2021. A coupled model of episodic warming, oxidation and geochemical transitions on early Mars. Nature Geoscience 14, 127–132. https://doi.org/10.1038/s41561-021-00701-8

Wray, J.J., Dobrea, E.Z.N., Arvidson, R.E., Wiseman, S.M., Squyres, S.W., McEwen, A.S., Mustard, J.F., Murchie, S.L., 2009. Phyllosilicates and sulfates at Endeavour Crater, Meridiani Planum, Mars. Geophysical Research Letters 36. https://doi.org/10.1029/2009GL040734

Wray, J.J., Murchie, S.L., Bishop, J.L., Ehlmann, B.L., Milliken, R.E., Wilhelm, M.B., Seelos, K.D., Chojnacki, M., 2016. Orbital evidence for more widespread carbonate-bearing rocks on Mars. Journal of Geophysical Research: Planets 121, 652–677. https://doi.org/10.1002/2015JE004972

1811 Zamanian, K., Pustovoytov, K., Kuzyakov, Y., 2016. Pedogenic carbonates: Forms and formation
1812 processes. Earth-Science Reviews 157, 1–17. https://doi.org/10.1016/j.earscirev.2016.03.003
1813